NTNU
Norwegian University of
Science and Technology

Use of Tunnel Thrusters and Azimuthing Thrusters for Roll Damping of Ships

Sigbjørn Eng Rudå

Marine Technology
Submission date: June 2016
Supervisor: Sverre Steen, IMT

Norwegian University of Science and Technology
Department of Marine Technology

NTNU Trondheim
Norwegian University of Science and Technology
Department of Marine Technology

MASTER THESIS IN MARINE TECHNOLOGY

SPRING 2016

FOR

Sigbjørn Eng Rudå

Use of tunnel thrusters and azimuthing thrusters for roll damping of ships

For many ship types, like offshore vessels, mega-yachts, and fishing vessels, roll-damping at zero forward speed is an important issue. Anti-roll fins aren't effective at zero speed, and anti-roll tanks aren't always feasible. Therefore, there is a need for other anti-roll measures. It has been proposed to use tunnel thrusters and azimuthing thrusters already installed on the ship to provide extra roll-damping, but the effectiveness and energy-consumption of such an arrangement need to be clarified. The thrusters are used for dynamic positioning, but the dynamic positioning system is using the thrusters at a lower frequency than the roll natural frequency. Therefore, it might be possible to utilize the thrusters for both purposes at the same time.

The objectives of the master thesis are to determine the feasibility and effectiveness of using the thrusters for roll damping, and to give recommendations to how the thrusters might be controlled for maximum roll damping efficiency.

An experimental campaign, using an existing ship model, is planned to be a central part of the work. It is pointed out that in application of both experimental and numerical modelling, uncertainty is important to be aware of and assess and quantify as far as possible. For numerical modelling, uncertainty is usually limited to systematic (modelling) uncertainty, while experimental modelling typically will have both systematic (bias) and random errors.

In the thesis the candidate shall present his personal contribution to the resolution of problem within the scope of the thesis work.

Theories and conclusions shall be based on mathematical derivations and/or logic reasoning identifying the various steps in the deduction.

The thesis work shall be based on the current state of knowledge in the field of study. The current state of knowledge shall be established through a thorough literature study, the results of this study shall be written into the thesis. The candidate should utilize the existing possibilities for obtaining relevant literature.

The thesis should be organized in a rational manner to give a clear exposition of results, assessments, and conclusions. The text should be brief and to the point, with a clear language. Telegraphic language should be avoided.

The thesis shall contain the following elements: A text defining the scope, preface, list of contents, summary, main body of thesis, conclusions with recommendations for further work, list of symbols and acronyms, reference and (optional) appendices. All figures, tables and equations shall be numerated.

NTNU Trondheim
Norwegian University of Science and Technology
Department of Marine Technology

The supervisor may require that the candidate, in an early stage of the work, present a written plan for the completion of the work. The plan should include a budget for the use of computer and laboratory resources that will be charged to the department. Overruns shall be reported to the supervisor.

The original contribution of the candidate and material taken from other sources shall be clearly defined. Work from other sources shall be properly referenced using an acknowledged referencing system.

The thesis shall be submitted electronically (pdf) in DAIM:

- Signed by the candidate
- The text defining the scope (signed by the supervisor) included
- Computer code, input files, videos and other electronic appendages can be uploaded in a zip-file in DAIM. Any electronic appendages shall be listed in the main thesis.

The candidate will receive a printed copy of the thesis.

Supervisor : Professor Sverre Steen
Co-supervisor : Vahid Hassani
Start : 18.01.2016
Deadline : 19.06.2016

Trondheim, 18.01.2016

Sverre Steen
Supervisor

Preface

This thesis is written by Sigbjørn Eng Rudaa as a part of a Master's degree at the Marine Technology Department at the Norwegian University of Science and Technology (NTNU) in Trondheim. It was written during the fall term of 2016. The project, initiated and proposed by NTNU, will be included in the University Technology Center (UTC), which is run by NTNU in collaboration with Rolls-Royce. Furthermore, a conference paper based on this thesis is accepted and will be presented at the IFAC-CAMS 2016 conference in September.

During the autumn of 2015, I worked on a project thesis that was a pre-study to the master thesis. The primary focus of this project thesis was to understand and evaluate qualities of different software programs used when processing data for a possible master thesis, e.g. VERES ShipX and SIMULINK. I also undertook a thorough study and analysis of the available literature on roll damping systems. Furthermore, I created a simulation environment acquired most of the scheduled time, which turned out to be more time-consuming than initially estimated.

The central part of the master thesis has been based on improving the simulation model, by implementing a more suitable control system, by studying the dynamics of the thrusters, by carrying out experiments, and lastly by re-implementing simulation model to represent the experimental results as close as possible.

Even though this project was supposed to be a thesis in the field of hydrodynamics, it has eventually shown many similarities with marine cybernetics. The thesis has in general been difficult to carry out, due to my own lack of training in the field of marine control. However, this has in return given me a substantial learning outcome.

Trondheim, June 18th, 2016

Sigbjørn Eng Rudaa

Abstract

This thesis presents a novel technique of active roll damping in marine vessels by the sole use of conventional thrusters. Many marine operations, such as crane operation and helicopter landings, should be carried out in small and steady roll motions. However, active roll damping devices such as fins and rudders lose their efficiency in low-speed conditions. This thesis provides a new methodology for roll reduction by adjusting the shaft speed and pitch of the propellers, by use of already installed thrusters.

In order to develop a simulation environment suitable for representing realistic roll damping scenarios and validate the damping contribution from the thrusters, systematic experimental trials were carried out in the large towing tank at MARINTEK. The simulation model is based on the MSS Toolbox, with additional modifications added to represent roll motions more realistically, i.e. 4-quadrant open water results and non-linear sway and roll damping.

The numerical simulations and experimental trials, presented in the thesis, are compared with ship operations that require low roll motions, and shows promising results with significant roll reduction. Seakeeping trials related to roll motions are carried out to quantify the damping contribution. Decay tests showed average damping ratio 250% higher using the proposed anti-roll system compared to the undamped case. Furthermore, regular waves showed 40% damping in the area around resonance. Additionally, statistical values from irregular wave trials showed damping in the regime 30-64%. Lastly, operability diagrams were created using numerical simulations and was compared with helicopter landing criteria. It was shown that helicopter landings could take place 34% more often using the active roll damping system for oblique waves and 20% more often for beam waves.

Based on the results, it is concluded that the system works very well for moderate sea states, and that the damping contributions, that is to say in moderate sea state conditions, is comparable to that of currently available anti-roll systems

Sammendrag

Denne masteravhandlingen presenterer en ny teknikk for aktiv rulledemping for marine fartøyer ved bruk av konvensjonelle thrustere. Mange marine operasjoner, som for eksempel kranoperasjoner og helikopterlandinger, bør utføres mens fartøyet beveger seg med små og jevne rullebevegelser. Aktiv rulledempingsenheter som finner og ror mister imidlertid sin effekt når fartøyet holder lav hastighet. Denne avhandlingen fokuserer på bruken av allerede installerte thrustere for å oppnå rulledempning, og presenterer en ny metodikk for rulledemping ved å justere turtall og pitch på propellene.

For å utvikle et simulasjonsmiljø egnet for å representere realistiske rulledempningsscenarier, og for å validere dempingsbidraget fra thrustere, ble det utført systematiske eksperimenter i slepetanken hos MARINTEK. Simuleringsmodellen er basert på MSS-Toolbox, men ytterligere endringer ble lagt til for å representere rullebevegelsene på en mer realistisk måte, ved å bruke 4-kvadranters open water tester og ved å tilføye ikke-lineær demping i svai og rull.

De numeriske simuleringene og eksperimentelle forsøkene som presenteres i avhandlingen, blir i avhandlingen sammenlignet med skipsopperasjoner som krever lave rullebevegelser. I avhandlingen presenteres lovende resultater med betydelig rulledemping. Typiske tester knyttet til rullebevegelser har blitt utført for å kvantifisere dempingsbidraget. Decay-tester viste gjennomsnittlige dempingforhold på 250 % høyere ved bruk av det foreslåtte anti-rulle-systemet, sammenlignet med når modellen er udempet. Videre viste regulærebølgetester en dempning lik 40 % demping i området rundt resonans. I tillegg viste statistiske verdier fra studier av uregelmessige bølger, demping i regimet 30-64 %. Avslutningsvis ble det opprettet operabilitetsdiagrammer ved hjelp av numeriske simuleringer. Diagrammene ble sammenlignet med landingskriterier for norske helikoptre, utarbeidet og brukt av NHS. Det ble vist at helikopterlandinger kan skje 34 % oftere ved bruk av det aktive rulledempingssystemet for skrå innkommende bølger og 20 % forbedring for sidebølger.

Basert på resultatene, vises det at denne rulledempingsenheten demper i samme størrelsesorden som mange av dagens brukte dempesystemer under moderate sjøtilstander.

Acknowledgments

Most of all would I like to express my gratitude to Professor Sverre Steen at the Department of Marine Technology, for valuable guidance in the field of hydrodynamics, as well as for trying to keep me on a steady course by supervising the process at weekly meetings. Furthermore, would I like to thank Associate Professor Vahid Hassani for valuable feedback and convincing me to write a paper to the IFAC CAMS 2016 conference on the topic of this thesis. I would further like to thank Rolls-Royce Marine for pitching the idea, and for valuable thruster information, the ShipX model, and financing the experiments.

Additionally, would I like to thank the staff at MARINTEK for instrumenting the model, and for giving me valuable information regarding the experimental trials. Special thanks to Ph.D. Luca Savio, who was the project leader and Mikkel Danielsen for assisting me on the towing carriage, and making sure I did not fall in the water.

A jury consisting of Prof. Svein Sævik, Prof. Bernt Johan Leira, and Prof. Ingrid Bouwer Utne awarded me the price for *Best Master Thesis Poster of the Year* at the yearly *Master Thesis Poster Exhibition Awards* at the Department of Marine Technology. This is a great recognition, and it is very motivating to be picked among so many skilled candidates.

Lastly, I would also like to thank all of my fellow office colleagues, my girlfriend Elisabeth Andreassen and my family Mona Eng, Bjørn Rudaa, and Siri Eng Rudaa for much patience and support throughout this semester.

S.E.R

Contents

Nomenclature

Acronyms

1^{st}FS	1^{st} order Fourier series
20^{th}FS	20^{th} order Fourier series
ASW	Anti-submarine warfare
CDF	Cumulative density Function
CL	Centerline
COG	Vertical center of gravity
COR	Center of roll
DOF	Degree of freedom
GM	Metacentric height
MSS	Marine system simulator
NaN	Not a number
ODE	Ordinary differential equation
OL	Operability limit
PD	Proportional derivative
PM	Permanent magnet
PSO	particle swarm optimization
PTO	Percentage of time operable
RAO	Response amplitude operator
RMS	Root mean square
RPS	Rounds per second
RRD	Rudder roll stabilization

RT	Thruster reaction time
TV	Thruster variation
UDP	User datagram protocol

Greek Symbols

$\eta_{4_{\max}}$	Maximum roll amplitude
$\omega_{4_{max}}$	Maximum angular roll velocity
$\ddot{\hat{\eta}}_4$	Estimated roll acceleration
$\dot{\hat{\eta}}_2$	Estimated roll sway velocity
α	Propeller angle of attack at the propeller blade
β	Propeller angle of attack at radius 0.7R/ advance angle
β_w	Incoming wave direction
$\ddot{\boldsymbol{\eta}}$	Acceleration vector
$\dot{\boldsymbol{\eta}}$	Velocity vector
$\boldsymbol{\eta}$	Motion vector
$\boldsymbol{\theta_p}$	Vector for static propeller parameters
Δ	Weight displacement
η_0	Open water propeller efficiency
η_2	Sway motion
η_4	Roll motion
η_{4_S}	Significant roll amplitude
Λ	Logarithmic decrement
λ	Weibull scale parameter
ω	Angular velocity
ω_w	Wave frequency
ϕ	Velocity potential
ϕ_D	Diffraction potential
ϕ_g	User set optimization parameter
ϕ_p	Propeller pitch angle
ϕ_p	User set optimization parameter
ϕ_R	Radiation potential

ψ	Potential per unit velocity
ρ	Water density
τ	Control signal
ξ	Damping ratio
$\xi_{\%}$	Percentage change of the damping ratio
ζ	Wave amplitudes with respect to time
ζ_a	Wave amplitude

Superscripts

A	Added-mass matrix
B	Damping matrix
C	Restoring matrix
F	Summed forces acting on the body
$\mathbf{F}_{control}$	Input force vector
$\mathbf{F}_{env}$	Environmental forces
$\mathbf{F}_{hs}$	Hydro static force term
$\mathbf{F}_{hyd}$	Hydro dynamic force term
M	Mass matrix
B	Breadth moulded
$\mathrm{B}_2^{\mathrm{EQ}}$	Nonlinear equivalent sway damping
C_Q	4-quadrant propeller torque coefficient
C_T	4-quadrant propeller thrust coefficient
D	Propeller diameter
D_d	Design draught
D_F	Drag
F^R	Radiation force
H_w	Regular wave height
J_a	Advance number/advance ratio
K	Retardation function of time, Cummins (1962)
K_A	Control gain
K_Q	Nominal torque coefficient

K_Q	Propeller torque coefficient
K_R	Control gain
K_T	Nominal thrust coefficient
K_T	Propeller thrust coefficient
L_{PP}	Length between perpendiculars
L_F	Lift
M_{T4}	Thruster moment
P_D	Engine power
Q_a	Actual propeller torque
S_{XX}	Response spectrum
T_n	Net thrust
T_a	Actual propeller thrust
T_d	Damped natural frequency
T_N	Net thrust
T_0	Bollard pull thrust
V_a	Advance velocity/ ambient water velocity
V_t	Propeller tangential velocity
X_i	Decay test amplitudes
Z	Number of propeller blades

Subscripts

$\mathbf{p}_k^i$	Optimization particle
$\mathbf{x}_p$	Vector for dynamic propeller parameters
a	Weight arm from center of vessel used in inclination tests
$c_D^{\mathbf{H}}$	4-quadrant drag coefficient based on Healey et al. (1995)
$c_D^{\mathbf{L}}$	4-quadrant drag coefficient based on Häusler et al. (2013)
$c_D^{\max}$	Drag coefficient to approximate the 4-quadrant characteristics using the **L**-method
$c_L^{\mathbf{H}}$	4-quadrant lift coefficient based on Healey et al. (1995)
$c_L^{\mathbf{L}}$	4-quadrant lift coefficient based on Häusler et al. (2013)
$c_L^{\max}$	Lift coefficient to approximate the 4-quadrant characteristics using the **L**-method
$c_L^{\min}$	Drag coefficient to approximate the 4-quadrant characteristics using the **L**-method

$c_Q^{\mathbf{L}}$	Torque coefficient using the **L**-method
$c_T^{\mathbf{L}}$	Thrust coefficient using the **L**-method
c_c	time constant
f_Q	Propeller torque model
f_T	Propeller thrust model
g	Gravitational acceleration
k	Weibull shape parameter
k_w	Wavenumber
l	length of pendulum used in inclination tests
n	Propeller shaft speed
n_{bp}	Shaft speed at bollard pull
o_D	Drag coefficient to approximate the 4-quadrant characteristics using the **L**-method
o_L	Lift coefficient to approximate the 4-quadrant characteristics using the **L**-method
r_g	Random optimization variable
r_p	Random optimization variable
t	Time
t_c	Time constant in a first order system.
v_L	Linear speed
w	Movable weight used in inclination tests
z	Thruster momentum arm

List of Figures

List of Tables

Chapter 1: Introduction

In numerous marine operations, roll-damping at zero speed is of extreme importance. Typical active roll reduction systems such as Rudder-Roll Damping (RRD) and Anti-Roll Fins, are not capable at zero speed. Anti-roll tanks work well at low and zero speed condition. However, not all the vessels are equipped with such devices and in certain ships and operations, they cannot provide sufficient roll reduction. The use of thrusters for active roll reduction has already been proven feasible for cycloidal propellers by Jürgens and Palm (2009). However, to the author's knowledge, there is no report in existence today on the use of conventional propulsion systems, such as tunnel thrusters and azimuthing thrusters, for the purpose of active roll reduction in marine vessels.

Reduction of roll motion is essential during many operations. Roll reduction can also be necessary to secure life at sea by reducing the hazard of capsizing, as well as lowering the risk of damaging cargo. Additionally, certain operations are constrained to have adequate low roll amplitudes, e.g. helicopter landings and crane operations. In Norway the criteria for landing helicopters on small vessels requests for 2° or 3° in roll and pitch depending on the aircraft type, Helideck Certification Agency (2016). Furthermore, a workability analysis by van den Boom (2010) shows that the downtime for helicopter operations in the wintertime with good visibility varied between 70% and 90%. This study implies that roll damping techniques could lead to a significant economic benefit for operators since helicopters could be utilized year round, and the vessel will not have to transit to shore mid-operation. Furthermore, operations may become more tedious and time-consuming, seeing as crew members may struggle with carrying out their mission. This is illustrated by *NORDFORSK* table 1.1. Furthermore a study carried out

by Monk (1987) showed that the effectiveness of crew was reduced by 25-30% by root-mean-square roll angles equal to 6°.

Table 1.1: Criteria for effectiveness the crew, NORDFORSK 1987 (Faltinsen (1990),Fossen (2011))

Standard deviation (root mean square) criteria			
Vertical acceleration ($\dot{w}$)	Lateral acceleration ($\dot{v}$)	Roll angle (ϕ)	Description of work
0.20 g	0.10 g	6.0 deg	Light manual work
0.15 g	0.07 g	4.0 deg	Heavy manual work
0.10 g	0.05 g	3.0 deg	Intellectual work
0.05 g	0.04 g	2.5 deg	Transit passengers
0.02 g	0.03 g	2.0 deg	Cruise liner

According to Weinblum and St.Denis (1950), Perez (2005), roll damping modifications of ships come in three different varieties of technology that uses three different ways of achieving roll damping: the first way is to increase the damping. The second way is to increase the inertia, and the third is to reduce the exciting moment.

The primary focus and contribution of this thesis is on reduction of the net exciting moment and increase the damping using the propulsion system. Figure 1.1 illustrates how the thrusters can be used to counteract the exciting environmental moment.

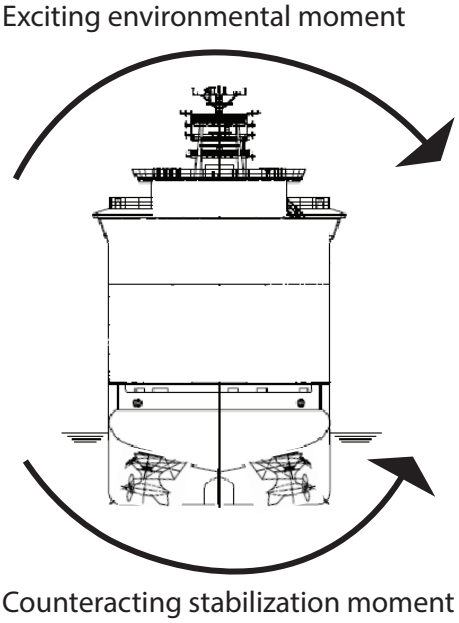

Figure 1.1: Thruster counteracting stabilization moment. The figure is a modification of the general arrangement from a vessel.

The work presented in this thesis show promising effectiveness in roll reduction. The concept of reducing the exciting roll moment with a propulsion system was proven experimentally to be efficient by Jürgens and Palm (2009). The major challenge in reduction of roll motion using the conventional thrusters compared to cycloidal propulsion units is their limited ability to change the direction of thrust. Voith Schneider's cycloidal propellers can change their direction of thrust nearly instantly, while the thruster dynamics of more conventional propellers is a function of the change of the shaft speed, pitching of the propeller blades, and the rate of change of azimuth angle.

The main problem of actively changing the shaft speed, propeller pitch and azimuth angle for roll reduction, is the resulting wear and tear on the propulsion system. However, *"Roll Reduction Mode"* might be executed only during particular critical operations that are constrained to low roll motions. Thus, the operation time of this control system can be of a minimal nature.

1.1 Overview of roll damping systems

As previously mentioned, roll motion of vessels can be one of the most important of motions to damp, thus several systems have been developed for the sole purpose of roll damping. The following section will consist of a brief discussion of already existing roll damping systems, including the active cycloidal propeller damping system which this thesis drew its inspiration from.

Bilge keels

Bilge keels are flat plates protruding from the ship side. The longitudinal lengths of the keels are about 25 to 50% of the length of the vessel. When a ship rolls, vortices from the keels are shed, and parts of the kinetic energy of the roll motion is transferred to fluid kinetic energy, Perez (2005). The reduction of resonant roll motion can be 35 %, however during irregular beam sea it is common to have an effect of around 10-20 % according to Sellars and Martin (1992).

Anti-roll tanks

Anti-roll tanks provide damping by containing tanks of water that move with the same velocity as the ship is rolling but with another phase, creating a counteracting moment that reduces the net excitation moment. The tanks are tuned by the water height of the tanks, and are often tuned to have maximum contribution at the natural roll period, for obvious reasons. There both are passive and active anti-roll tanks. Passive tanks have been measured to reduce the roll motion by 40-75 %, Sellars and Martin (1992).

Active fin stabilization

Active fins are large wing-like structures protruding from the side of the ship and is controlled by hydraulics to counteract the roll motion. They have shown huge potential as they can reduce the roll with magnitude 60-90%, Sellars and Martin (1992). But they come with a significant amount of drag and they are prone to cavitation and wear and tear. They are not effective at zero-speed since the fins will not generate any lift in this condition, only drag, which has a much smaller magnitude.

Rudder roll stabilization

Rudder roll stabilization (RRD) systems also depend on the vessel moving with sufficient velocity. The system works since the force acting from the rudder is lower than the center of roll, thus will it give a corresponding moment that can be used to counteract the excitation moment from the environmental forces. An illustration is shown in Figure 1.2 where one can see that the roll motion is reduced when the roll damping system is working (T>300).

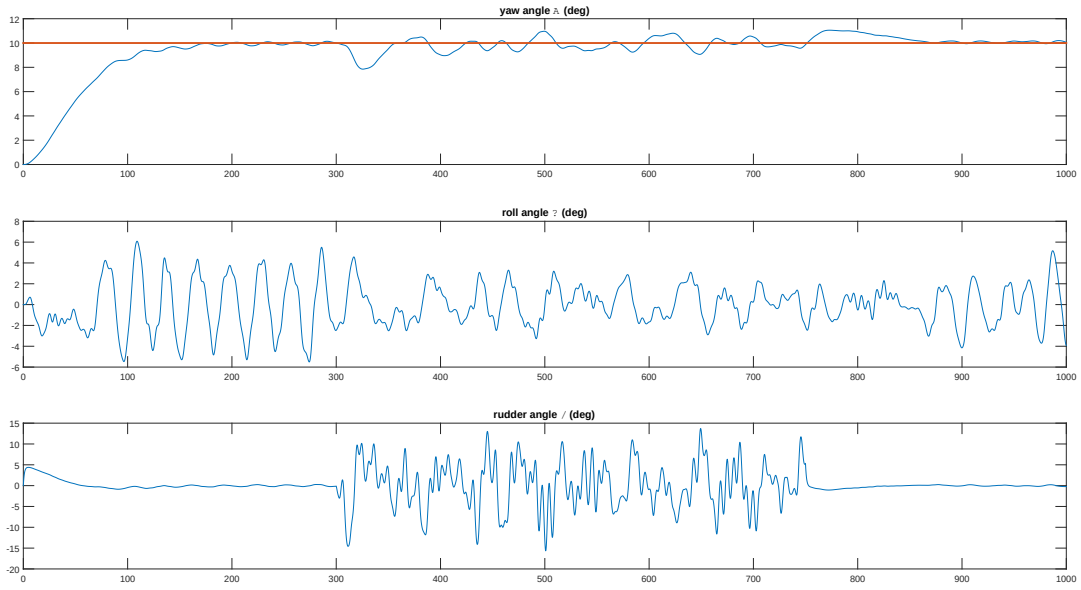

Figure 1.2: Performance of RRD. The system is active between t = 300-700 s. From (Fossen and Smogeli, 2004, p. 440) page 440.

Cycloidal propulsion damping

Cycloidal propulsion units are showing promising results regarding roll damping using thrusters. The first research was according to Voth Scheider (2006) carried out by Söding (2004) but the findings were not published. Prof. H Söding supposedly showed simulations where roll motion were almost totally suppressed at sea states with a significant wave height (Hs) of 6 meters and peak (Tp) period equal to 15 seconds, and for significant wave height equal to 3 meters and 10 seconds peak period. Furthermore, Jürgens and Palm (2009) carried out model tests for a vessel operating with significant wave height equal to 1.5 meters and peak period equal to 5 seconds. The results for this test case using two Voith Schneider propulsion units showed significant roll reduction of magnitude 64.9 %.

Additionally, a comparison study between cycloidal propellers and active fins was carried out by White (2013) where the vessel was free to move in roll and yaw. This study discussed the reaction time necessary to generate sufficient side thrust. It was concluded that the reaction time would need to be less that 13 seconds. These results show that reducing roll motion using tunnel and azimuthing propulsion may be an effective solution. However, unfortunately, the

natural roll period is not described in this paper and the general information about the ship model and thruster characteristics are too limited to make a decent comparison study with the findings from White's paper.

1.2 Organization of the thesis

The structure of the thesis is as follows:

Part I: Firstly the mathematical equations needed to describe vessel motions and thrust from the propulsion units will be presented. Secondly, in Chapter 3, the results of a preliminary feasibility study that was carried out by hand calculations to get an early estimate of the damping effect will be presented. This part was mostly conducted during the project thesis, but new calculations and figures are made during the master thesis since another case vessel was used. Chapter 4 consists of the dynamic effects that will be of importance during the simulations, and Chapter 5 explains the controller structure implemented, and parameter tuning adopted by use of optimization. Lastly, Chapter 6 consists of different roll motion performance techniques.

Part II: In Part II the model experiments carried out in the large towing tank at MARINTEK will be presented.

Part III: Part III presents the simulations carried out in SIMULINK. Firstly, a discussion will be presented on how to adjust the hydrodynamic loads, in order to make the simulation results as close to the experimental results discussed in Part II. Part III also contains presentations of tests not possible during the experiments, such as discussions on the effect of increased thruster reaction time and momentum arm and how the operability can be improved by using the proposed active roll damping system. Part III finishes with a formulation of the conclusion and recommendations for further work.

Part I

Mathematical Model

Chapter 2: Mathematical Model

The purpose of this chapter is to provide the reader with the theoretical assumptions that the later calculations are based on. The theory presented here will depict how a vessel's seakeeping capabilities can be described mathematically. Thus, these methods may be used for both steady state, i.e. no transient effects present and for time-domain analysis. While the former can only describe a linear/ linearized system, the latter can include the non-linear effects.

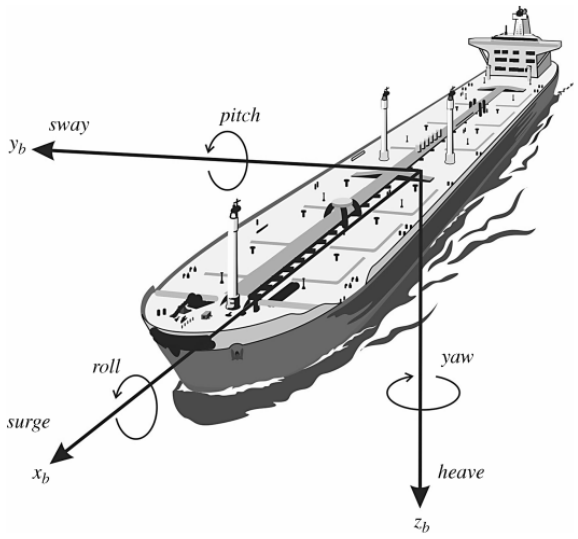

Figure 2.1: Six degree of motion of a vessel, found from Fossen (2011).

2.1 Equations of motion

A vessel can move in six degrees of freedom (DOF) where the first three represents translation motion and the last three represents the rotations, Figure 2.1. The corresponding motion is

described by Newton's second law as:

$$\mathbf{M} \cdot \ddot{\boldsymbol{\eta}} = \boldsymbol{F}_{hyd} + \boldsymbol{F}_{hs} + \boldsymbol{F}_{control} + \boldsymbol{F}_{env}, \tag{2.1}$$

here $\mathbf{M}$ represents the mass inertia matrix and $\ddot{\boldsymbol{\eta}}$ represents the acceleration of the DOF represented in 2.1. $\boldsymbol{F}_{control}$ represents the input variables to the system which would be the thruster excitation forces and moments. The last two vectors $\boldsymbol{F}_{hs}$ and $\boldsymbol{F}_{hyd}$ express the force acting on the vessel and they consist of the hydrostatic term (spring stiffness) and the hydrodynamic term which consist of the radiation, diffraction and the Froude-Krylov forces. Moreover,$\boldsymbol{F}_{env}$ represents the environmental forces acting on the body. By solving these equations the vessel motions can be found.

The motions of a floating vessel can be found by modeling it as a mass-damper-spring system which are described by the following formula:

$$\mathbf{(M+A)}\ddot{\boldsymbol{\eta}} + \mathbf{B}\dot{\boldsymbol{\eta}} + \mathbf{C}\boldsymbol{\eta} = \mathbf{F}, \tag{2.2}$$

where $\mathbf{(M+A)}\ddot{\boldsymbol{\eta}}$ are the mass forces consisting of a mass term and a added mass term, $\mathbf{B}\dot{\boldsymbol{\eta}}$ are the damping forces, consequently $\mathbf{C}\boldsymbol{\eta}$ are the restoring forces and $\mathbf{F}$ represents all the forces and moments acting on the mass-damper-spring system.

2.2 Strip theory

Strip theory is a popular linear theory used to estimate motions and hydrodynamic loads on structures and is based on the work of Salvesen et al. (1970). The method divides a structure info finite strips, i.e. cross sections, and integrate over the elongation direction to compute the 3D potential hydrodynamical coefficients added mass, damping, restoring and exciting wave forces, i.e. Froude-Krylov and diffraction loads. The method is proven to be especially accurate for zero-speed problems, something which coincides well with this project.

There exist several commercial programs to utilize the strip theory, e.g. VERES SHIPX developed by Marintek Fathi (2004) and the 3-potential code WAMIT developed by MiT. SHIPX has been used in this thesis.

2.3 Linear hydrodynamic loads

Irregular sea states are in hydrodynamic point of view generated by superposing regular wave components, and is thus considered linear, Faltinsen (1990). Because of this linear system, the hydrodynamic loads are usually decomposed into two separate contributions, namely the wave excitation forces and radiation problem.

The *excitation potential* consists of the Frode-Kriloff and diffraction forces and moments which depict the forces the vessel experiences when it is restrained from oscillation and there are waves present. The *radiation forces* represents the forces and moments the vessel will experience due to ship motions in an undisturbed sea, Newman (1977). The mentioned forces are illustrated in Figure 2.2. The corresponding velocity potential can now be described as a sum of the two contributions: $\phi = \phi_R + \phi_D$.

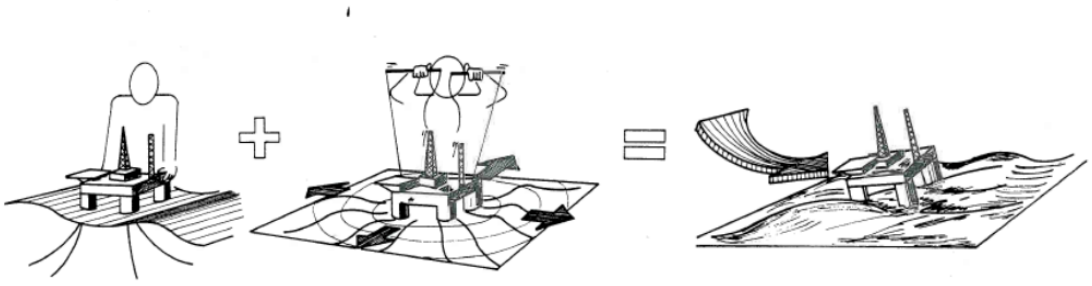

Figure 2.2: Superposition of excitation loads and forces from forced oscillations. From (Faltinsen, 1990, p.40).

2.3.1 Excitation potential

The excitation potential describes the propagating incident regular waves and the diffraction waves due to the interaction between a floating body and waves. The wave potential is outlined

in the literature as:

$$\phi_0 = \frac{g+\zeta_a}{\omega} e^{k_w z} cos(\omega t - k_w r), \tag{2.3}$$

where r is the direction the wave is propagating, and is defined as r = $(x^2 + y^2)^{1/2}$.

Moreover, the diffraction potential can be derived from the body boundary condition Faltinsen (1990). SHIPX(VERES), here by referred to as VERES, can calculate both potentials and writes the results as a complex force response amplitude operator (RAO). This force component includes the first-order wave force, which includes both the Froude-Krylov forces and the diffraction forces.

The corresponding amplitude and phases from the first order wave forces can be calculated according to Fossen (2011, p. 212) as:

$$F_{\text{wave}}^{\{\text{dof}\}} = \sum_{k=1}^{N} \rho g |F_{RAO}^{\{\text{dof}\}}(\omega_k, \beta)| \zeta_a \cos(\omega_k t + \angle F_{RAO}^{\{\text{dof}\}}(\omega_k, \beta) + \epsilon_k), \tag{2.4}$$

where F_{wave1} represents the first order wave force with respect to the degree of freedom (DOF), e.g. sway and roll. $|F_{RAO}|$ represents the force RAO, and $\angle F_{\text{RAO}}$ represents the phase. Furthermore, ϵ_k represents random phases.

2.3.2 Radiation potential

The radiation potential ϕ_R is as mentioned due to the motion of a vessel on an undisturbed sea. Newman (1977) described the radiation potential as:

$$\phi_R = \sum_{j=1}^{6} \dot{\eta}_j(t) \psi_j(t, \mathbf{r}), \tag{2.5}$$

where ψ_j represents the potential per unit velocity, $\dot{\eta}_j$ is the velocity of the vessel in the jth degree of freedom (DOF). Furthermore are the radiation forces given by

$$\mathbf{F}^R = -\rho \iint_{S_B} \mathbf{n} \frac{\partial \phi_R}{\partial t} dA. \tag{2.6}$$

Combining theses two equation the radiation forces can be expressed as:

$$F_i^R = -\sum_{j=1}^{6} \ddot{\eta}_j \rho \iint_S \psi_j dA - \sum_{j=1}^{6} \dot{\eta}_j \rho \iint_S \dot{\psi}_j dA, \tag{2.7}$$

$$= -\sum_{j=1}^{6} \ddot{\eta}_j A_{ij} - \sum_{j=1}^{6} \dot{\eta}_j B_{ij}, \tag{2.8}$$

where A_{ij} and B_{ij} represents the added mass and damping with i as the force direction and j as the motion direction.

2.4 Frequency domain

As previously mentioned, a popular approach to describe the motions of a vessel with a mass-spring-damper system, Equation (2.2). Assuming that this is a steady state problem, the equation can be rewritten to attain the steady state response represented as:

$$\boldsymbol{\eta} = \boldsymbol{\eta_a} e^{i\omega t}, \tag{2.9}$$

$$(-\omega^2 \mathbf{[M+A(\omega)]} + i\omega \mathbf{B}(\omega) + \mathbf{C})\boldsymbol{\eta_a} = \mathbf{F}(\omega), \tag{2.10}$$

where $\boldsymbol{\eta_a}$ is the complex response vector and the force ($\mathbf{F}(\omega)$) is the complex force vector. This expression is often used to calculate response amplitude operators (RAO) in the frequency domain.

2.5 Time domain

2.5.1 Cummins theorem

A popular approach finding the frequency dependent hydrodynamical coefficients and excitation forces, is by utilizing potential codes, as mentioned in Section 2.2. The typical hydrodynamic mass-damper-spring system that is frequently described in the literature can not be used for implementation in the time-domain, since time and frequency should not be mixed in ordinary differential equations (ODE). Consequently, Cummins (1962) equation is used, which includes the fluid memory effect.

Cummins' equation relates the response to the history of the excited wave forces, and it is represented by an integro-differential equation that includes a convulsion term, Pérez and Fossen (2008). The equation related to the equation of motion can be described by the Cummins' equation as:

$$(\mathbf{M}+\mathbf{A})\ddot{\boldsymbol{\eta}} + \int_0^t \mathbf{K}(t-\tau)\dot{\boldsymbol{\eta}}(\tau)\,d\tau + \mathbf{C}\boldsymbol{\eta} = \mathbf{F}, \tag{2.11}$$

where $\mathbf{K}$ is the convolution integral, which is called the retardation functions of time. The relationship between the frequency dependent equation of motion (2.10) and the representation by Cummins 2.11 was discovered by Ogilvie (1964). He used Fourier transform for sinusoidal excitation forces, and the following representation was found for the added mass and damping terms

$$\mathbf{A}(\omega) = \mathbf{A} - \int_0^\infty \mathbf{K}(t)\sin(\omega t)\,dt, \tag{2.12}$$

$$\mathbf{B}(\omega) = \int_0^\infty \mathbf{K}(t)\cos(\omega t)\,dt. \tag{2.13}$$

The added mass equation must be represented for the entire range of frequencies (ω) which

means that the following expression must be known:

$$\mathbf{A} = \lim_{\omega \to \infty} \mathbf{A}(\omega) = \mathbf{A}(\infty). \tag{2.14}$$

Inverse Fourier transform can also be used to rewrite the time- and frequency retardation function as:

$$\mathbf{K}(t) = \frac{2}{\pi} \int_0^\infty \mathbf{B}(\omega) cos(\omega t) d\omega. \tag{2.15}$$

Implementing these terms into the equation of motion, the correct time-domain representation of a vessel's motions can be attained, and it can be described as:

$$[\mathbf{M} + \mathbf{A}(\infty)]\ddot{\boldsymbol{\eta}} + \mathbf{B}(\infty)\dot{\boldsymbol{\eta}} + \int_0^t \mathbf{K}(t-\tau)\dot{\boldsymbol{\eta}}(\tau) d\tau + \mathbf{C}\boldsymbol{\eta} = \mathbf{F}, \tag{2.16}$$

$$\mathbf{K}(t) = \frac{2}{\pi} \int_0^\infty [\mathbf{B}(\omega) - \mathbf{B}(\infty)] cos(\omega\tau) d\omega. \tag{2.17}$$

For zero speed (U = 0), the potential damping will be zero at the extremes of the frequency domain according to Fossen and Smogeli (2004), which is the case for this study. Subsequently, can the expression be further simplified into:

$$[\mathbf{M} + \mathbf{A}(\infty)]\ddot{\boldsymbol{\eta}} + \int_0^t \mathbf{K}(t-\tau)\dot{\boldsymbol{\eta}}(\tau) d\tau + \mathbf{C}\boldsymbol{\eta} = \mathbf{F}, \tag{2.18}$$

$$\mathbf{K}(t) = \frac{2}{\pi} \int_0^\infty [\mathbf{B}(\omega)] cos(\omega\tau) d\omega. \tag{2.19}$$

2.6 Ship model

To make this project as realistic as possible, an existing case ship was used for the simulations. The case ship was a supply vessel, and the already implemented geometry file for VERES was provided. The main particulars of the vessel are listed in Table 2.1.

Table 2.1: Main particulars for the case vessel.

	Symbol	**Unit**	**Value**
Length between perpendiculars	L_{PP}	[m]	99
Breadth moulded	B	[m]	21
Design draught	D_d	[m]	6
Mass displacement	Δ	[tons]	9000
Vertical center of gravity	COG	[m]	7.38
Transverse metacentric height	GM_T	[m]	2.45

2.6.1 MSS toolbox

The *Marine System Simulator* (MSS) *Toolbox* is a Matlab and Simulink toolbox developed at NTNU. Its main developers are Professor Thor I. Fossen and Professor Tristan Perez. The code is open source and is especially useful for testing new ideas, Perez and Fossen (2009).

The MSS Toolbox works only with all 6 degrees of freedom as input, even though this project is only a two degree of freedom system, i.e. sway and roll. All the hydrodynamic coefficients and the excitation forces and moments are calculated by reading the output files from VERES. Unfortunately, the Toolbox was not working properly with VERES. Hence, configurations were made to make the program respond adequately. The fault occurred during calculation of the natural period for heave, roll and pitch motion. Since the peaks of the RAOs were already known, the corresponding natural frequencies could be found using the built-in *find* function. These extra lines of code made the MSS Toolbox work properly. The non-frequency dependent restoring moment was found to be $C_{44} = 2.168 \cdot 10^8$ [Nm/deg]. Furthermore, the frequency dependent coupled added mass and damping are illustrated for the vessel in the following figures:

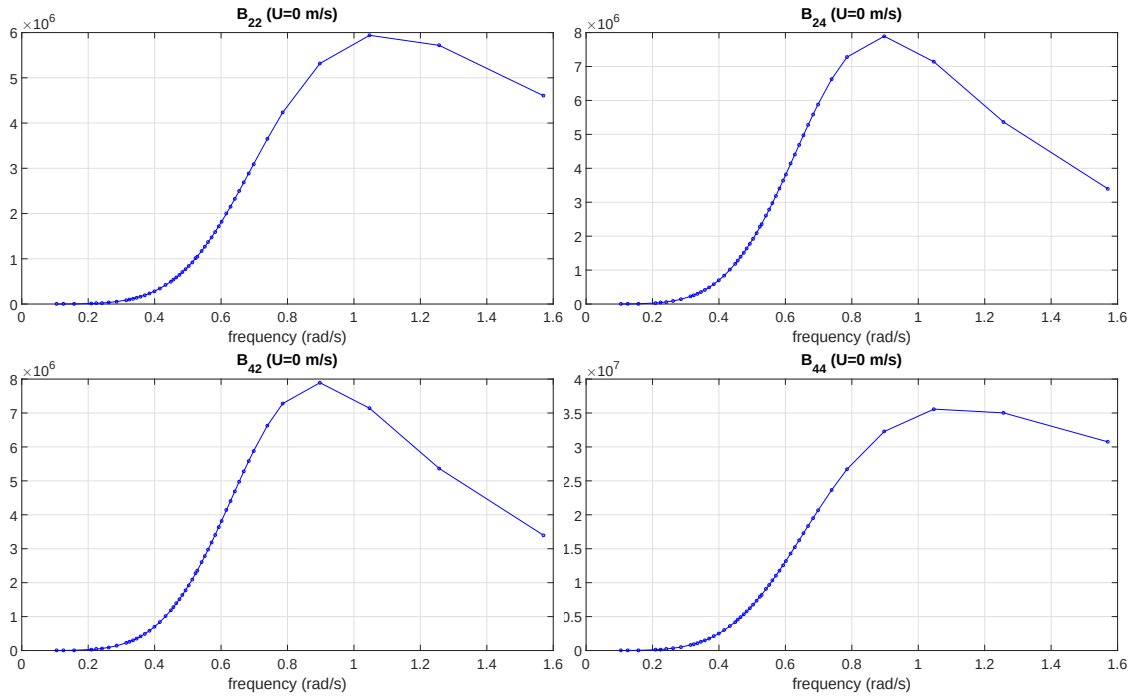

Figure 2.3: Lateral damping coeffients for the coupled sway (η_2) and roll (η_4) motions. Produced by the *MSS Toolbox*

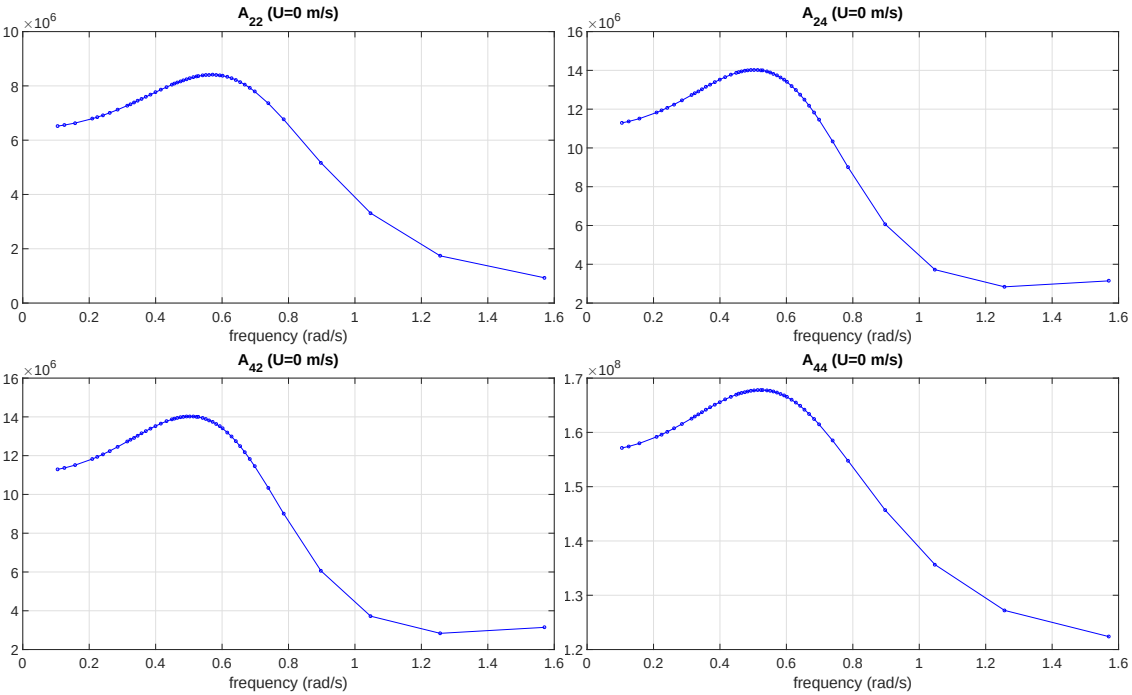

Figure 2.4: Lateral added mass coeffients for the coupled sway (η_2) and roll (η_4) motions. Produced by the *MSS Toolbox*

After the main vessel characteristics were found could these be used to calculate the retardation functions (fluid memory effect) approximated by transfer functions. They are approximated since one need the extremes of the frequency range, e.g $\mathbf{A}(\infty)$, to calculate the retardation functions (2.18 and 2.17), and they can not be computed by VERES. This is depicted by Figure 2.5, where the corresponding fluid memory effect is depicted in Figure 2.6. The approximations are carried out for all the coupled motions.

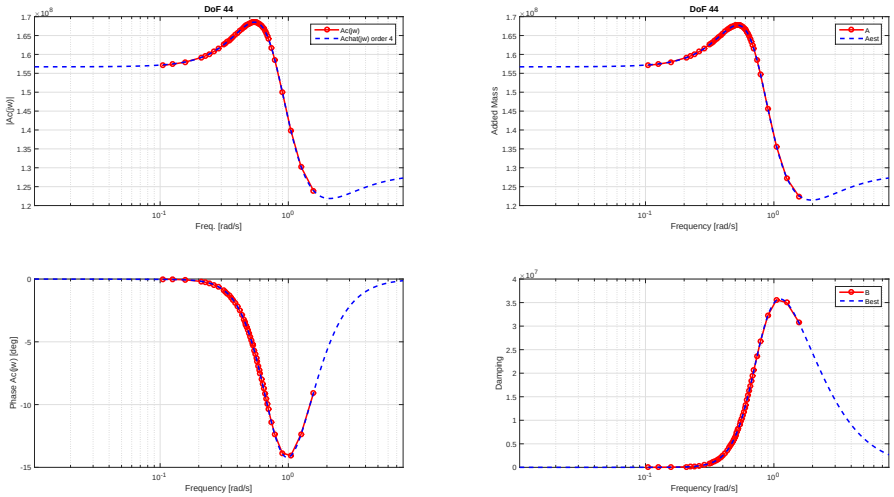

Figure 2.5: Hydrodynamic coefficients approximated by transfer functions from MSS Toolbox. Blue graph represents the estimated values for the frequency dependent added mass (upper right) and damping (down right), the red color represents the calculated values from VERES.

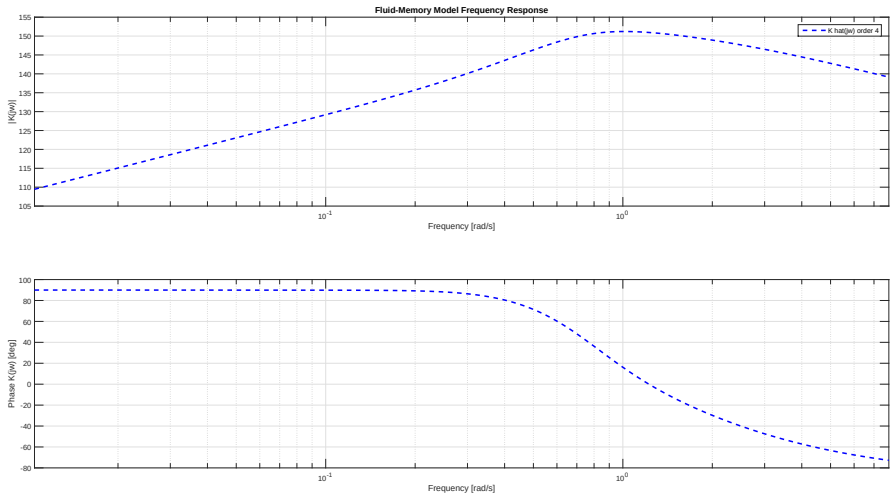

Figure 2.6: Roll retardation function approximated by transfer functions from *MSS Toolbox*.

2.7 Propulsion model

The propeller thrust (T_a) and torque (Q_a) are dependent on several static and dynamic values. The static values are typically propeller diameter and geometry. The time-varying parameters are generally the shaft speed (n), the advance ratio (J_a), pitch ratio, and the submergence. These values are described by Smogeli (2006) as:

$$T_a = f_T(n, \mathbf{x_p}, \boldsymbol{\theta_p}), \tag{2.20a}$$

$$Q_a = f_Q(n, \mathbf{x_p}, \boldsymbol{\theta_p}), \tag{2.20b}$$

where $\boldsymbol{\theta_p}$ defines the dynamic parameters and $\mathbf{x_p}$ represents the static parameters.

2.7.1 Open-water propeller models

The thrust of a propeller, with the exception of tunnel thrusters, is optimized to work in one direction. The conventional way of describing the thrust and torque of propellers is with so-called open water diagrams. The thrust and torque are made dimensionless using the following formulas:

$$K_T = \frac{T_a}{\rho \cdot D^4 \cdot n^2}, \tag{2.21a}$$

$$K_Q = \frac{Q_a}{\rho \cdot D^5 \cdot n^2}. \tag{2.21b}$$

These coefficients are found experimentally using open water tests, and they are conventionally plotted over the dimensionless advance ratio (J_a), which is described by the advance velocity (V_a), the shaft speed (n) and the propeller diameter (D):

$$J_a = \frac{V_a}{n \cdot D} \tag{2.22}$$

2.7.2 4-quadrant model

Even though the current thesis's main attention the roll reduction at zero-speed, is it not sufficient to model the thrust by bollard pull condition. This is because the ship is rolling, and thereby the inflow velocity to the thrusters is varying. Furthermore, roll reduction using the thrusters is not a conventional operation where the propellers are working in only one direction, i.e. positive advance ratio. Because of the zero-speed case with roll motion, the motions will introduce oscillating advance speeds to the thrusters as they are pointing in the direction of the roll motion. Thus leading to both positive and negative advance ratios. Standard open water diagrams can no longer address the problem sufficiently; for further discussions on this, see Smogeli (2006), Miniovich (1960), and van Lammeren et al. (1969). In this section, the Wageningen B-Series propellers are used as an example to describe the 4-quadrants. The quadrants are separated by the angle of attack (β), which is outlined by the ambient water velocity (V_a), the tangential water velocity (V_t), the propeller rotation rate (n) and the propeller diameter (D) as

$$\beta = \arctan(\frac{V_a}{V_t}) = \arctan(\frac{V_a}{0.7\pi nD}). \tag{2.23}$$

The quadrants as defined by Carlton (1994) are described in Table 2.2.

Table 2.2: The 4-quadrants

1^{st} quadrant	$0° \leq \beta \leq 90°$	$V_a > 0$	$n > 0$
2^{nd} quadrant	$90° < \beta \leq 180°$	$V_a > 0$	$n < 0$
3^{rd} quadrant	$180° < \beta \leq 270°$	$V_a < 0$	$n < 0$
4^{th} quadrant	$270° < \beta \leq 360°$	$V_a < 0$	$n > 0$

During the proposed roll reduction operation in zero-speed, only the 1^{st} and 4^{th} quadrant is of concern, since the shaft speed direction is positive. Thus, the relevant β values are in the interval $-90° \leq \beta \leq 90°$. The non-dimensional thrust and torque coefficients for the 4-quadrant model

are defined as

$$C_T = \frac{T_a}{\frac{1}{2}\rho(V_a^2 + (0.7\omega R)^2)\frac{\pi}{4}D^2}, \tag{2.24a}$$

$$C_Q = \frac{Q_a}{\frac{1}{2}\rho(V_a^2 + (0.7\omega R)^2)\frac{\pi}{4}D^3}. \tag{2.24b}$$

One can also describe the 4-quadrants with K_T and K_Q by equating (2.21a) and (2.24a), and similar manner for the torque using (2.21b) and (2.24b), leading to the following equations:

$$K_T = C_T\frac{\pi}{8}(J_a^2 + (0.7\pi)^2), \tag{2.25a}$$

$$K_Q = C_Q\frac{\pi}{8}(J_a^2 + (0.7\pi)^2). \tag{2.25b}$$

2.7.3 Model representation

The open water characteristics are as mentioned determined experimentally, and in order to use these results in simulations, further modifications must be introduced to avoid the non-continuous behavior of the experimental values. In following, the Wageningen B4-70 propeller is used for discussion purposes. Later in Part II the experimental values from the 4 quadrant open water tests will be discussed.

Fourier series

van Lammeren et al. (1969) described the thrust- and torque coefficients for a variety of propellers by using 20^{th} order Fourier series by two coefficients for the thrust (A_T and B_T) and two for the torque (A_Q and B_Q). The thrust and torque representations can then be calculated using:

$$C_T(\beta) = \sum_{k=0}^{20} (A_T(k)\cos(\beta k) + B_T(k)\sin(\beta k)), \tag{2.26a}$$

$$C_Q(\beta) = \sum_{k=0}^{20} (A_Q(k)\cos(\beta k) + B_Q(k)\sin(\beta k)). \tag{2.26b}$$

This can be depicted by the figure below where the 1st and 4th quadrants are plotted using equations (2.26). The coefficients used are found from the Wageningen B4-70, which is tabulated in (van Lammeren et al., 1969, Table 7) and is discussed thoroughly in Smogeli (2006). The A and B values can be found in Appendix A.1.

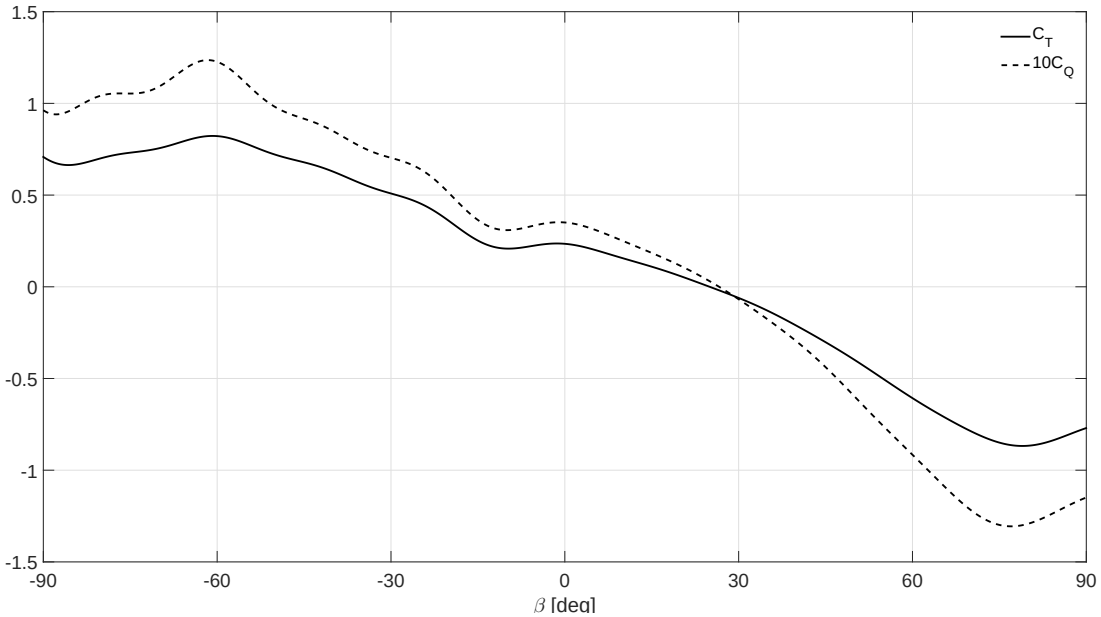

Figure 2.7: C_T and C_Q 1st and 4th quadrant from the 20th fourier series, van Lammeren et al. (1969).

A simplified version of this method is only to use the first terms in the Fourier series.

$$C_T(\beta) = A_T(0) + A_T(1)\cos(\beta) + B_T(1)\sin(\beta)), \tag{2.27a}$$

$$C_Q(\beta) = A_Q(0) + A_Q(1)\cos(\beta) + B_Q(1)\sin(\beta). \tag{2.27b}$$

The differences between the 20th and 1st order Fourier series are depicted in the Figure 2.8. Note that the deviation is fairly large around $\beta = 0$. This implies that open water characteristics in the boundary between the 1st and 4th quadrant are not well represented using the simplified Fourier series.

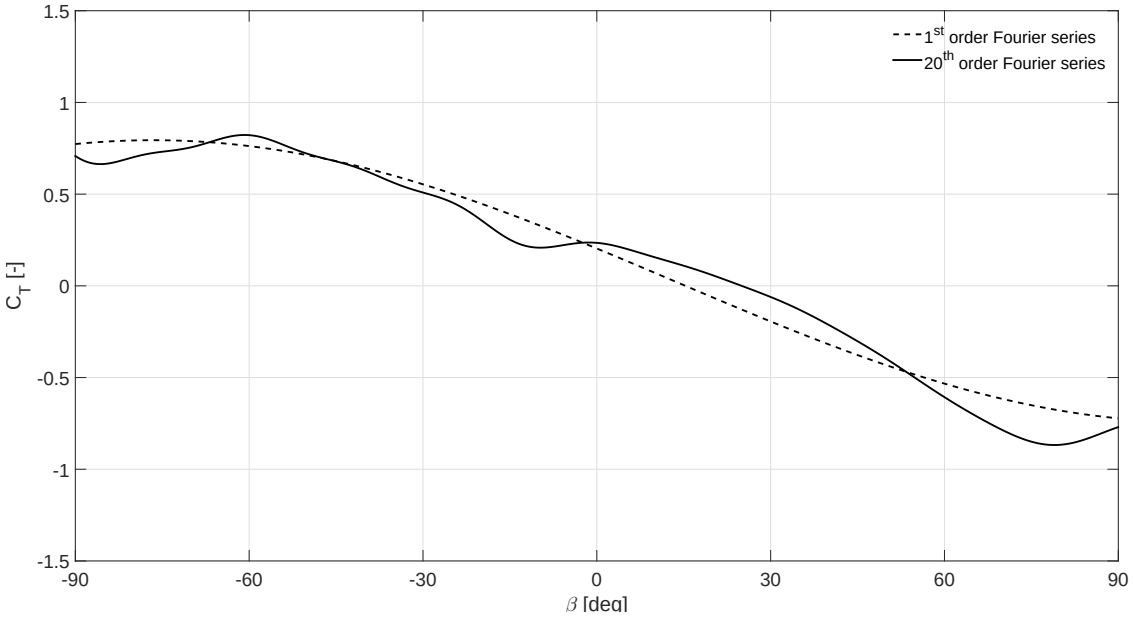

Figure 2.8: C_T 1st and 4th quadrant approximated using a 1st and 20th order Fourier series

Polynomial approximation

The open water characteristics can also be represented using a polynomial approximation. Smogeli (2006) presents both second order polynomial - and a linear approximation. K_T and K_Q can be approximated as a second order function using the following formulas:

$$K_T = K_{T0} + \alpha_{T1} J_a + \alpha_{T2} J_a |J_a|, \tag{2.28a}$$

$$K_Q = K_{Q0} + \alpha_{Q1} J_a + \alpha_{Q2} J_a |J_a|, \tag{2.28b}$$

where the α values are approximated constants, K_{T0} and K_{Q0} are the nominal thrust and torque coefficients.

A simplified linear approximation can also be introduced by imposing α_{T2}=α_{Q2}=0.

$$K_T = K_{T0} + \alpha_{T1} \mathrm{J}_a, \tag{2.29a}$$

$$K_Q = K_{Q0} + \alpha_{Q1} \mathrm{J}_a. \tag{2.29b}$$

The same polynomial approach can naturally be utilized for C_T and C_Q.

H- and L-Model

Healey et al. (1995) introduced the **H**-model. This method approximates the Wageningen series using lift (L_F) and drag (D_F) frame rather than thrust and torque frame. Healey et al. (1995) defined the lift and drag coefficients on a sinusoidal form:

$$c_L^{\mathbf{H}}(\alpha) = c_L^{max} \sin(2\alpha), \tag{2.30a}$$

$$c_D^{\mathbf{H}}(\alpha) = c_D^{max} (1 - \cos 2\alpha)/2, \tag{2.30b}$$

where $\alpha = \phi - \beta$ represents the angle of attack at the propeller blade, ϕ is the pitch angle. However Häusler et al. (2013) noticed that the **H**-model is lacking certain physical properties, e.g. the thrust and torque are zero at the same advance angle (β), a more detailed description can be found in Häusler et al. (2013) and Häusler et al. (2015). For this reason, the **L**-method was introduced as a modification of the **H**-model. The proposed amendment is represented by the formulas below:

$$c_L^{\mathbf{L}}(\alpha) = c_L^{max} \sin 2(\alpha - o_L), \tag{2.31a}$$

$$c_D^{\mathbf{L}}(\alpha) = (c_D^{max} - c_D^{min})(1 - \cos 2(\alpha - o_D))/2 + c_D^{min}, \tag{2.31b}$$

where the five parameters (c_L^{max},c_D^{min},c_D^{max},o_L,o_d) are, according to Häusler et al. (2013), deter-

mined using a nonlinear least square problem by fitting the curve with the open water characteristics. The thrust and torque coefficients can be found by replacing the Fourier series (2.26) using Equation (2.32).

$$c_T^{\mathbf{L}}(\beta) = c_L^{\mathbf{L}}(\beta)\cos(\beta) - c_D^{\mathbf{L}}\sin(\beta), \tag{2.32a}$$

$$c_Q^{\mathbf{L}}(\beta) = 0.7(c_L^{\mathbf{L}}(\beta)\sin(\beta) + c_D^{\mathbf{L}}\cos(\beta)). \tag{2.32b}$$

Chapter 3: Preliminary Feasibility Study in the Frequency Domain

This chapter is mostly based on the work carried out in the project thesis, Rudaa (2015). However, new calculations are conducted in the master thesis, because another case vessel was used in the project thesis. The purpose of this chapter is to present the results of a preliminary feasibility study in the frequency domain that was carried out to get an early feasibility estimate.

VERES was used to find hydrodynamical coefficients (**M**,**A**,**B**,**C**) and loads to describe the equation of lateral motion, Equations (3.1) and (3.2). The coupled *roll-yaw* component was assumed give negligible contribution for the coupled effect with roll in beam sea.

Salvesen et al. (1970) describes the coupled motions as:

$$(A_{22}+M)\ddot{\eta}_2 + B_{22}\dot{\eta}_2 + (M_{24}-Mz_c)\ddot{\eta}_4 + B_{24}\dot{\eta}_4 = F_2(t), \tag{3.1}$$

$$(A_{42}-Mz_c)\ddot{\eta}_2 + B_{42}\dot{\eta}_2 + (M_{44}+I_4)\ddot{\eta}_4 + B_{44}\dot{\eta}_4 + B_{44}^V|\dot{\eta}_4|\dot{\eta}_4 + C_{44}\eta_4 = F_4(t). \tag{3.2}$$

If the non-linear viscous damping term (B_{44}^V) can be replaced by the linearized term (B_{44}^L), the expressions of coupled motions can be rewritten in matrix form as follows:

$$\begin{bmatrix} M+A_{22} & A_{24} \\ A_{42} & I_{44}+A_{44} \end{bmatrix} \begin{bmatrix} \ddot{\eta}_2 \\ \ddot{\eta}_4 \end{bmatrix} + \begin{bmatrix} B_{22} & B_{24} \\ B_{42} & B_{44}+B_{44}^{L} \end{bmatrix} \begin{bmatrix} \dot{\eta}_2 \\ \dot{\eta}_4 \end{bmatrix} + \begin{bmatrix} C_{22} & C_{24} \\ C_{42} & C_{44} \end{bmatrix} \begin{bmatrix} \eta_2 \\ \eta_4 \end{bmatrix} = \begin{bmatrix} F_2 \\ F_4 \end{bmatrix}, \quad (3.3)$$

or in compact notation:

$$\mathbf{M}\ddot{\boldsymbol{\eta}} + \mathbf{B}\dot{\boldsymbol{\eta}} + \mathbf{C}\boldsymbol{\eta} = \mathbf{F}. \quad (3.4)$$

The transfer functions are found by implementing the terms (3.5) in the equation of motion, Equation (3.4). The resulting roll amplitude with the respect to frequency is described by the transfer function (3.6).

$$\eta_2 = \eta_{2a} \cdot e^{i\omega t}, \quad (3.5a)$$

$$\eta_4 = \eta_{4a} \cdot e^{i\omega t}, \quad (3.5b)$$

$$\boldsymbol{\eta}_a(\omega) = \frac{\mathbf{F}}{(i\omega\mathbf{B}(\omega) + \mathbf{C} - \omega^2\mathbf{M})}, \quad (3.6)$$

where $\boldsymbol{\eta}_a$ consist of the two amplitudes for sway and roll, i.e η_{2a} and η_{4a}.

Equation (3.6) was implemented in Matlab ®by using the hydrodynamical coefficients found using VERES, and was used to calculate the response amplitude operator (RAO) in roll (η_4). The results were then compared to the RAOs from VERES. The comparison between the steady state calculations and VERES is depicted in Figure 3.1.

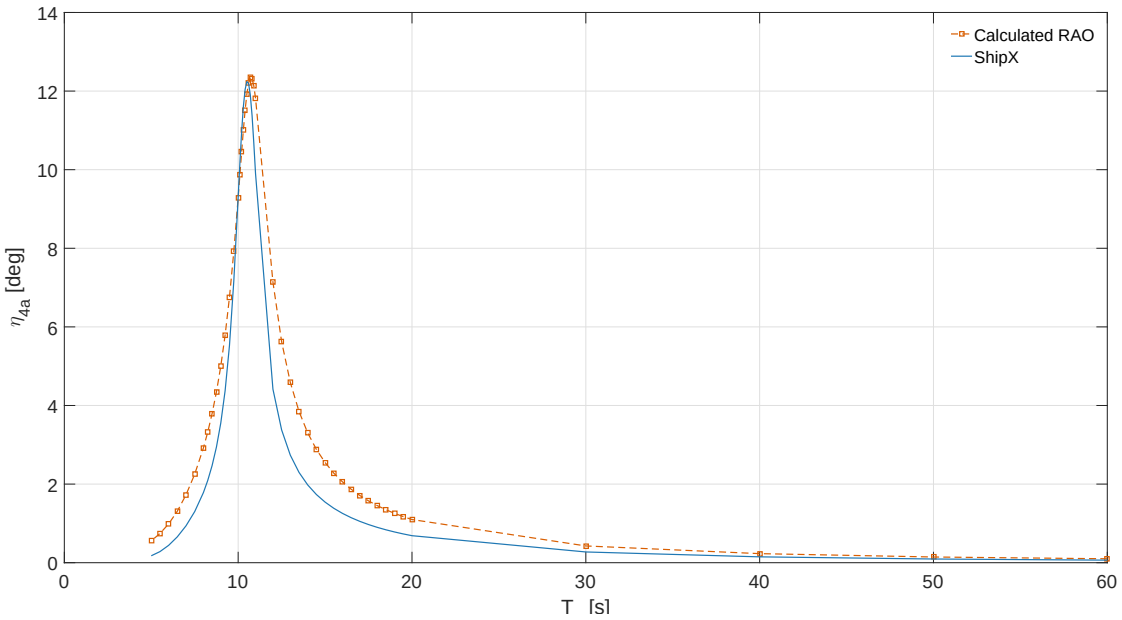

Figure 3.1: Motion RAO comparison. Orange represents calculated and blue line is calculated using VERES.

The reason for the discrepancy between the calculated RAO and the results from VERES ShipX is that the yaw contribution is neglected because this is a sway-roll case. The future calculations in the frequency domain will solely consider the roll response at the natural roll period, from the Figure 3.1 one can see that there is a good fit at this period.

3.1 Thrust and moment calculations

Bollard pull thrust calculations were utilized to find the steady-state thrust from the thrusters. The bollard pull thrust is calculated using (Steen, 2014b, Ch. 23):

$$T_0(N) = [10^6 \rho \pi \eta_p^2]^{1/3} \cdot [D^2 P_D^2]^{1/3} \tag{3.7}$$

All the propeller characteristics were provided by Rolls-Royce Marine, and the pump efficiency (η_p) was calculated using the regression on bollard pull model test by MARINTEK, and are found in Appendix C.1.

3.1.1 Thruster set up

The vessel is equipped with two Azipull thrusters in the rear, two tunnel thrusters and one swing up thruster at the bow of the ship. The characteristics of the thrusters are listed in Table 3.1. Moreover, the magnitude of the moments had to be considered. To find the moment arm, the center of roll must be known. It is assumed that the center of roll was placed half way between the center of gravity and the transverse metacentric height. The distance from the assumed center of roll and the center of thrust for the three different thrusters was found by studying the general arrangement using web plot digitizer. The calculated thrust and moments are represented in Table 3.1.

Table 3.1: Calculated thrust and moment using the bollard pull thrust approximation

Type			Azipull Open	Tunnel Ducted	Swing up Ducted
Number of thrusters			2	2	1
Engine power	P_D	[kW]	2 200	970	883
Propeller diameter	D	[mm]	3 200	2 400	1 800
Pump efficiency	η_p	[-]	0.5	0.7	0.7
Bollard pull thrust	T_0	[kN]	327	193	126
Moment arm	z	[m]	7.25	7.25	9.80
Thruster moment	M_{T4}	[kNm]	2373	1399	1241

3.1.2 Increased damping coefficient

There are two ways of implementing the damping moment from the thruster. Either as an extra excitation moment working against the excitation moment from the environmental forces, or by adding the contribution to the damping coefficient (**B**). For frequency domain analyses, it is easier ti implement the damping moment by introducing the moment as a damping component, since the sign of the moment can be disregarded. For time-domain analyses, the thrusters must be added as a counteracting moment because of their dynamic nature. Equation (3.8) was applied to convert the moment to a damping term.

$$B_{44M} = \frac{M_{T4}}{i\omega\eta_{4a}}. \tag{3.8}$$

At this point, only the steady state solution was examined. Therefore, the dynamic effect of the thrusters could not be modeled. The first goal was to see whether it was possible to gain above 50% damping using thrusters. To study this effect, the magnitude of damping that could be achieved by the thrusters at the natural roll period was calculated. Because of the variation of possible thruster set-ups, three test cases were carried out:

1. All thrusters work in the same direction with maximum thrust.
2. Each of the Azipull and bow thrusters operate in opposite direction (probably the most feasible operation mode).
3. same as 2) but the swing up operates in both directions.

The results from these three test cases are tabulated in Table 3.2.

Table 3.2: Calculated thrust and moment and roll reduction in the frequency domain.

Description		**Unit**	**Test case 1**	**Test case 2**	**Test case 3**
Moment from Azipull thrusters	M_{Azi}	[kNm]	4746	2373	2373
Moment from tunnel thrusters	M_{Tunnel}	[kNm]	2798	1399	1399
Moment from swing up thruster	M_{SU}	[kNm]	1241	0	1241
Total moment	M_T	[MNm]	8.79	3.77	5.01
Total damping contribution	B_M	[MNms/deg]	170.77	73.32	97.45
Roll amplitude	η_{4a}	[deg]	2.39	3.40	2.98
Roll reduction		[%]	52	32	40

The steady state damping effect for test case 2 is depicted in Figure 3.2 where the x-axis represents the damping term multiplied with the factor i, and the y-axis represents the roll response at the natural roll period.

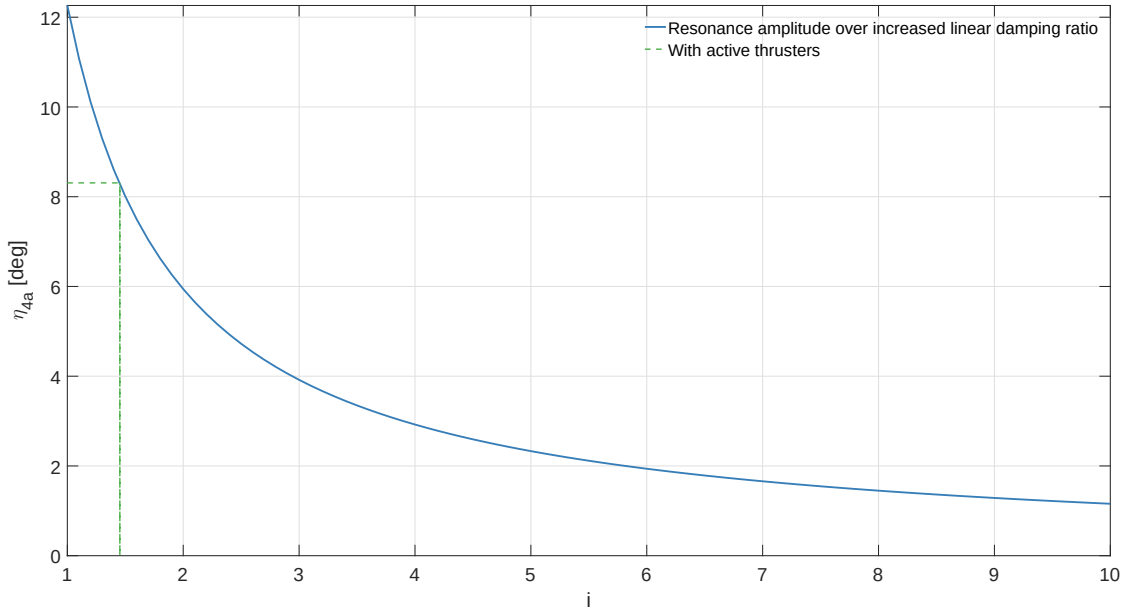

Figure 3.2: Increased damping term as a function of increased roll moment relative to the roll damping.

Even though the thrust was below the objective damping contribution, the effect of the thrusters was quite substantial. However, this is a steady state case, meaning that all the dynamics of the system are neglected, and a realistic scenario would feature irregular waves.

Chapter 4: Time Domain Simulations

The thruster dynamics will have substantial effects, thus is it important to create a realistic simulation model and carry out time domain simulation. This chapter's primary goal is to describe the building blocks of the dynamic simulation environment. First, typical seakeeping trials related to rolling motions are presented. Secondly, a novel approach to lower the reaction time of the thrusters is described. Lastly, the propeller model representation discussed in Section 2.7 are compared and reviewed.

4.1 Seakeeping trials related to roll motion

Before the experimental and numerical simulated results can be evaluated, it is necessary to discuss the different seakeeping trials related to roll motion. The methods used in this thesis are roll decay tests, regular waves, and irregular waves.

4.1.1 Decay test

Decay tests illustrate the damping of a dynamic system. When analyzing damping in decay tests, it is common practice to calculate the logarithmic decrement (Λ). The logarithmic decrement is calculated using two succeeding amplitudes (X_i) where i describes each succeeding amplitude:

$$\Lambda = \frac{X_i}{X_{i+1}}. \tag{4.1}$$

Then, the damping ratio ξ is defined by the logarithmic decrement as:

$$\xi = \frac{\Lambda}{\sqrt{(2\pi)^2 + \Lambda^2}}. \tag{4.2}$$

The damping ratio can be used to calculate the equivalent linearization of the nonlinear damping term, which is determined by assuming equal damping energy per roll cycle, Faltinsen (1990), is used to determine the equivalent nonlinear damping term:

$$\mathrm{p_{EQ}} = \mathrm{p_1} + \frac{8}{3\pi}\omega \mathrm{x_0 p_2}. \tag{4.3}$$

The damping ratio is plotted as a function of the mean amplitude that was used to calculate the damping ratio. This graph can be linearized to find the damping terms. $\mathrm{p_1}$ is the point at the abscissa, and $\mathrm{p_2}$ is the slope of the least square linearization.

4.1.2 Regular waves

Regular waves are in principal harmonic sinusoidal waves that consist of a wave amplitude (ζ_a) and a wave frequency (ω_w). These waves can be categorized as the most simple forms of waves and are illustrated by Equation (4.4).

$$\zeta(t) = \zeta_a \cos(\omega_w t). \tag{4.4}$$

The results of regular waves can not depict how a vessel will behave in a typical environment, nonetheless these waves can produce valuable information on how the vessel will respond to different wave frequencies. The RAO analyses can also be used for verification purposes, i.e. validate simulations against experimental results.

Regular wave tests are usually used for obtaining motion RAO, and are found by calculating the

ratio between the response and the wave amplitudes:

$$RAO(\omega_w) = \frac{\eta_4(\omega_w)}{\zeta_a}. \tag{4.5}$$

4.1.3 Irregular Waves

In order to attain more realistic simulation scenarios, irregular waves are carried out. The irregular waves were implemented according to the 17$^{\text{th}}$ ITTC recommended JONSWAP (Joint North Sea Wave Project) spectrum.

An example of a spectrum is illustrated in Figure 4.1 where the peak frequency is selected as the natural roll period (Tp = 10.5 s), with a significant wave height equal to 1.5 meters, and γ is equal to 3.3.

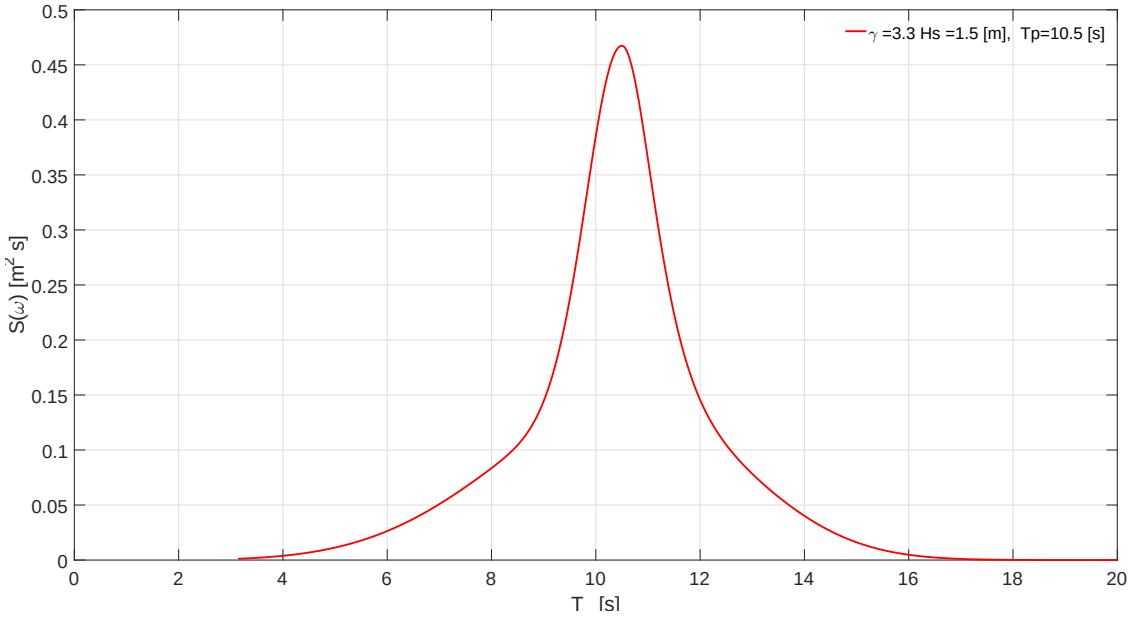

Figure 4.1: Jonswap spectrum with peak frequency equal to natural roll period and a significant wave height equal to 1.5 meters.

4.2 Thruster dynamics

The three different thrusters contain some dynamic constraints, e.g. pitching time (full astern to full forward), change of shaft speed and Azimuth angle. The mentioned dynamical parameters are listed in Table 4.1.

4.2.1 Transient effects

Before the discussion regarding the different dynamics thruster set-up, one should examine the transient effects of thrusters in general. It has been shown that the dynamic effects acting upon the torque and thrust can be viewed as quasi-steady. Steen (2014b) described this as *"change of operational condition is relatively slow compared to the revolution speed"*. Experimental and numerical results supported this study. Assuming that the error will be small for assuming quasi-steady propulsion performance will significantly simplify the dynamic propulsion effects.

4.2.2 Dynamic setup

The reader should note that from this point the swing-up thruster will not be discussed further. The reason is twofold: Firstly, because the thrust variations should be equal in both directions, i.e. the swing-up would only contribute to one direction due to the reaction speed limitations. Secondly, because the swing-up thruster could be used solely for station keeping.

Both the Azipull and bow thrusters have the ability to regulate propeller pitch and shaft speed. Both the bow and the Azipull thrusters have pitching times (0-100%) equal to 7.5 seconds, while the shaft speeds require 10 seconds to reach to its maximum speed, Table 4.1 . The thrust was found to be increasing linearly with the pitch. This was calculated by changing the pitch angle for Wageningen B-series Propellers open water characteristics (enclosed in the electronic Appendix) while the advance ratio was set to zero, i.e. bollard pull. This linearity is depicted in Figure 4.2.

Table 4.1: Dynamical thruster constrains.

Thruster	Azipull 120 CP	TT2200 CP
Type	Azipull	Tunnel
Shaft speed rate (0-100%)	10 s	10 s
Pitching time (0-100%)	7.5 s	7.5 s

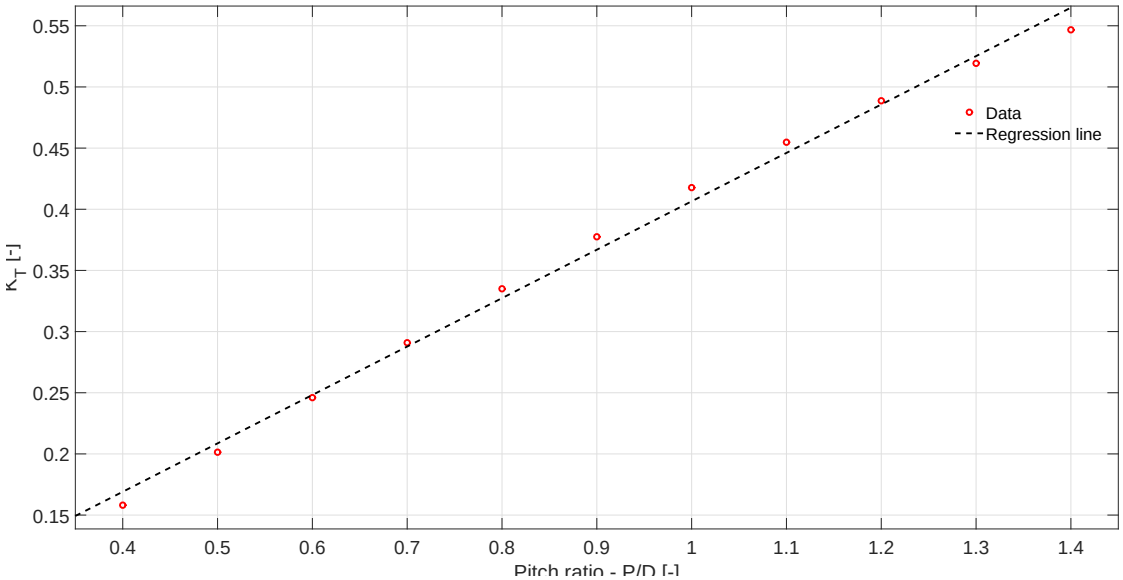

Figure 4.2: Thrust coefficient as a function of the propeller pitch. With regression line, R=98.88%

Furthermore, the thrust increases with the square of the shaft speed, because of the open water equation (2.21a). The thrust can be controlled by pitch, shaft speed or a combination of the two. In Figure 4.3, representative time series of thrust controlled by only propeller pitch, only shaft speed, and a combination of both pitch angle and shaft speed are presented.

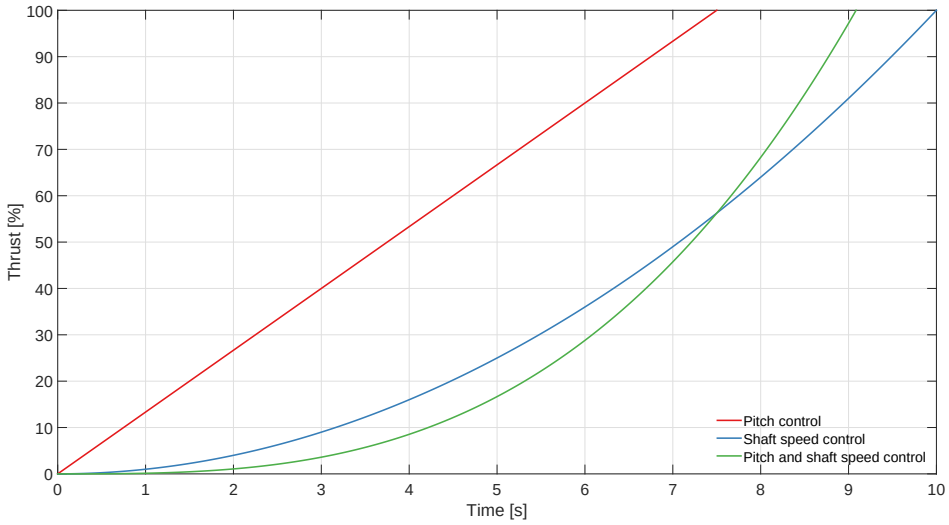

Figure 4.3: Thrust development with respect to time. Red: Thrust with respect to time for pitch-control. Blue: shaft speed control. Green: combination between pitch and shaft speed control.

Figure 4.3 illustrates that the reaction times are relatively slow if one wants to vary the thrust between 0-100% thrust by sole use of pitch or shaft speed. In order to overcome this problem, it has been suggested that one can regulate the thrust by combining pitch and shaft speed control, because it has the steepest slope. Additionally, by constraining the minimum thrust to a certain value, e.g. operating in the range 30-100% thrust, it is apparent that the slope of the curve is higher, so that the effective dynamic response improves. Table 4.2 presents the reaction time for different minimum thrust limits when using the combination of pitch and shaft speed to control thrust. The reason not to set the lower limit too high, is of course that this restricts the change of thrust force, which is what provides the damping moment.

Table 4.2: Thruster reaction time with respect to minimum thrust limit.

Minimum thrust limit	[%]	20	30	40	50	60
Reaction time	[s]	3.76	2.99	2.38	1.86	1.41

4.3 Modeling the thrusters in oscillatory flow

It has been shown in (Huse and Børresen, 1983, Enclosure 13) that thrusters operating at constant shaft speed reduce the roll motion. It is believed that this is due to the variation of advance speed discussed in Section 2.7. It is of interest to study to what degree the different representations of the propeller model would influence the roll damping when the shaft speed is constant.

A sensitivity study using decay tests was carried out, in order to see the effect of the damping found by Huse and Børresen (1983). This was done by extracting the amplitudes during the decay test using an image toolbox, the results of which can be found in Appendix A.2. The average of the damping ratios with and without working thrusters were calculated and compared. The average damping ratio was increased with 230% when the thrusters were working with constant shaft speed. This indicates that the possible damping from the thrusters could be of great magnitude. However, the vessel used in Huse and Børresen (1983) is of a semi-submersible type, hence the seakeeping capabilities quite different from conventional ships.

4.3.1 Open water representation techniques

At this point, open water characteristics for the case propellers were not available. Therefore, the Wageningen B-series B4-70 propeller was chosen for simulations, because it had 4-quadrant characteristics. The necessary propulsion values are listed in Table 4.3.

Table 4.3: Wageningen B-series B4-70 propeller data. Number of blades Z, diameter D, shaft speed at bollard pull n_{bp}, and bollard pull thrust T_{bp}

Z	D	n_{bp}	T_0	z_T
4	4m	2.05rps	490 kN	7.25m

In order to find the incoming velocity, it is necessary to change from angular velocity (ω) to linear speed (v_L) by multiplying the momentum arm (z):

$$v_L = z \cdot \omega. \tag{4.6}$$

The decay test with constant shaft speed were simulated through the application of a step-load moment to induce roll motions. β can be found by using the given parameters and equations (2.23) and (4.6). The value was found to be approximately $\beta \approx \pm 5°$. Because of the oscillatory advance speed around zero would it be necessary to know how the 4-quadrant open water characteristics are in this regime. The purpose behind this study was to compare the different propeller model representations discussed in Section 2.7.3, e.g 20^{th}- and 1^{st} order Fourier series Formulas (2.26) and (2.27), the linear approach Formula 2.29, and the L-model represented by Formulas (2.31) and (2.32). Figure 4.4 depicts how the 4-quadrant thrust coefficient (C_T) varies for the different approximation method for $\beta = \pm 20°$. The linear regression is approximated using $\beta = -20°$ and $\beta = 0°$, e.g bollard pull condition.

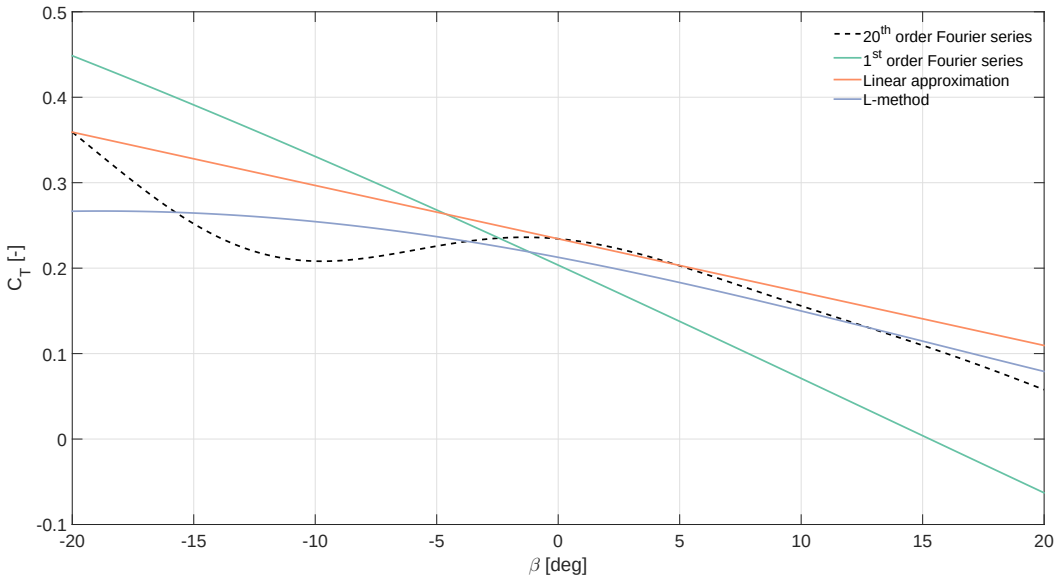

Figure 4.4: 4-quadrant representation techniques comparison study, $\beta = \pm 20°$

Figure 4.5 represents 4-quadrant thrust coefficient when $\beta = \pm 5°$, which is the interval that is expected that the propellers will work in during the decay trials. Furthermore, the decay trial is simulated in Figure 4.6.

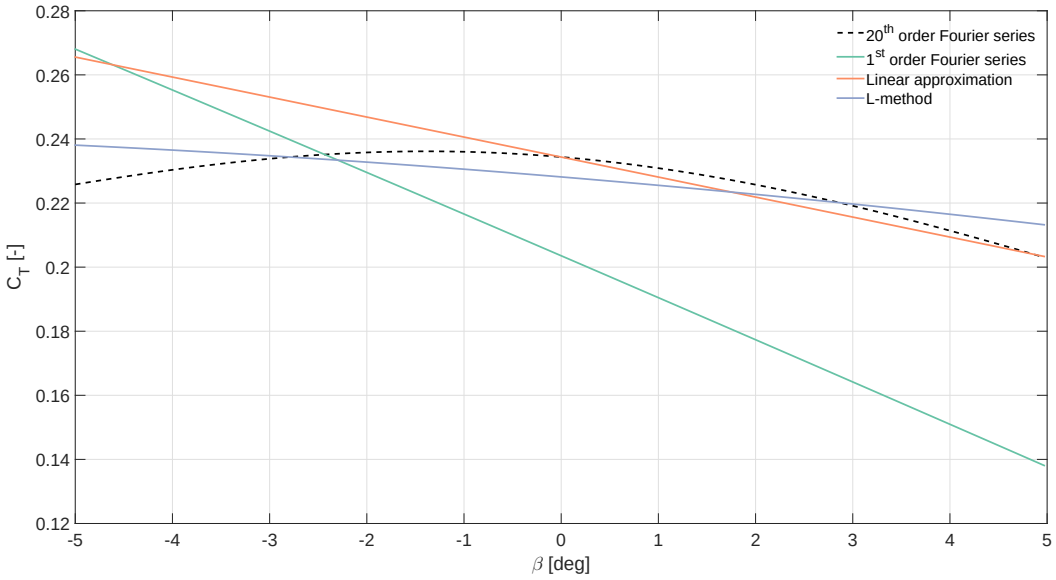

Figure 4.5: 4-quadrant representation techniques comparison study, $\beta = \pm 5°$

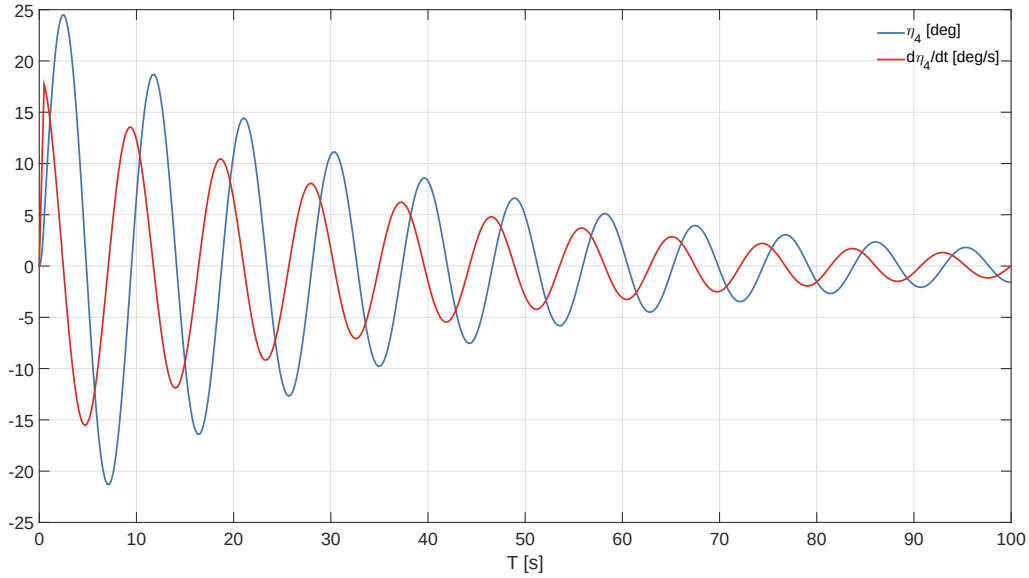

Figure 4.6: Simulated free oscillation test with constant shaft speeds. Blue is the roll amplitude, and the red graph represents the roll rate of the vessel ($d\eta_4$/dt).

Figure 4.7 illustrates how the net thrust (T_N) is developing throughout the decay test for the different 4-quadrant approximations. From the results, the L-method is relatively close to the assumed most correct method, i.e. 20th order Fourier series, and it is apparent that both of these

methods depict the lowest net thrust. The 1st order Fourier series resulted in the highest net thrust. The reason why this approximation gives the largest thrust is due to the large derivative $dC_t/d\beta$. This effect is clearly depicted in Figure 4.5.

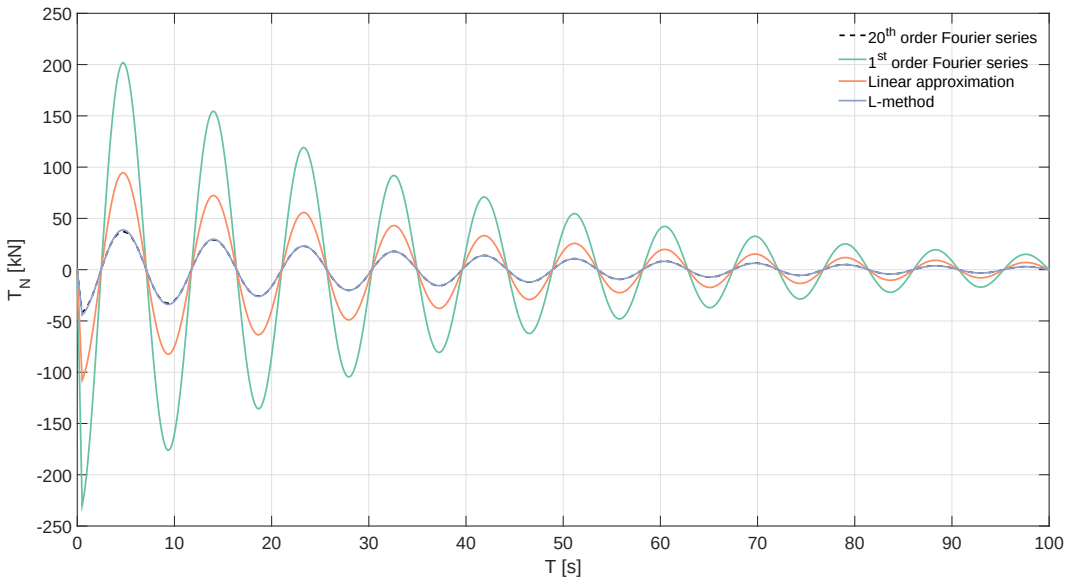

Figure 4.7: Net thrust for the different 4-quadrant approximations.

The results show an indication of how sensitive the thrust is to the 4-quadrant open water representations, especially in the interval around the bollard pull range, e.g. $\beta = [-5°, 5°]$. The percentage increased damping ratio ($\xi_{\%}$) concerning open-water method are tabulated in Table 4.4. Thus, the L-method is implemented in future open water representations, since the 20^{th} order Fourier series are more laborious and several points are needed to get the correct representation.

Table 4.4: Percentage difference in damping ratios for different 4-quadrant representations.

Method	20^{th} FS	1^{st} FS	Linear	L-method
damping ratio	3.49%	17.97%	8.36%	3.45%

Chapter 5: Control

This chapter consists of the control theory used to implement the proposed control system. After implementing some of the code simulating the vessel motions, it was discovered that a lot of simulation code related to the 6-degree motion of a vessel at zero-speed had been widely researched and the MSS Toolbox granted existing open source code. The toolbox is mainly built for ordinary DP-operations, which do not represent roll motion sufficiently. Therefore, additional blocks are added to the existing SIMULINK blocks to achieve a simulation environment suitable for the roll damping cases.

5.1 Controller

The controller that is exploited in the current thesis is the result of several different trials and is of a nonlinear Proportional-Derivative (PD) controller type, in the form of

$$\tau_{\mathrm{PD}} = -K_A \cdot \mathrm{sign}(\dot{\eta}_4)\sqrt{\frac{|\dot{\eta}_4|}{c}} - K_R \cdot \ddot{\eta}_4. \tag{5.1}$$

K_A represent the gain for the estimated roll acceleration ($\ddot{\eta}_4$) and and K_R is the gain for the roll rate term $\dot{\eta}_4$. Furthermore, the nonlinear square root term is added because the contribution from the thrusters should be equally large for all roll rates. By applying the square root term, the term $\sqrt{\frac{|\dot{\eta}_4|}{c}}$ will be decreased for $|\dot{\eta}_4|/c > 1$, and increased for $|\dot{\eta}_4|/c < 1$, where c is a tuning parameter. If linear control would be utilized and the derivative gain would be large, the system would work well for lower roll rates, but it would also saturate the shaft speed for an excessively

long duration during larger roll rates. For lower gains, the system would work well for large roll rates, but the shaft speed would not be fully utilized for lower roll rates.

5.2 Thruster dynamics modeling

The thrusters must be modeled with a limitation of an upper boundary of the maximum thrust and the thruster reaction time, e.g. pitching time and shaft speed. The major difference between conventional Azipull thrusters and Voith Schneider thrusters, is as mentioned the ability to change the direction of the thrust. Thus, the sensitivity of modeling the thruster dynamics is of great importance. The thrusters main particulars can be found in Table 3.1 and 4.1.

5.2.1 Saturation

To restrict the shaft speed from reaching a higher value than the maximum, saturation elements are added to the control system. The saturation is implemented using the following expression:

$$\text{sat}(\tau) = \begin{cases} \text{sign}(\tau)\tau_{max} & \text{if } |\tau| \geq \tau_{max} \\ \tau & \text{else} \end{cases}, \tag{5.2}$$

where τ is the control signal.

As previously mentioned the correct implementation of the thruster dynamics is of great importance, hence the shaft speed rate of the thrusters must be judiciously modeled. This is implemented by Perez and Fossen (2009) using an integrator in a feedback loop in a first order system[1]. The tuning of this system is done by varying the time constant (tc). The goal is to mimic the thruster reaction time described in Section 4.2.2. This SIMULINK saturation element is presented in Figure 5.1.

[1] Using a first order system will not produce the perfect linear behavior that the shaft speed should have, but by implementing a second order system, the damping could lead to a delay in the system.

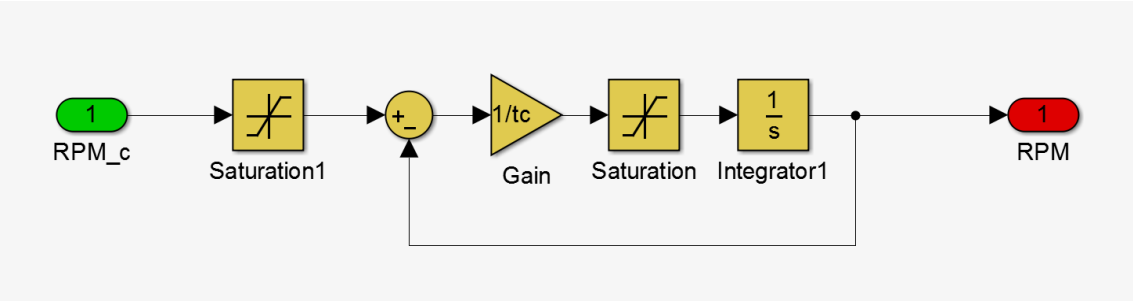

Figure 5.1: Shaft speed saturation element.

5.3 Thruster allocation

The thrusters are modeled to work in pairs, i.e. one bow thruster with one Azipull thruster. There are two reasons behind this set-up, firstly so that it has the same amount of counteracting moment in both directions. Secondly, the thrusters will give the same contribution in sway and yaw. The two pairs are pointing in the opposite direction of the roll motion. The inclination angle is defined as positive (right) and negative (left), thus two thrusters will constantly produce positive thrust and the other pair will produce negative thrust with respect to each other. To model this effect the saturation limits for the positive acting thrusters were defined as max= max RPS, and min = thruster limit. The negative acting thrusters were arranged as max= - thrusters limit and max = - max RPS. This is illustrated in Figure 5.2. Note also that both the positive and the negative acting thrusters have the same input control signal. This is because the thruster pairs will increase and decrease the shaft speed at the same time, thus gaining the optimal thrust for roll damping. The SIMULINK thrust allocation can be found in Appendix B.2.

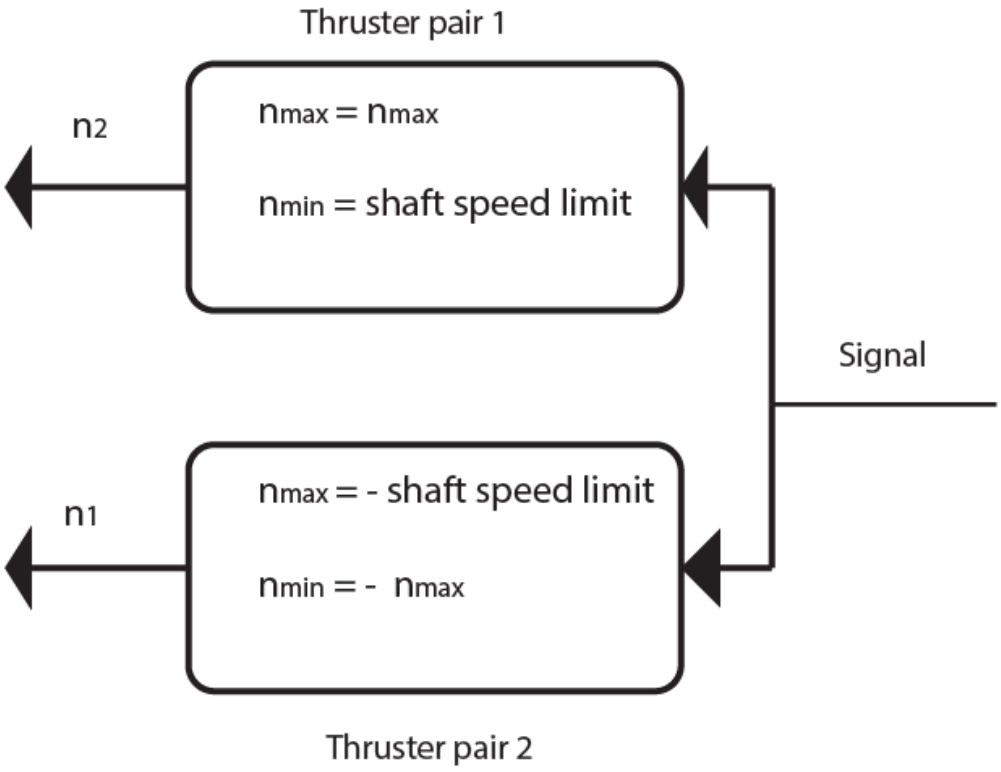

Figure 5.2: Shaft speed allocation.

5.4 Tuning

The tuning of the nonlinear PD-controller can be done by varying the gains K_P, K_D, and c. An optimization algorithm is proposed to find the optimal gains.

5.4.1 Optimization

A particle swarm optimization (PSO), see Kennedy and Eberhart (1995), algorithm was chosen to identify the most suitable gains and thruster limits.

The algorithm assigns each particle a random position in the search space (x) and a random velocity (v). The positions and velocities are updated for each iteration (k) for all the *i*the particle using the following equations

$$\mathbf{x}_{k+1}^{i} = \mathbf{x}_{k}^{i} + \mathbf{v}_{k+1}^{i} \tag{5.3}$$

$$\mathbf{v}_{k+1}^{i} = \omega \mathbf{v}_{k}^{i} + \underbrace{\phi_p r_p(\mathbf{p}_k - \mathbf{x}_k^i)}_{\text{CVC}} + \underbrace{\phi_g r_g(\mathbf{p}_k^g - \mathbf{x}_k^i)}_{\text{SVC}}, \tag{5.4}$$

were ω is a so called inertia parameter, which scales the previous particle velocity. Additionally this parameter is dynamic, meaning that it will narrow towards the optimal solution through the optimization process. The parameters ϕ_p and ϕ_g denote user set scaling parameters which define how much the particles are dependent on the swarm and themselves. Furthermore, $\mathbf{p}_k^i$ represents the *i*th particle and $\mathbf{p}_k^g$ is the particle containing the most optimal solution for the iteration *k*. This particle will redirect the swarm towards its location, Ehlers (2012). The r_p and r_g represents random number in the interval r_p, $r_g \in [0,1]$.

The velocity components in (5.4) can be broken down into two categories, namely the *cognitive velocity component* (CVC) and the *social velocity component* (SVC). The former represents the difference between the *i*th particle and the currently best-known particle in the *k*th iteration. The latter represents the difference between the *i*th particle and the global best known, i.e. the best through the entire optimization process. These results are then used as an input to the objective function, which is updated accordingly. The optimization process ends when the prescribed number of iterations is reached. The PSO implementation used in the current paper is written in MATLAB, and is a modified version of Ehlers (2012) and Jalkanen (2006). The optimization parameters are listed in Table 5.1. The optimization parameters are listed in Table 5.1.

Table 5.1: PSO parameters

Particle swarm size	20
Number of iterations	20
ϕ_p	2
ϕ_g	2
Inertia (ω) at the beginning	1.4
Inertia reduction factor	0.8
Number of rounds to improve the results before the inertia is reduced	4

Chapter 6: Ship Roll Motion Performance

There are several ways to delineate the performance of roll damping systems, and they often differ between manufacturers. Perez (2005) discusses the following measurement of roll damping performance:

- Percentage Reduction of Roll at Resonance (RRR).
- Percentage Reduction of Statistics of Roll (RSR).
- Percentage Reduction of Probability of Roll Peak Occurrence (RRO).
- Percentage of Time Operable (PTO).

This section will consist of a brief explanation of the four different measurement of performance. Several statistical distributions will be discussed and are referenced to Bury (1975).

6.1 Reduction of roll at resonance

A common figure of performance is described as the reduction of the roll motion at the resonant frequency for regular beam waves. This method is according to Perez (2005) deterministic and will not present the real roll reduction but an overestimate. The roll reduction at resonance (RRR) are described by the following formula:

$$\text{RRR} = \frac{\eta_{4_u} - \eta_{4_s}}{\eta_{4_u}} \times 100\%, \tag{6.1}$$

where subscript u represents the response amplitude at resonance without any damping system active, and subscript s represents the amplitude when the damping system is active.

6.2 Reduction of statistics of roll

In order to get a realistic measurement of the roll motion, the roll motion is described in a more pertinent matter by using roll peak statistics, since in a realistic scenario irregular waves from different sea states will excite the vessel. The typical statistical properties used for roll motion performance are listed below.

- Standard Deviation (STD).
- Root Mean Square (RMS).
- Significant roll amplitude (η_{4_S}).
- Maximum roll amplitude.

The significant roll amplitude is calculated the same way as for waves, hence it represents the one-third of the largest peaks that occur in the time series.

6.3 Reduction of probability of roll peak occurrence

Often certain operations can not be carried out in a condition that exceeds a certain roll amplitude. Thus is it relevant to calculate the probability of not exceeding a certain roll limit. Perez (2005) describes that the roll motion of ships can be described as a narrow-banded Gaussian stochastic process since the wave excitations can be a realization of a narrow-banded Gaussian process. Thus, Rayleigh density functions can represent the roll amplitude peaks according to Price and Bishop (1974):

$$P_{R_{PDF}} = \frac{\eta_4}{\sigma^2} e^{-\frac{\eta_4^2}{2\sigma^2}}, \tag{6.2a}$$

$$P_{R_{CDF}} = 1 - e^{-\frac{\eta_4^2}{2\sigma}}. \tag{6.2b}$$

It was decided to illustrate this further by looking at the response spectrum, which is calculated by the square of the RAO multiplied by the wave spectrum, Equation 6.3. The response spectrum is illustrated along with the wave spectrum and the Roll RAO in Figure 6.1.

$$S_{XX}(\omega) = [RAO(\omega)]^2 \cdot S_{wave} \tag{6.3}$$

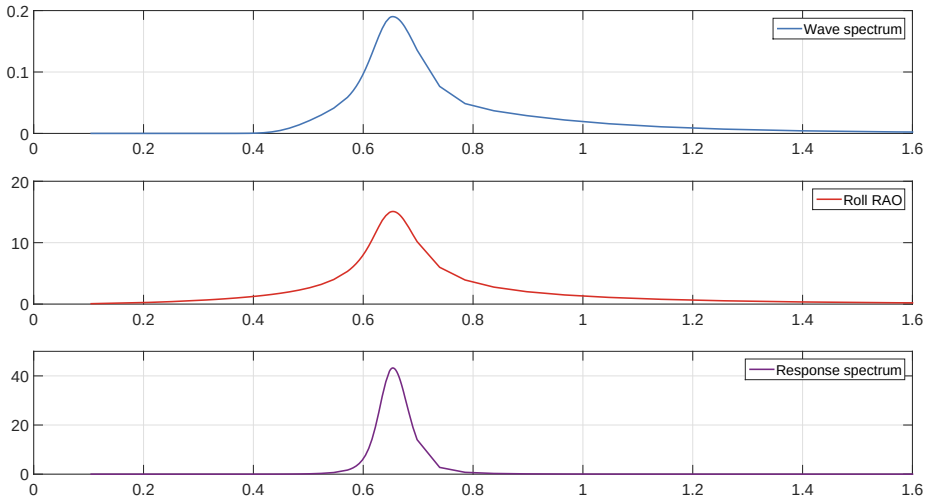

Figure 6.1: Wave spectrum, roll RAO and response spectrum.

From the Figure 6.1, it was unclear whether the response was as narrow-banded as is required in order to use Rayleigh density functions to describe the roll peaks. Therefore a comparison study was carried out to compare the Rayleigh and Weibull cumulative density functions (CDF), Equations 6.2b and 6.4b.

$$P_{W_{PDF}} = \frac{k}{\lambda}(\frac{\eta_4}{\lambda})^{k-1} e^{-(\frac{\eta_4}{\lambda})^k}, \tag{6.4a}$$

$$P_{W_{CDF}} = 1 - e^{-(\frac{\eta_4}{\lambda})^k}, \tag{6.4b}$$

where k is the shape parameter and λ is the scale parameter. The CDF comparison between Rayleigh and Weibull representation are presented in Figure 6.2, where the sampled roll peaks are represented with yellow scatter.

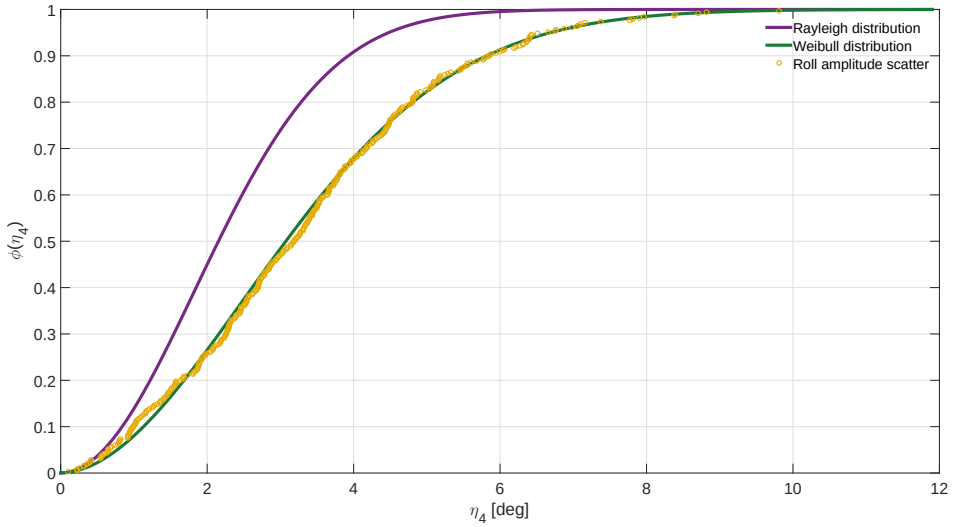

Figure 6.2: Comparison between Rayleigh and Weibull representation of the roll peaks.

The figure clearly depicts that a Weibull representation is more suited for representing the roll peaks, especially since the Rayleigh distribution shows a non-conservative representation.

6.4 Reduction of probability of max roll peak occurrence

The statistical representation discussed in the previous section will only be valid for roll peaks during a time series. If the requirements are strictly limiting a vessel from not experiencing roll angles higher than a certain limit in a given sea state, e.g. Helideck Certification Agency (2016)

request roll lower than 3°, must other methods be used. A given sea state will not provide the same wave realization, thus different maximum can occur even though the sea state remains the same. Common practice in wave statistics is to use different wave realizations using a variety of seeds and sample the maximum for each wave realization, and represent them with a Gumbel distribution. The same approach is used for roll response in this thesis. Figure 6.3 clearly shows that Gumbel is a good representation of the extreme values. By taking the 95 percentile from the Gumbel CDF one can by 95% certainty say that the roll response will be below the requested criteria for a given sea state.

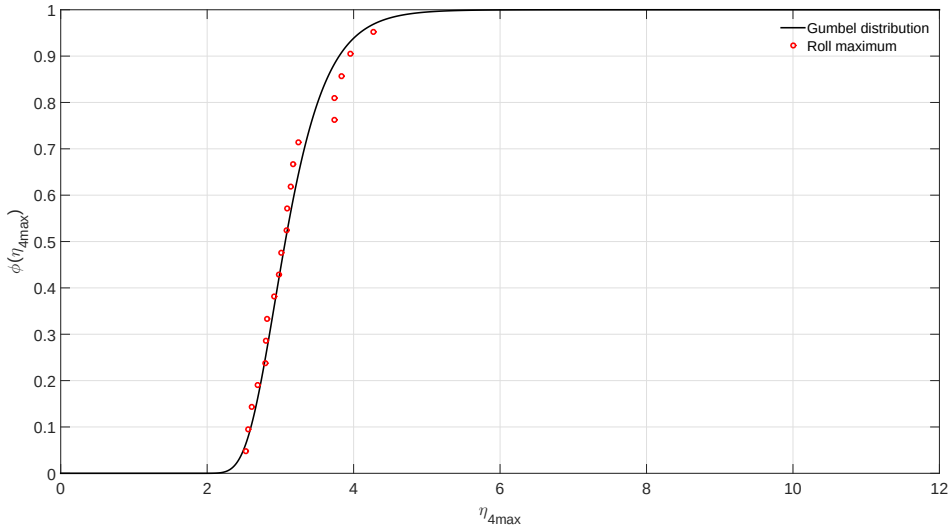

Figure 6.3: Gumbel distribution representing the maximum roll angles for 20 seeds.

6.5 Percentage of time operable

Most marine operations has performance indices (PI). These indicate certain constrains to the operations, e.g. motion sickness, maximum roll angle, accelerations, and propeller emergence. Different operations have a variety of indices, and they are evaluated at their respective Operability Limits (OL), e.g roll less than 3° the last 20 minutes. The Percentage of Time Operable (PTO) for a zero-speed case[1] are calculated using the summed probability that a sea state will occur.

[1] For a non-zero-speed case, the probability of speed be must included.

6.6 Operation Criteria

As stated in the introduction several marine operations request stable and low roll motions. In the following section, some examples of criteria are presented.

According to Crossland (2003) and Monk (1987) crew-members had a reduced ability to carry out tasks about 20-30% for RMS roll 6° and 50 % when the lateral acceleration was equal to 0.07 g.

A frigate operating in the North Atlantic had the following mission criteria for anti-submarine warfare (ASW) concerning roll and pitch motion, (Crossland, 2003, Table 1). If one of the criteria is exceeded, the operation is considered not operational.

Table 6.1: North Atlantic operating frigate's mission criteria.

	RMS Roll	**RMS Pitch**
Personnel, bridge	4.0°	1.5°
Torpedo launch	3.8°	3.8°
Helicopter launch	2.5°	1.5°

In Norway the criteria for landing helicopters on small vessels requests for 2° or 3° in roll and pitch depending on the helicopter type, Helideck Certification Agency (2016).

Table 6.2: Helideck limitations list related to roll and pitch motion. P/R represents pitch and roll.

Vessel category / Aircraft category	Stern mounted helideck	Bow mounted helideck
	P/R	P/R
A	2.0°	2.0°
B	3.0°	3.0°

Part II

Experimental Trials

To get verify the simulation results the decision was made to carry out model tests using a model with scale 18.319, see Table 6.3 and Figure 6.4. The experiments were carried out in MARINTEK's towing tank and lasted for one week.

Table 6.3: Particulars of the model M-3124B used in the model tests.

	Unit	**Full-scale**	**Model-scale**
Lpp	m	98.73	5.389
B	m	21	1.146
D	m	6	0.328
Δ	tons, kg	9003.0	1428.8
KG	m	7.38	0.403
GM	m	2.455	0.134

The following sections are arranged as follows. The experimental setup is covered in Chapter 7. Uncertainty estimation is described in Chapter 8. Lastly, the final results of the seakeeping trials related to roll motion and a discussion of these results are presented in Chapter 9. The results presented are found from the binary files included in the electronic Appendix, see Appendix E for more information.

Figure 6.4: Ship model 3124 B ready for testing.

Chapter 7: Experimental Setup

Since this study was conducted in order to determine whether the thrusters could be used to damp roll motions actively, springs were attached to the model, constraining the model from surge, sway, and yaw motions. Moreover, the model was equipped with two Azipull thrusters in the stern and two bow thrusters in the bow. In order avoid making holes in the model, a platform was constructed to carry the bow thrusters, see Figure 7.1. The bow thrusters were placed at the same height as the bow thrusters should be placed, thus giving the same counteracting moment as it would in a real scenario.

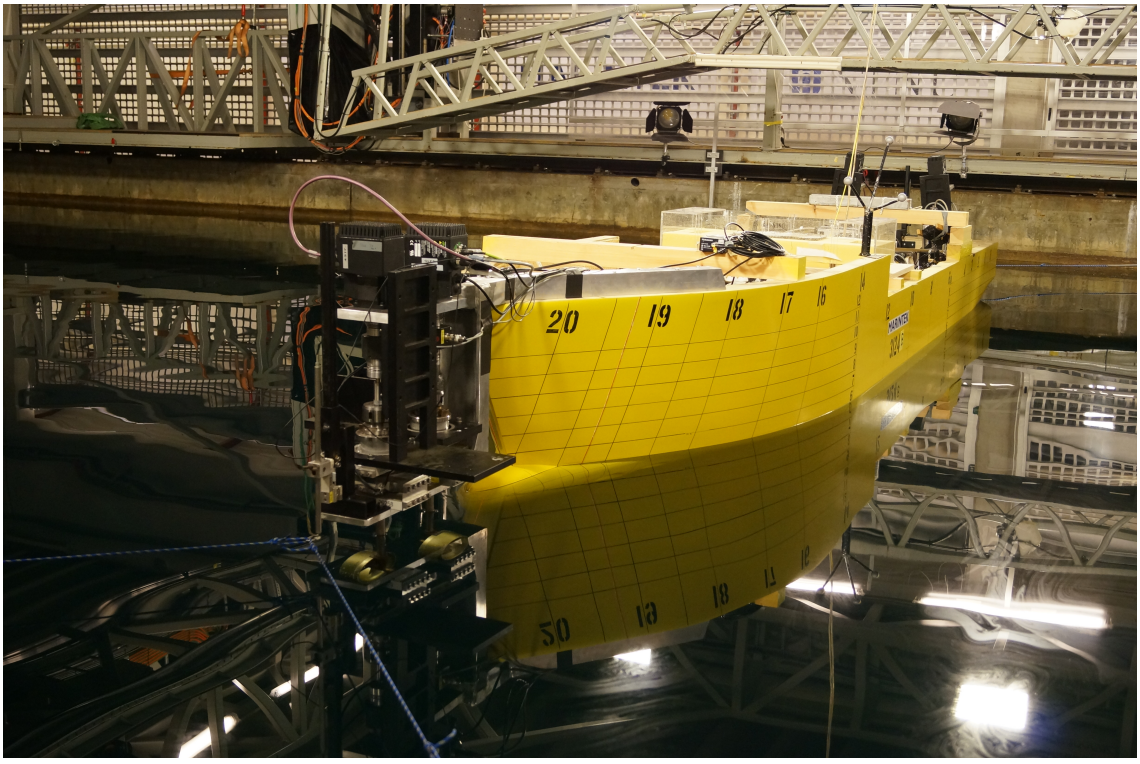

Figure 7.1: Bow thruster platform.

The model was equipped and calibrated by MARINTEK personnel. The most important measurement equipment consisted of force actuators in X and Y direction, shaft speed, Azipull rudder, 6 DOF measurements, roll pitch and yaw rates, and wave measurements. The different channels can be found in Appendix E.1. The entire model is illustrated in Figure 7.2.

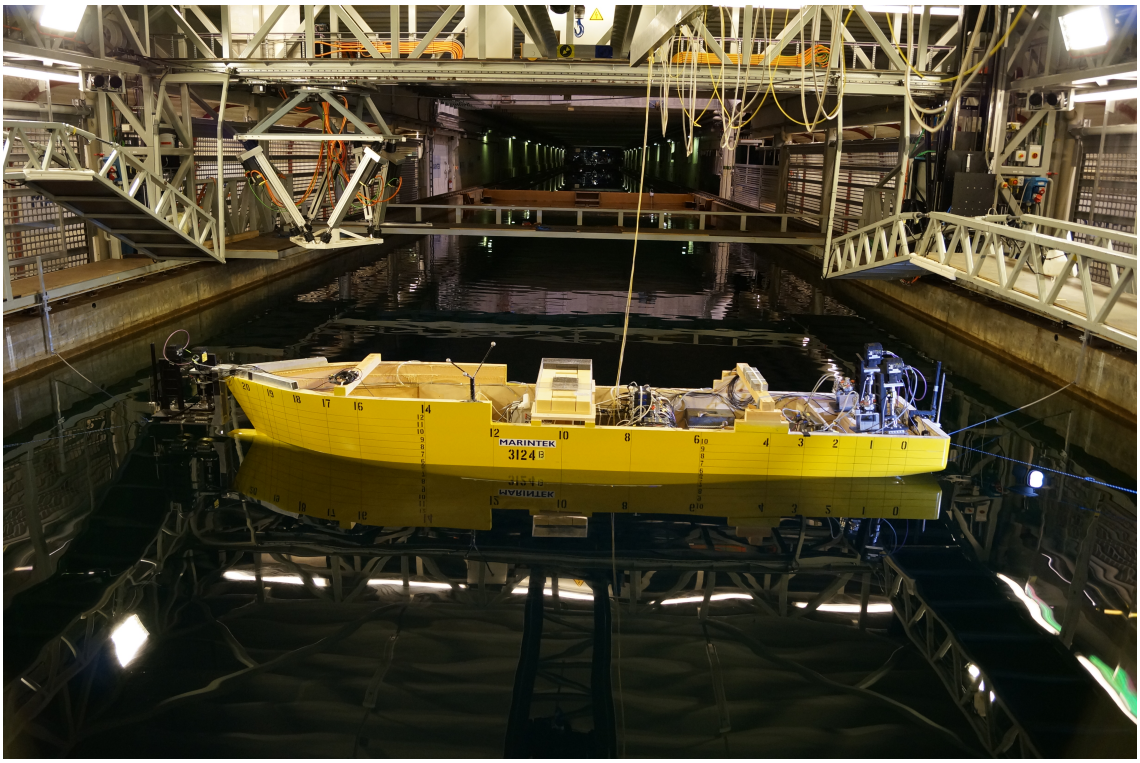

Figure 7.2: Experimental setup.

7.1 Weight data

After the model had been weighted, it was important that the weight, draught, center of gravity (COG), and the metacentric height (GM) were scaled correctly. MARINTEK personnel did this by first scaling the weight, then distributing the weights in a manner that meets all the above-mentioned requirements, see Table 6.3. The GM is found from inclination tests. This is accomplished experimentally by moving weight along the ship's transverse axis and measure the static heel angle with a pendulum, this is described by Equation (7.1).

$$GM = \frac{wal}{\nabla u}, \tag{7.1}$$

where w represents the weight that is moved, a is the arm of the displaced weight, l represents the length of the pendulum ∇ is the vessel's weight displacement, and u is the difference in the pendulum deflection between starboard and port. The final results from the weight measurements are described in Table 7.1

Table 7.1: Experimental weight data found by inclination tests.

Description	**Unit**	**Full-scale**	**Model-scale**
Displacement	tons, kg	9003.0	1428.8
KG	m	7.38	0.403
XCOG	m	42.303	2.309
GM	m	2.455	0.134

7.2 Open water tests

Prior to the seakeeping tests, open water tests were carried out. The purpose of these tests was to study the performance of a propeller working without a hull present. The necessary theory and equations are described in Section 2.7.

There are several ways of conducting open water tests. The most commonly used approach, which was used in this case, is to keep the propellers at constant shaft speed and towing the propeller with velocities in the regime where the propellers most likely will operate. Before these test could be carried out, determining the maximum shaft speeds for the thrusters was required. The maximum shaft speeds were found by calculating the bollard pull thrust for the full-scale propellers and scaled to model scale. Since the thrusters should be used during DP, a thrust reserve is kept for this purpose. The reserve was set to 25% less thrust for both the Azipull and the bow thrusters. The results from the scaled bollard pull thrusts with and without thrust reserve are represented in Table 7.2.

Table 7.2: Bollard pull thrust scaling.

		Full-scale	Model-scale	Model scale with thrust reserve
Bollard pull Azipull Thruster	T_{0_A}	327 kN	52 N	39 N
Bollard pull Bow Thruster	T_{0_B}	181 kN	29 N	22 N

After the bollard pull thrusts had been found, the maximum shaft speed could be found by keeping the propellers stationary while the shaft speed increased until the thrust reached the requested bollard pull thrust. This is illustrated in Figure 7.3 and 7.4. From the figures, one can see that the regression lines are perfect with the square of the shaft speed, which was discussed in Section 4.2.2. The maximum shaft speed was found to be 11 RPS for the Azipull thrusters and 13.6 RPS for the bow thrusters.

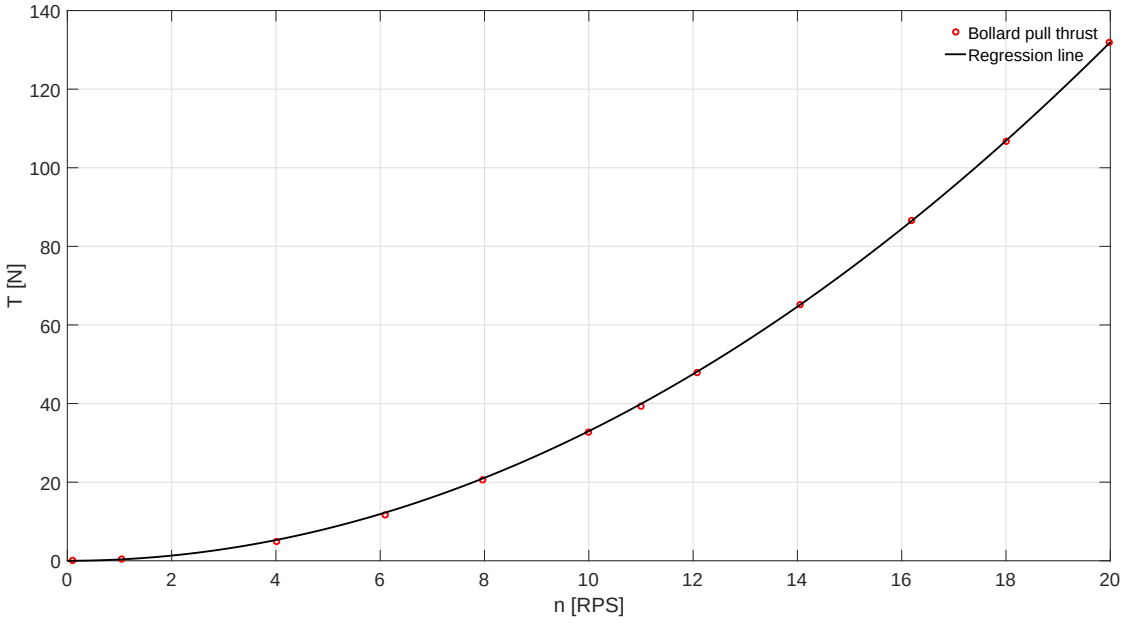

Figure 7.3: Bollard pull thrust with respect to shaft speed for Azipull thrusters.

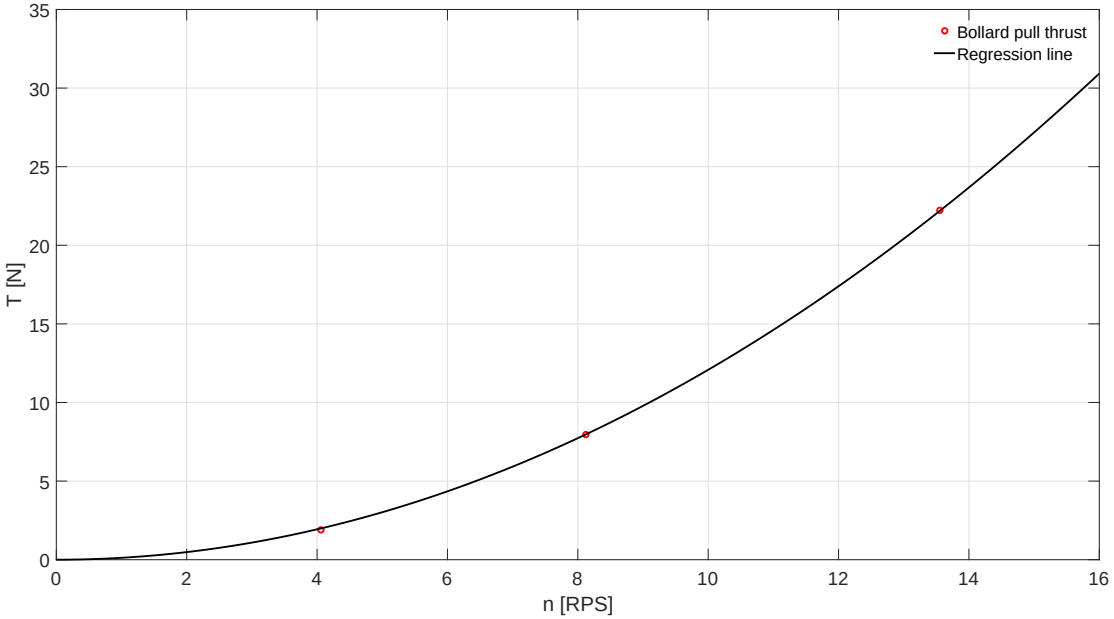

Figure 7.4: Bollard pull thrust with respect to shaft speed for bow thrusters.

After the maximum shaft speeds were available, the open water characteristics could be found by towing the propellers with different speeds. This is depicted in the two figures below where open water tests are carried out for shaft speed 30%, 60% and 100%. Note that the shaft speeds presented are related to the bollard pull with thrust reserve.

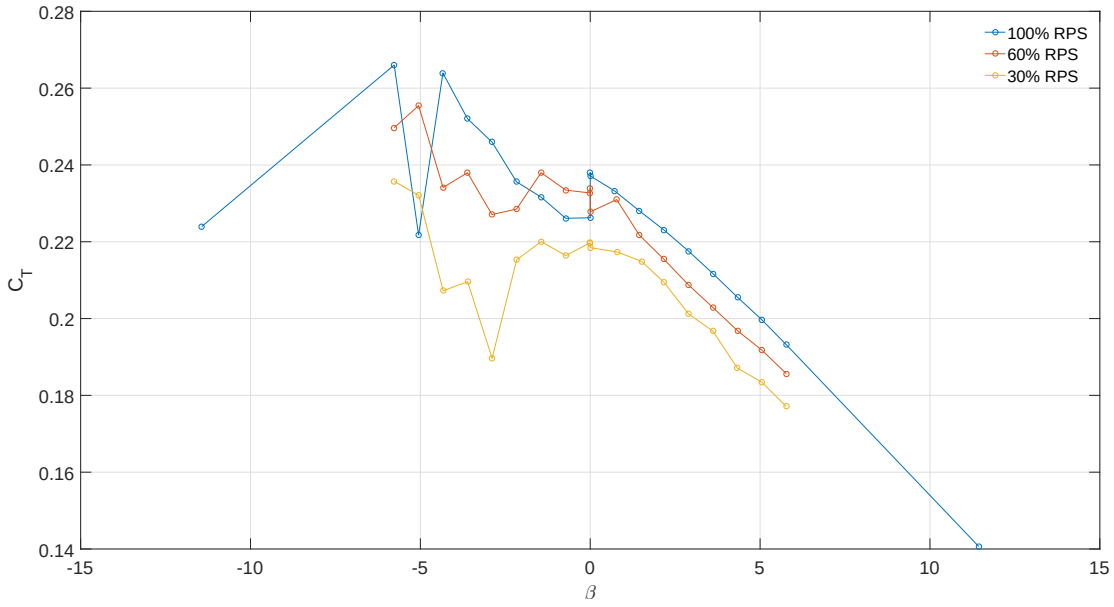

Figure 7.5: Open water results for Azipull thrusters.

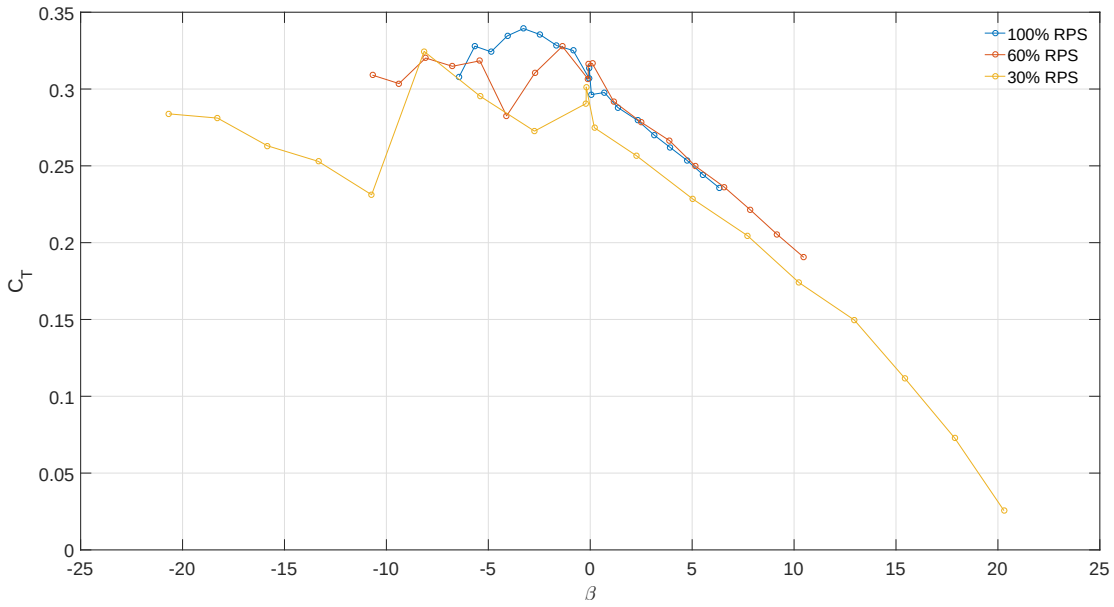

Figure 7.6: Open water results for bow thrusters.

From the figures one can easily see that the non-dimensional thrust coefficient is varying with both β and the shaft speed. Later it was found that the L-method, presented in Section 2.7.3, was a good fit to the open water results.

7.3 Spring stiffness

As mentioned above, the vessel was equipped with springs in the fore and aft of the vessel. The spring stiffness was not given, therefore was the stiffness calculated by using a sway decay test. The sway and the summed Y-forces from the fore and aft force transducers connected to the springs are plotted in Figure 7.7. Linear regression was used to find the total spring stiffness (144.8 N/m), the results from the regression can be found in Figure 7.8.

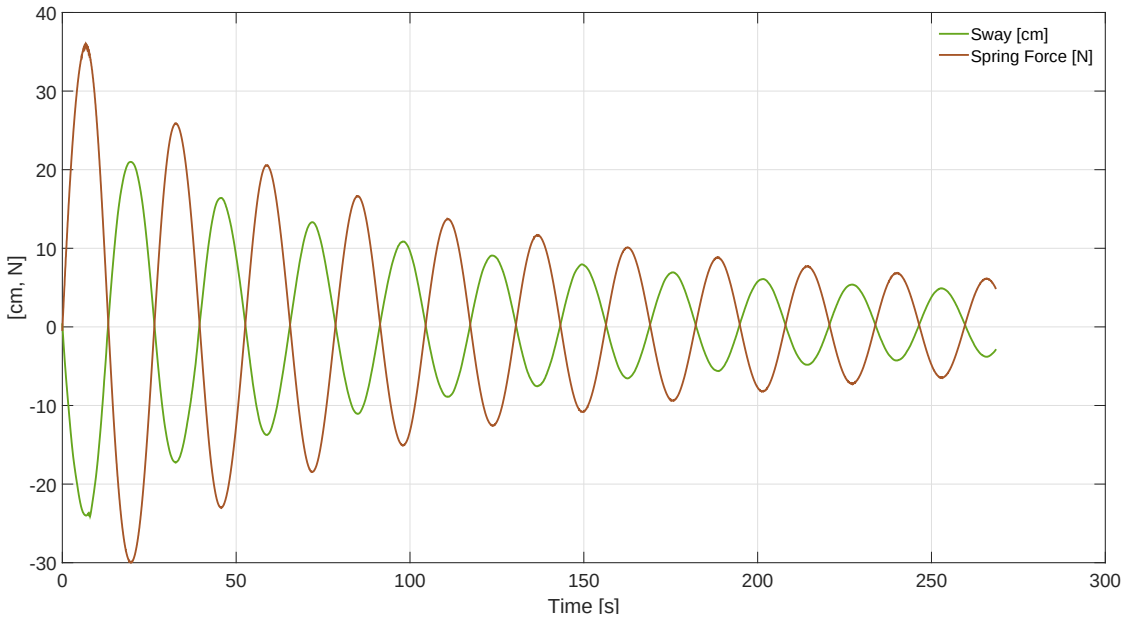

Figure 7.7: Sway motion and spring forces during a sway decay test.

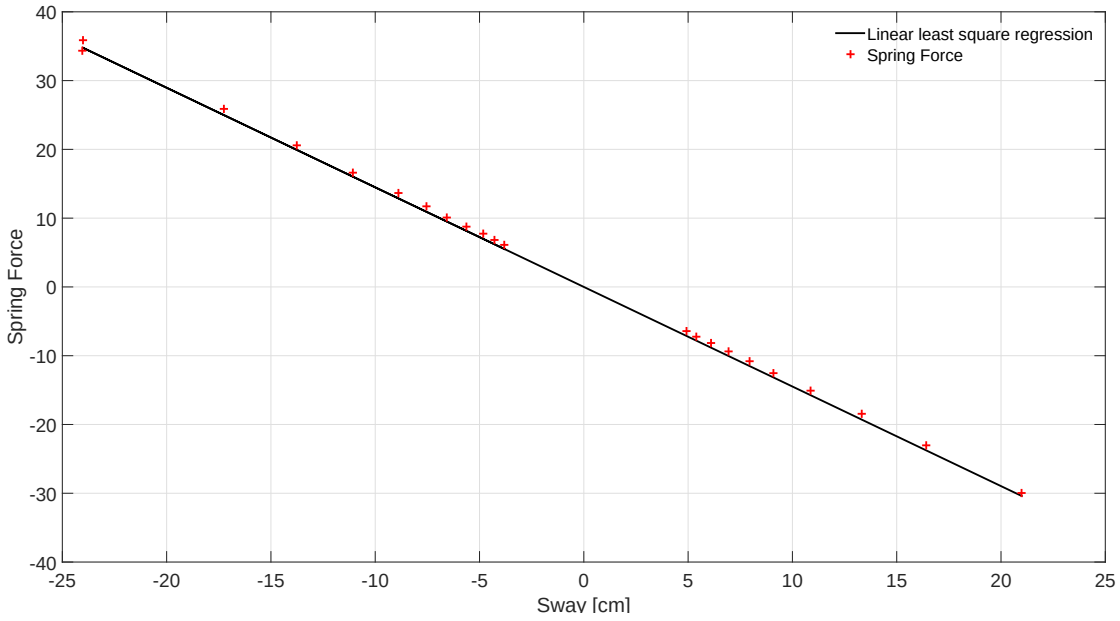

Figure 7.8: Spring stiffness found by linear regression k=144.8 N/m, R^2=99.

7.4 Wave calibration

The waves used in the experiment consisted of five regular and three irregular waves. The calibration was done by MARINTEK personnel, by using a wave probe at the same location as where

the model would be placed, thus measuring the same waves that will occur during the experiments. All the wave parameters and values, i.e. wave period and amplitude, except real time, are represented in full scale. The results from the regular wave calibrations are presented in Appendix D.1 and the irregular waves are shown in Appendix D.2.

7.5 Rudder angle

The bow thrusters are placed side by side in the longitudinal direction, and will not experience thruster-thruster interaction. The Azipull thrusters are placed side by side in the transverse direction, one pointing to starboard the other pointing to port, thus will the thrusters blow against towards each other, and thruster-thruster interaction might occur. The Azipull rudders can be rotated 360°, hence having a broad range of possible rudder positions. It is a trade-off between rudder angle and roll damping since as much thrust as possible should be given in the transverse direction. Furthermore, one would not like to have substantial thrust in the longitudinal direction since the vessel will move in that direction. A decay study with constant thruster shaft speed was performed to investigate the rudder angles 70-120°where the one Azipull thruster has positive rudder angles, and the other has negative, thus will the thrust contribution be equal in longitudinal and transverse direction. The results from the decay tests are presented in Figure 7.9.

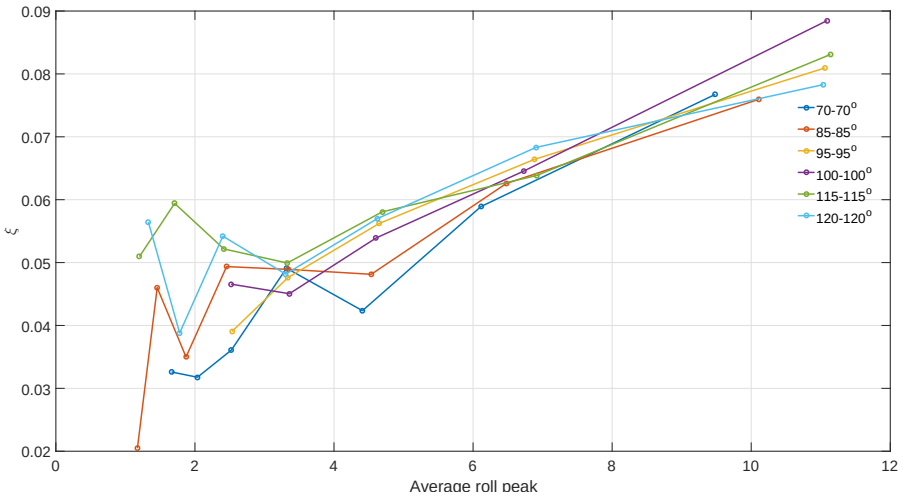

Figure 7.9: Damping ratio for different rudder angles.[1]

[1] 90-90°is not represented since the results was not properly sampled.

The results depict that angles below 95°, in general, give less damping. The average damping ratio was 2% higher for 100°and 115°than 95°, which is not a large improvement. Thus, is 95-95°chosen because this will give the smallest thrust in longitudinal direction.

7.6 Control and thruster configuration

The thrusters were controlled by SIMULINK using User Datagram Protocol (UDP) input and output. The output signal was sent to another computer which controlled the thrusters. The data was sent and received by single precision, therefore two MATLAB blocks were added to convert the input signal to double precision to perform the calculations, then converting the signal back to single precision. This was implemented because SIMULINK calculates with double precision. The tuning parameters c, K_A, and K_R was added as constants outside the control system, in order to carry out tuning during experiments. The optimal gains were found by first running numerical simulations, and then finely tuning the parameters using experimental decay tests. The control parameters found are presented in Table 7.3.

Table 7.3: Control parameters used during the experiments.

Description	**Control parameter**	**Value**
Linear roll acceleration gain	K_A	1000
Nonlinear roll rate gain	K_R	1546
Denominator	c	6.57
Lower shaft speed limit	LSSL	22.3%

Manuel switches were also added, to be able to switch easily between no propeller action, with constant shaft speed, and active roll control. The propeller shaft speed and associated rates were saturated with propeller shaft speed blocks, see Section 5.2.1 and 5.3. The SIMULINK system is illustrated in Figure 7.10.

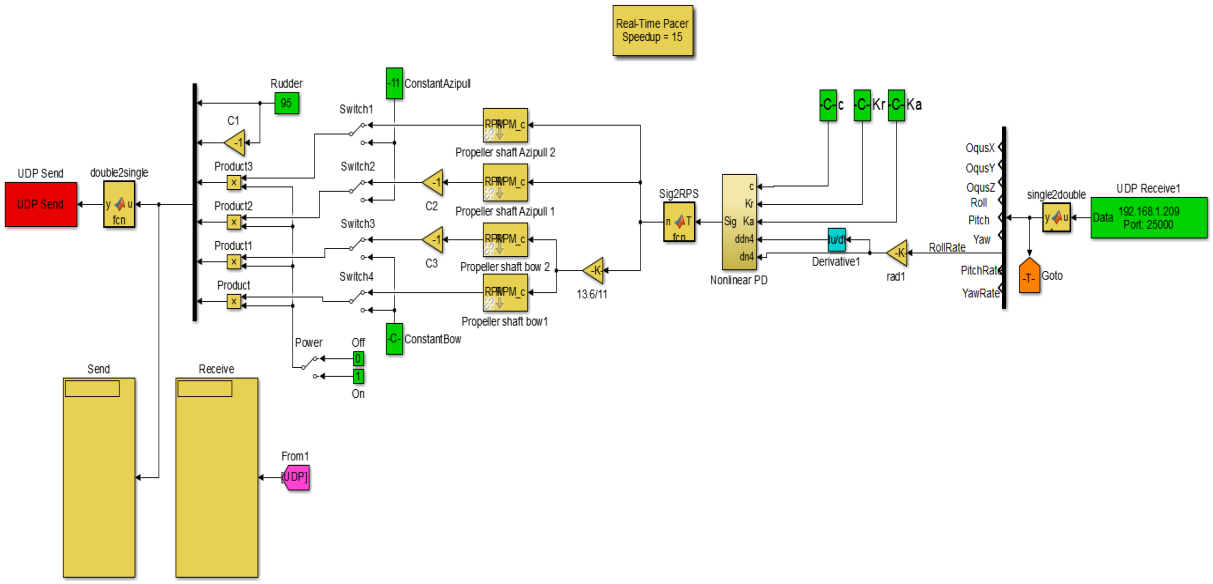

Figure 7.10: SIMULINK UDP setup.

The model thrusters could not control the propeller pitch. To overcome this problem, the reaction time was set to the reaction time if one had both pitch and shaft speed control. Furthermore, the shaft speed would be constrained to give the same lower thrust limit. In other words, the thrusters were modeled in such a way that the shaft speed rates were faster than what they were supposed to be. This can be exemplified by fixing the lower shaft speed to limit, e.g 30%. Furthermore, this value is used to find the same thrust when both shaft speed and pitch control is utilized. This point can be used to calculate the reaction time. This procedure is illustrated graphically with stippled lines in Figure 7.11.

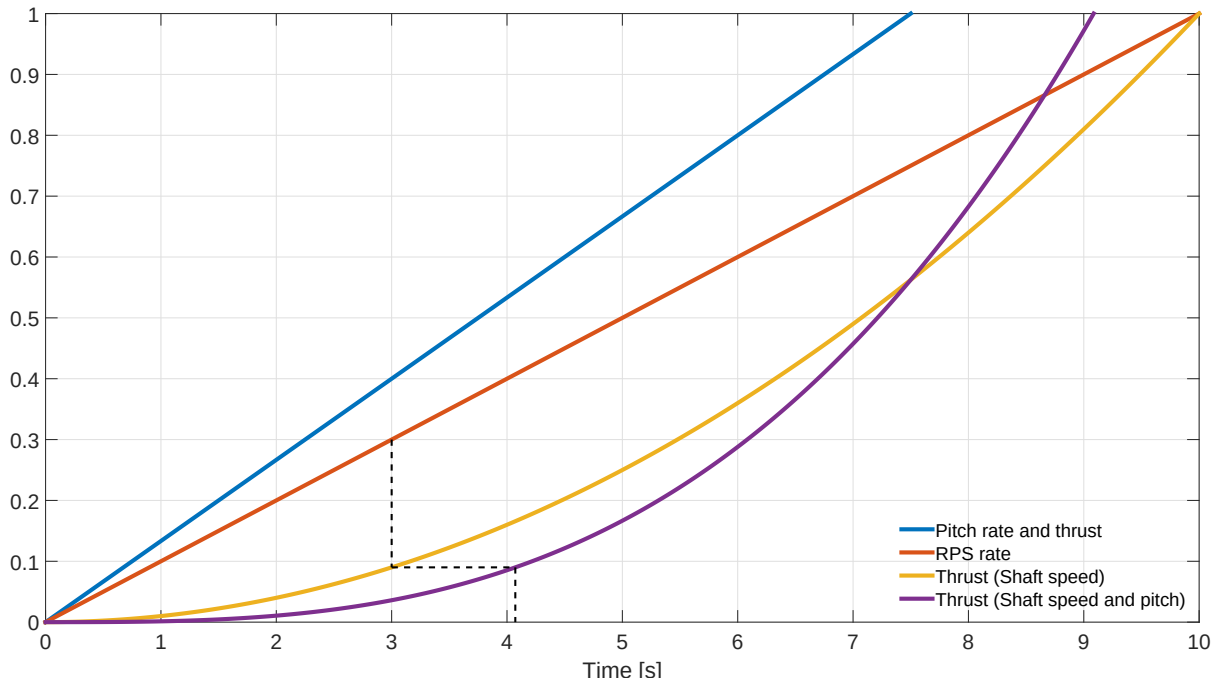

Figure 7.11: Thruster reaction time representation.

Chapter 8: Uncertainty Estimation

Error is defined as the difference between the measured results and the true value. However, it is impossible to attain the true value, thus an estimation of error is needed. Error analysis is typically divided between the two categories; *bias* and *precision errors*. The former represents all the systematic errors that may take place during experiments, which can not be determined by repetitions. Furthermore, the bias error can be reduced by calibration, and by increasing the number of factors included in the repeated experiments used to find the precision error. Precision error represents the error in the scatter of the results, and is revealed by repeating the experiments.

8.1 Bias error estimation

The largest bias errors in experimental trials are wave reflections and the waiting time between the trials. After the waves meet the wave beach, some waves will be reflected towards the model, thus causing disturbing waves. Furthermore, the waiting time between the experiments can also be the reason behind discrepancy in the results. Calm water was estimated by eye during the experiments.

8.2 Precision error estimation

The precision error is estimated using Student's t distribution. The distribution is similar to Gaussian distribution, the main difference is that Student's t distribution has longer tails. The

precision error can be calculated as

$$e_p = t_{\alpha/2,\nu}\sigma, \tag{8.1}$$

where α is defined as $\alpha = 1 - c$, c is the confidence interval (0.95 is used here), and ν represent the degree of freedom defined as $\nu = N - 1$, and N represents the number of samples. Finally σ represents the standard deviation given as

$$\sigma = \sqrt{\frac{1}{N-1}\sum_{j}^{N}(x_j - \mu)^2}, \tag{8.2}$$

where μ is the mean of the repetitions.

The following chapter presents the results as well as the precision error estimation for the two different sea trials; regular waves and irregular waves. Decay is difficult to estimate the error since it is oscillated by hand, and will thus sample different roll peaks. The error is estimated for the cases that have five or more repetitions. Because of the time constraints and the fact that during some results the measurement equipment failed, not all cases have sufficient amount of repetitions to say anything about the error.

Chapter 9: Experimental results

In the following chapter the seakeeping trials: decay tests, regular waves, and irregular waves are presented with related precision error described in Section 8.2. Moreover, the seakeeping trials will differentiate between no roll damping (NRD), constant shaft speed (CSS), and active roll damping (ARD). The latter have the control parameters presented in Table 7.3. Furthermore, the predicted power and fuel consumption will be presented and compared to helicopter operations. Lastly, the center of roll and open water characteristics are discussed. The All the results are referenced to the electronic Appendix E.

9.1 Decay tests

The decay tests were executed by oscillating the model back and forth by hand until it reached a sufficiently large roll angle. The vessel was then released and the roll motions were sampled. The first, i.e. the largest roll amplitude, was ignored due to transient effects, Steen (2014a). Since the vessel is excited using non-measured force, i.e. by hand, will the decay be different for all repetitions.

The theory used to calculate the damping ratio is described in Section 4.1.1. The linearized nonlinear damping term was calculated for the cases; No Roll Reduction (NRD), Constant Shaft Speed (CSS) and with Active Roll Damping (ARD). The measurements from the experimental trials for the three mentioned tests are illustrated in the following three subsections.

9.1.1 No roll damping

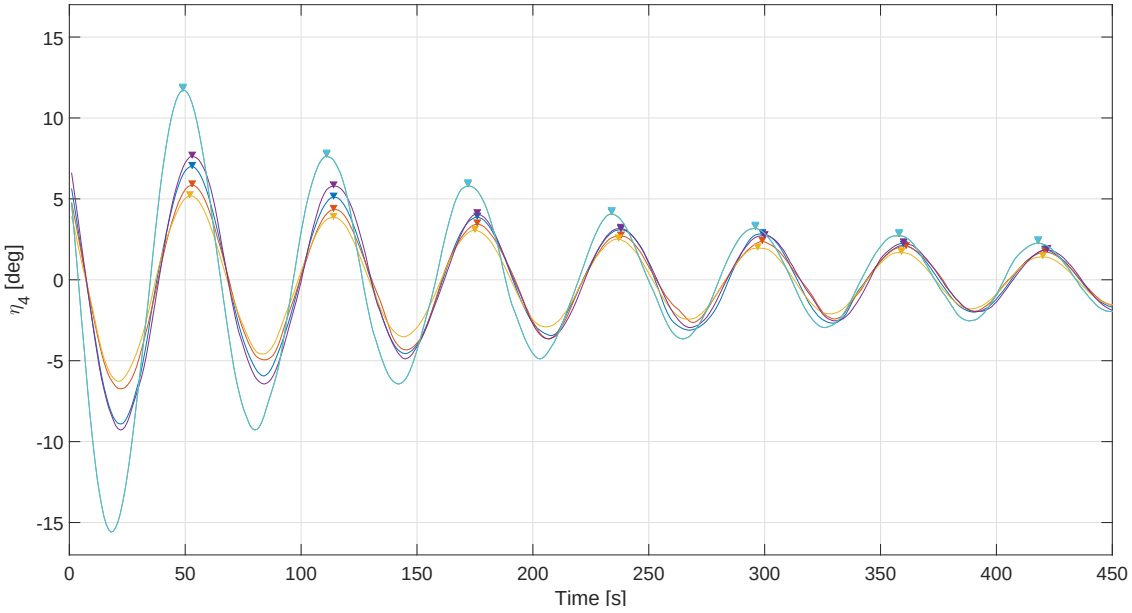

Figure 9.1: Measured response from decay tests with no roll reduction.

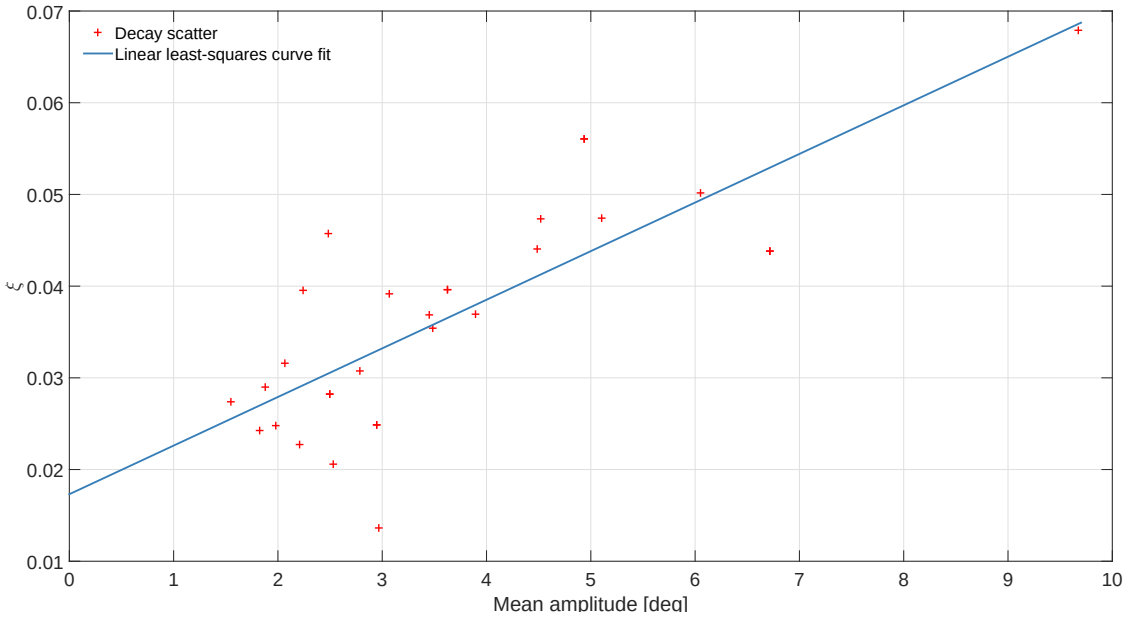

Figure 9.2: Measured damping ratio from decay tests with no roll reduction.

9.1.2 Constant shaft speed

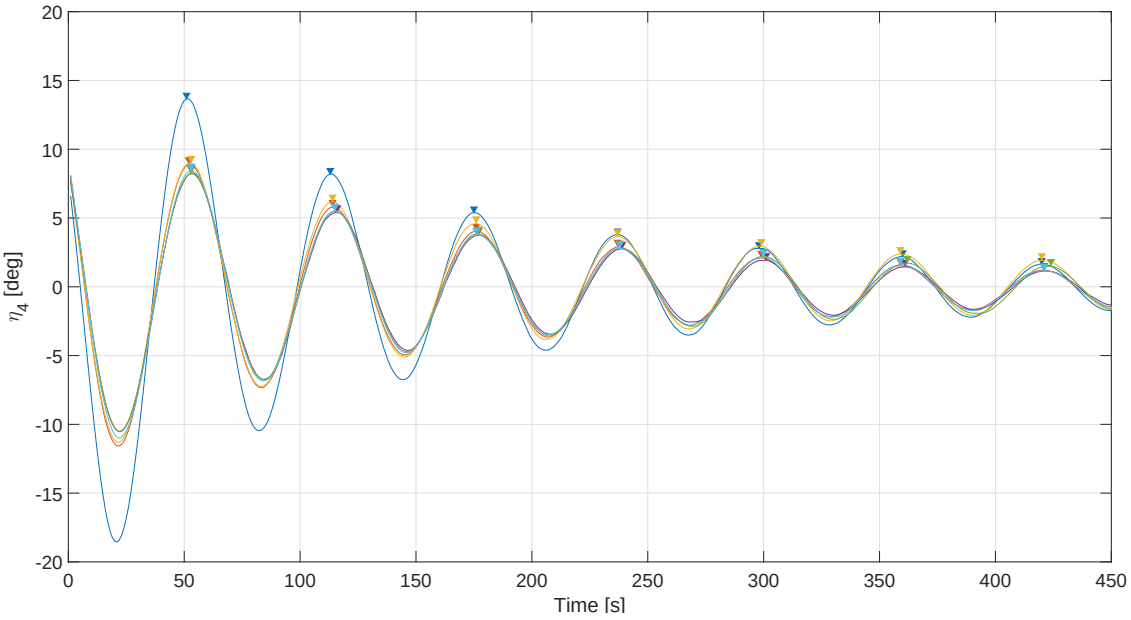

Figure 9.3: Measured response from decay tests with constant shaft speed damping.

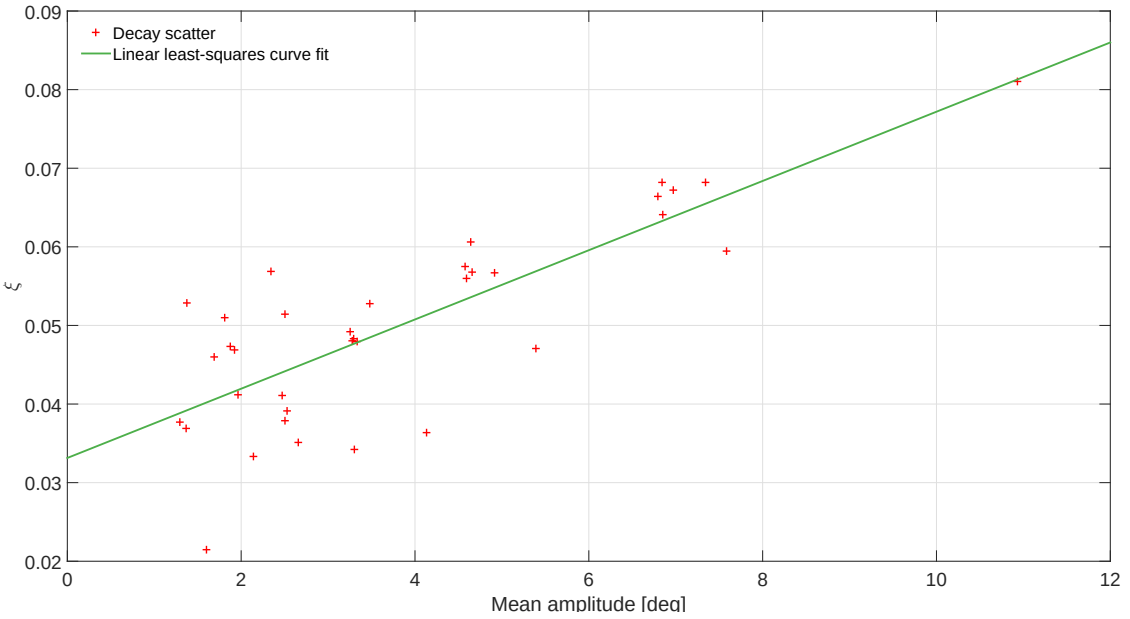

Figure 9.4: Measured damping from decay tests with constant shaft speed damping.

9.1.3 Active roll damping

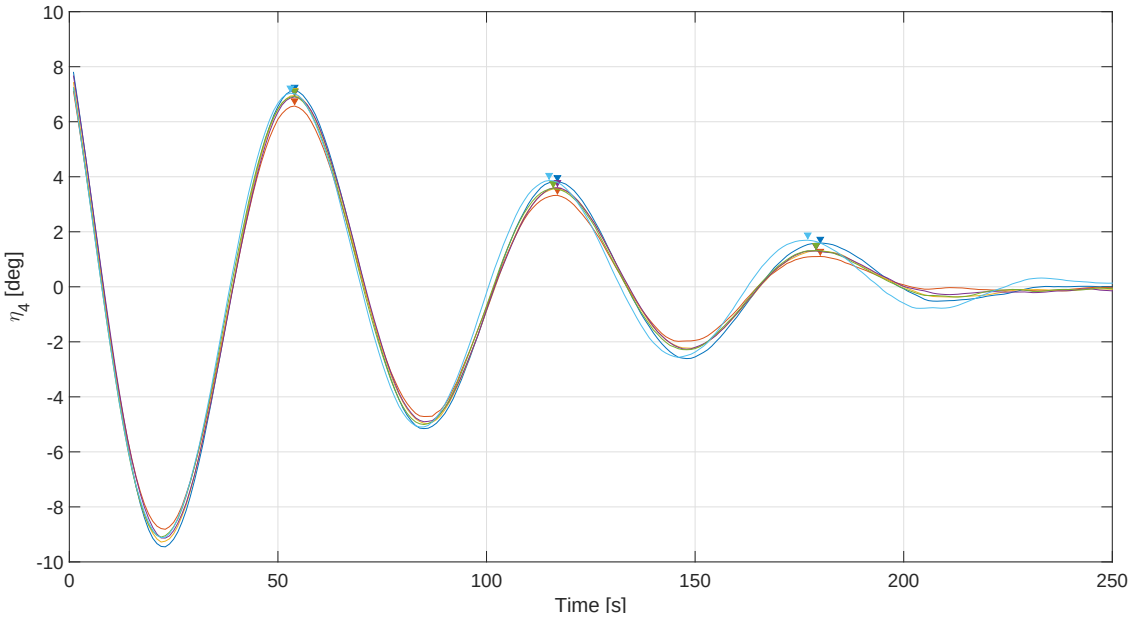

Figure 9.5: Measured response from decay tests with active thruster damping.

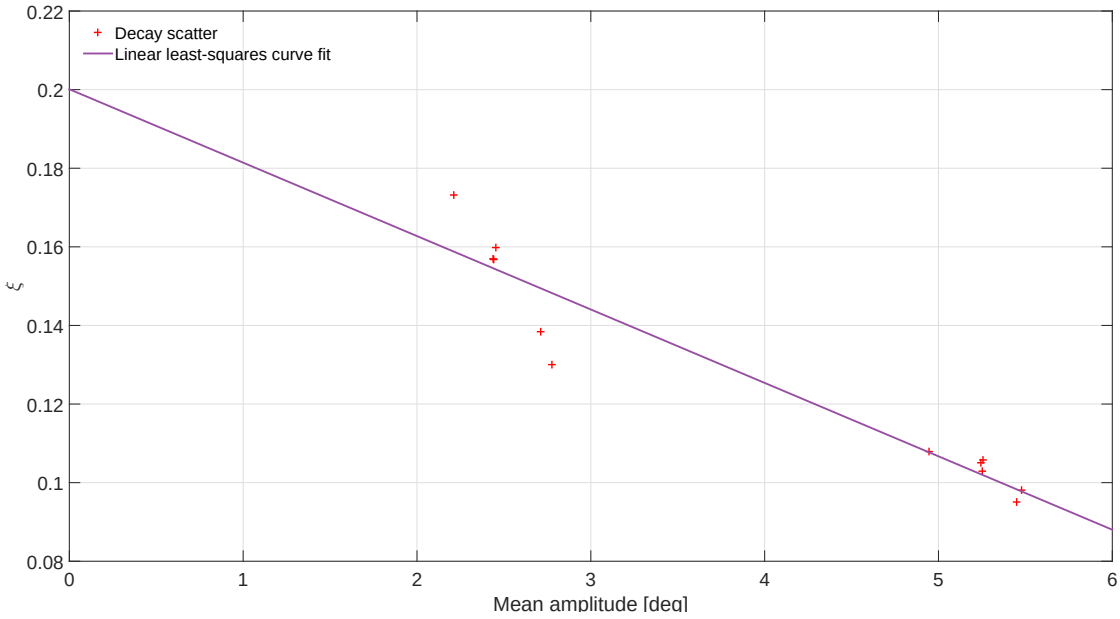

Figure 9.6: Measured damping from decay tests with active thruster damping.

9.1.4 Discussion

The results tabulated in Table 9.1 shows that the natural roll period is almost unchanged, the maximum difference is between with and without roll reduction which as a difference equal to 0.2 seconds in full-scale. From the results p1, i.e. the linear term, is the largest when active damping is used, however the equivalent non-linear term (p2) is negative which is difficult to discuss other than the damping is greater for lower roll amplitudes than higher.

Table 9.1: Results from experimental decay trials.

	$\mathbf{T_0}$	**p1**	**p2**	$\mathbf{R^2}$
NRD	2.4560	0.01731	0.005301	0.61
CSS	2.4578	0.03314	0.004405	0.63
ARD	2.5033	0.2001	-0.01868	0.91

A more intuitive approach to study the results is to represent the average of the two peaks the damping ratio is calculated from with the corresponding damping ratio. The results from the cases; no roll damping, constant shaft speed, and active damping are presented in the tables 9.2-9.4.

Table 9.2: Results from experimental decay trials, no roll damping.

Average peak	η_{4_a} [deg]	6.71	4.93	3.62	2.94	2.49	2.07
Damping ratio	ξ	0.0438	0.0560	0.0396	0.0249	0.0282	0.0316

Table 9.3: Results from experimental decay trials, with constant shaft speed.

Average peak	η_{4_a} [deg]	6.85	4.66	3.34	2.53	1.97	1.60
Damping ratio	ξ	0.064	0.057	0.048	0.039	0.041	0.021

Table 9.4: Results from experimental decay trials, with active roll damping.

Average peak	η_{4_a} [deg]	5.24	2.44
Damping ratio	ξ	0.103	0.160

The tables show that the constant shaft speed will contribute to some damping, but are not comparable with active roll reduction. To illustrate this further, the average of the damping

ratios are compared with NRD in Table 9.5.

Table 9.5: Average damping ratio comparison. The improvements are calculated with respect to NRD.

	Average damping ratio	**Improvement**
NRD	0.0374	
CSS	0.0451	20.6%
ARD	0.1309	250.0%

The results show that the damping ratio is increased with 250% when thrusters are actively used for roll reduction, which is a significant damping contribution, especially compared the constant shaft speed case. The magnitude of the damping contribution can be illustrated further by comparing the three test cases, Figure 9.7.

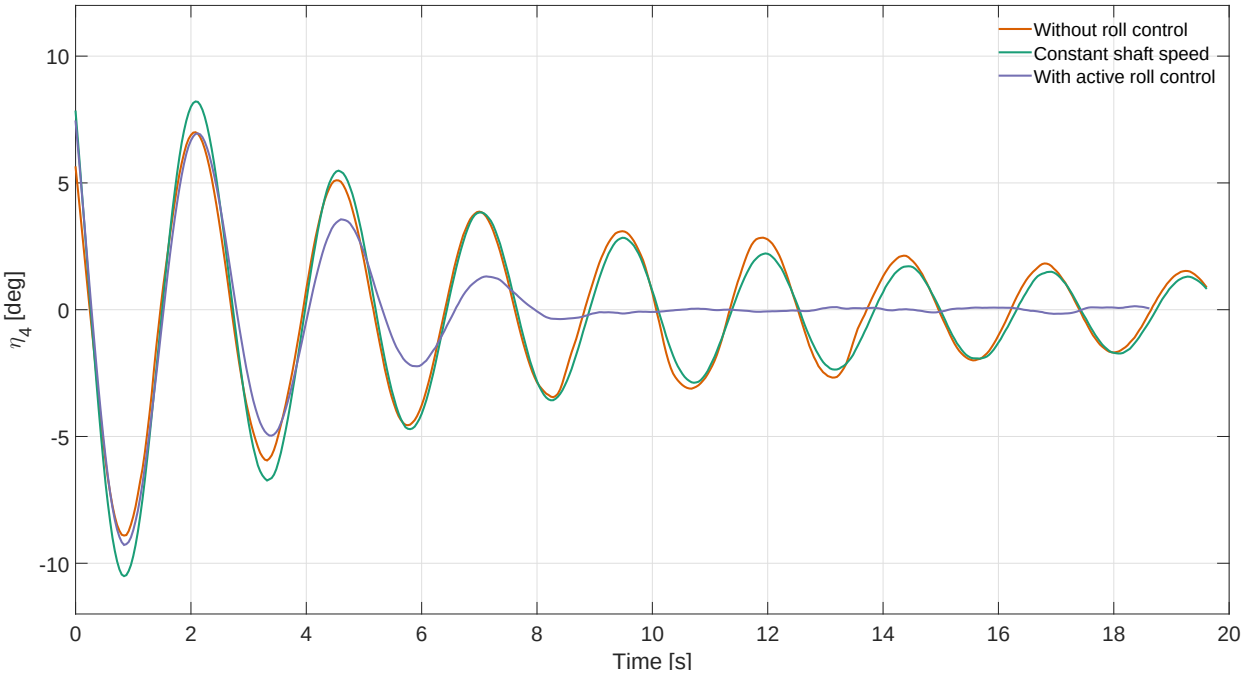

Figure 9.7: Decay comparison illustration.

9.2 Regular waves

The regular waves that were used in the experiments had wave heights 1.5 meters in full scale. The five regular waves had full-scale wave periods T_w=[8 10 11 11.9 14] s, and are illustrated in Appendix D.1. The post-processing of the regular waves was done by sampling the wave heights in the same range as the vessel responses were sampled. The average of the responses and the wave heights was calculated to find the RAO, Table 9.6 shows the average wave heights for the different regular wave periods. Moreover, the mean RAO results are presented in Table 9.7 with related error in Table 9.8.

Table 9.6: Calibrated regular waves (converted to full scale).

T_p [s]	8	10	11	11.9	14
ζ_a [m]	1.65	1.61	1.53	1.59	1.38

Table 9.7: Experimental RAO results.

$\mathbf{T}_p$	**NRD**	**CSS 100%**	**CSS 150%**	**ARD**
8	1.83°	-	-	1.44°
10	7.69°	6.87°	6.39°	4.48°
11	9.65°	8.97°	8.79°	5.71°
11.9	4.61°	4.47°	4.43°	3.25°
14	1.75°	-	-	0.63°

Table 9.8: Precision error estimation for RAO.

$\mathbf{T}_p$	**NRD**	**ARD**
10	-	0.56°
11	0.38°	0.62°
11.9	0.17°	0.27°

The results are illustrated graphically with a typical RAO plot with related error bars, Figure 9.8.

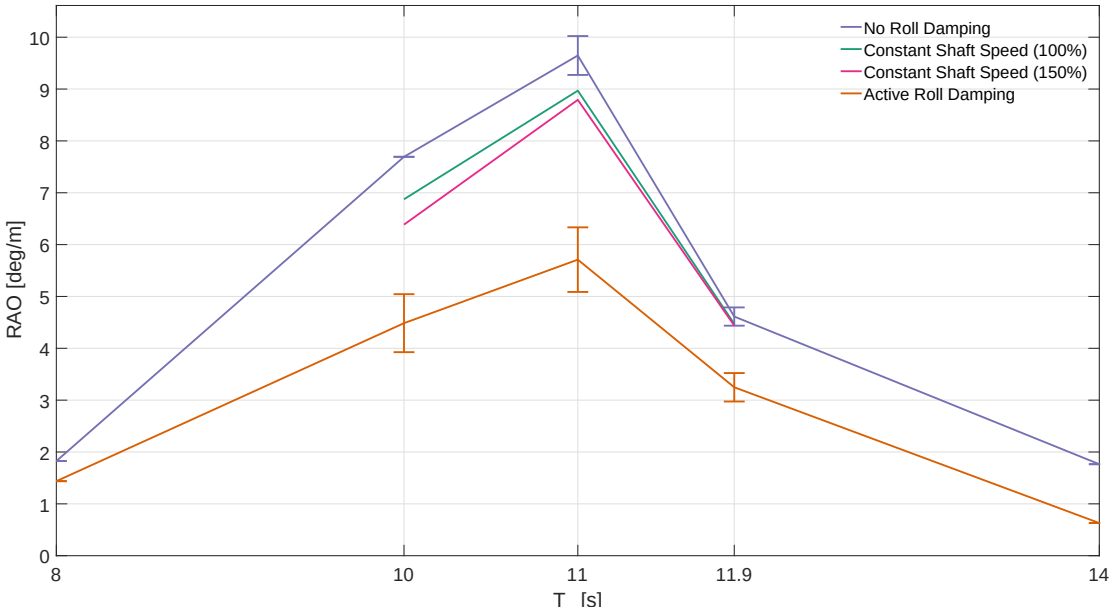

Figure 9.8: RAO without roll control, with constant shaft speed, and with roll control. Errorbars are plotted for the waves with sufficient repetitions.

From the results depicted in Table 9.7 and Figure 9.8 can the improvements be calculated. The improvements are presented in Table 9.9.

Table 9.9: Improvements RAO results with respect to NRD.

T_p	CSS 100%	CSS 150%	ARD
8	-	-	21.2 %
10	10.6%	17%	41.7 %
11	7.0%	8.9%	40.8%
11.9	3.1%	3.8%	29.6%
14	-	-	64.3%

The improvements show that the increasing the shaft speed, thus thrust, will increase the damping for smaller periods. However if the wave period is larger than 11 seconds will the difference between CSS 100% and CSS 150% decreases rapidly. The reason behind this effect is unclear, but the reader should note that there was not carried out multiple repetitions for CSS 150. The active roll damping system has some varying improvements; this could indicate that the trade-off between thrust variation and reaction should be different for different periods.

9.3 Irregular Waves

Three irregular waves were used each with significant wave height equal to 1.5 meters in full scale, and with peak periods T_p = [9.6 11.9 14] s. It was decided to use three wave spectrum to get several realistic operation scenarios. The time series of the irregular waves that were carried out represented 1 hour in full scale, which is 14 minutes in model scale. The usual procedure from MARINTEK is to sample peaks after 3 minutes; thus, the samples were carried out between 3-17 min. Because different roll stabilization manufacturers use different statistical properties, the decision was made to show the average (AVG), the standard deviation (STD), the root mean square, significant roll peak (η_{4_S}), and the maximum of the peaks (MAX). All of the tests were conducted without thrusters working and with active roll damping (ARD). Two of the cases were carried out with constant shaft speed (CSS). The active roll damping was also carried out in two different scenarios; ARD1 thrusters configured after the standard specifications, ARD2 with faster shaft speed rate, i.e 2 seconds faster than ARD1. ARD2 is supposed to represents faster thrusters, e.g. PM thrusters. However, due the fact that to some results were not properly stored, ARD1 was only carried out for peak period 11.9 seconds. Furthermore, the repetitions were carried out only a strictly sufficient amount of times for the sea state with full-scale peak period equal to 11.9 s. The remaining sea states were carried out two times for each thruster action case.

In the following, the roll responses from three irregular waves, illustrated with figures, will CSS and ARD be compared against NRD. Furthermore, statistical properties and the improvements are also tabulated in Table 9.10, 9.11 and 9.12.

Sea state Tp = 9.6 s

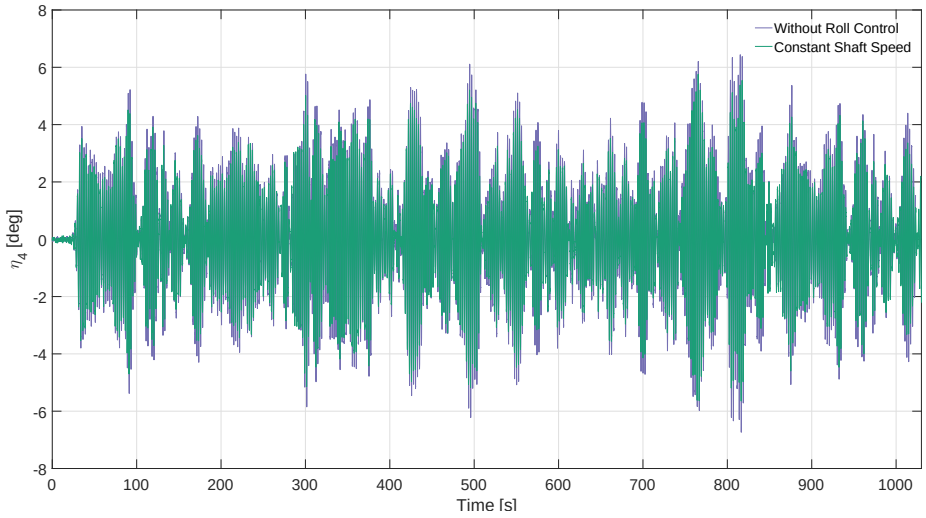

Figure 9.9: Comparison: CSS and NRD for irregular waves with peak period 9.6 s.

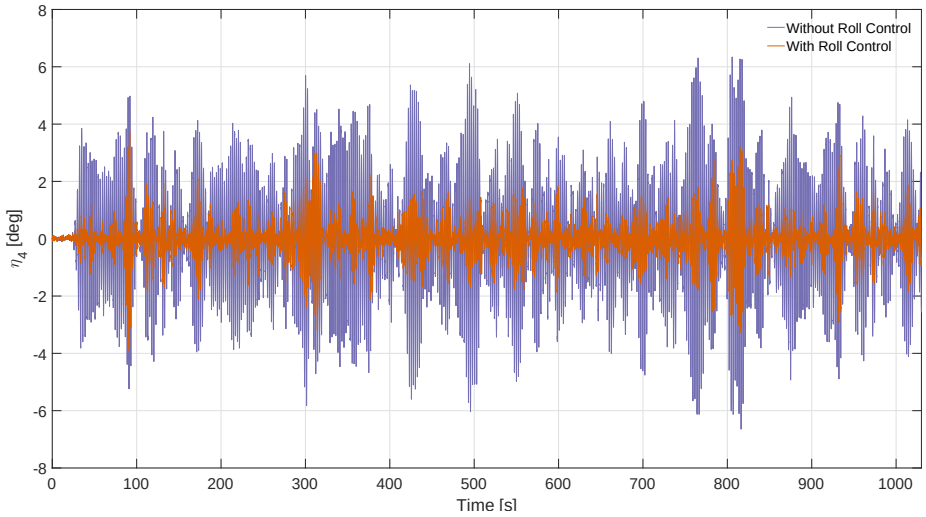

Figure 9.10: Comparison: ARD2 and NRD for irregular waves with peak period 9.6 s.

Table 9.10: Results from irregular waves with peak period equal to 9.6 seconds.

Statistical properties		Avg	STD	RMS	η_{4_S}	Max
NRD	[deg]	2.78	1.27	3.05	3.74	6.29
Constant RPS	[deg]	2.40	1.09	2.64	3.64	5.65
ARD 2	deg	0.91	0.62	1.10	1.85	3.42
Improvements		avg	std	RMS	η_{4_S}	Max
CSS	[%]	13.7	14.2	13.4	13.6	10.2
ARD 2	[%]	67.3	51.2	63.9	56.0	45.6

Sea state Tp = 11.9 s

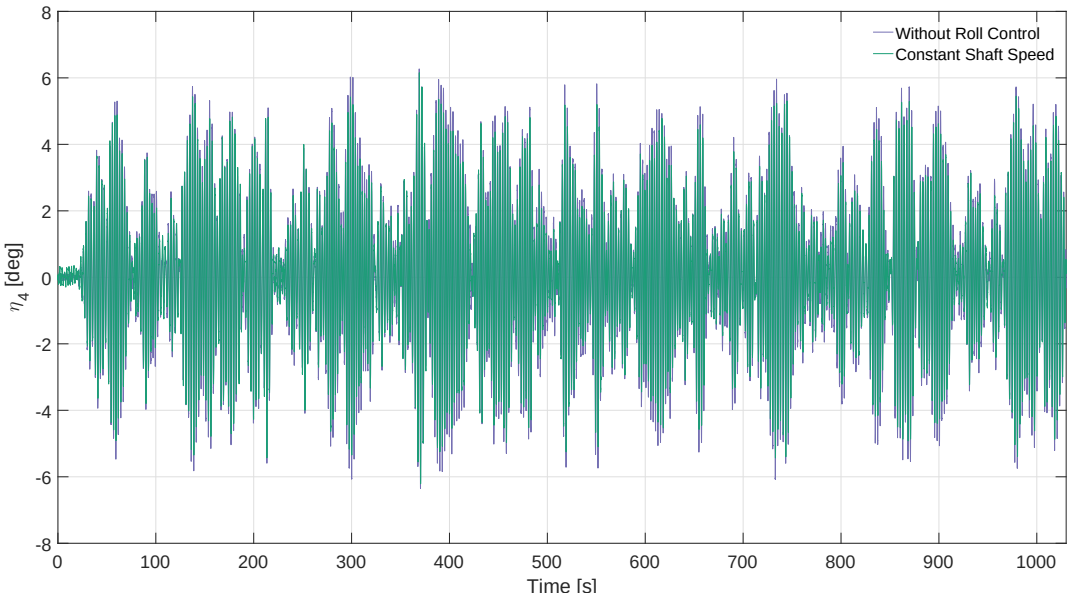

Figure 9.11: Comparison: CSS and NRD for irregular waves with peak period 11.9 s.

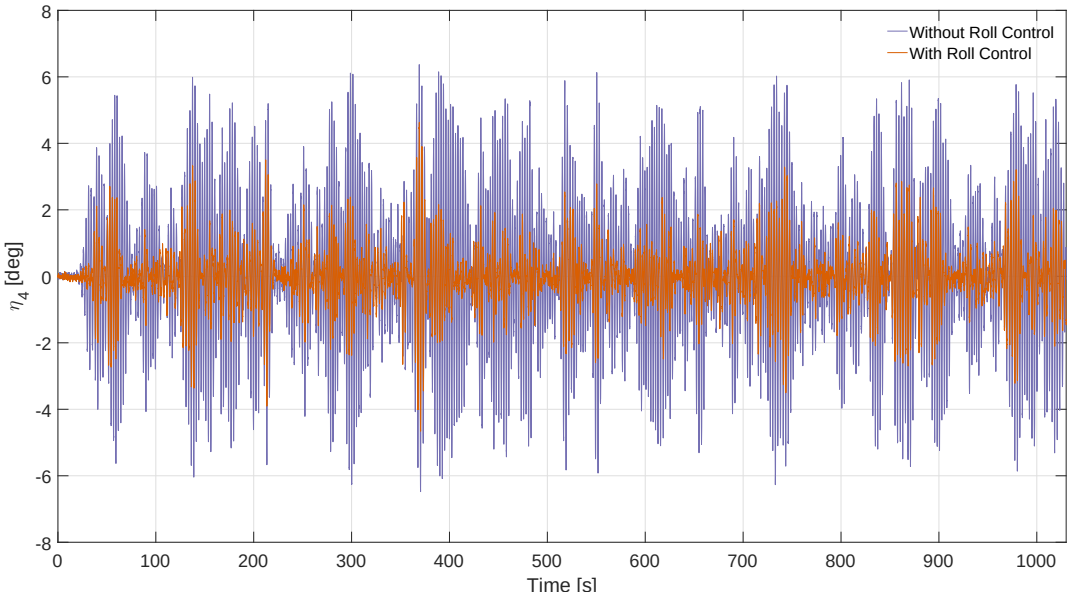

Figure 9.12: Comparison: ARD1 and NRD for irregular waves with peak period 11.9 s.

Table 9.11: Results from irregular waves with peak period equal to 11.9 seconds.

Statistical properties		AVG	STD	RMS	η_{4_S}	Max
NRD	[deg]	2.99	1.47	3.33	4.72	6.33
CSS	[deg]	2.63	1.32	2.95	4.18	6.05
ARD 1	[deg]	1.09	0.77	1.36	2.01	4.78
ARD 2	[deg]	0.94	0.72	1.20	1.78	4.22
Improvements		AVG	STD	RMS	η_{4_S}	Max
CSS	[%]	12.0	10.2	11.4	11.5	4.4
ARD 1	[%]	63.5	47.6	59.2	57.6	24.4
ARD 2	[%]	68.6	51.0	64.0	62.2	33.3
Precision error		AVG	STD	RMS	η_{4_S}	Max
NRD	[deg]	0.04	0.05	0.05	0.09	0.15
ARD 2	[deg]	0.15	0.06	0.15	0.21	0.50

Sea state Tp = 14 s

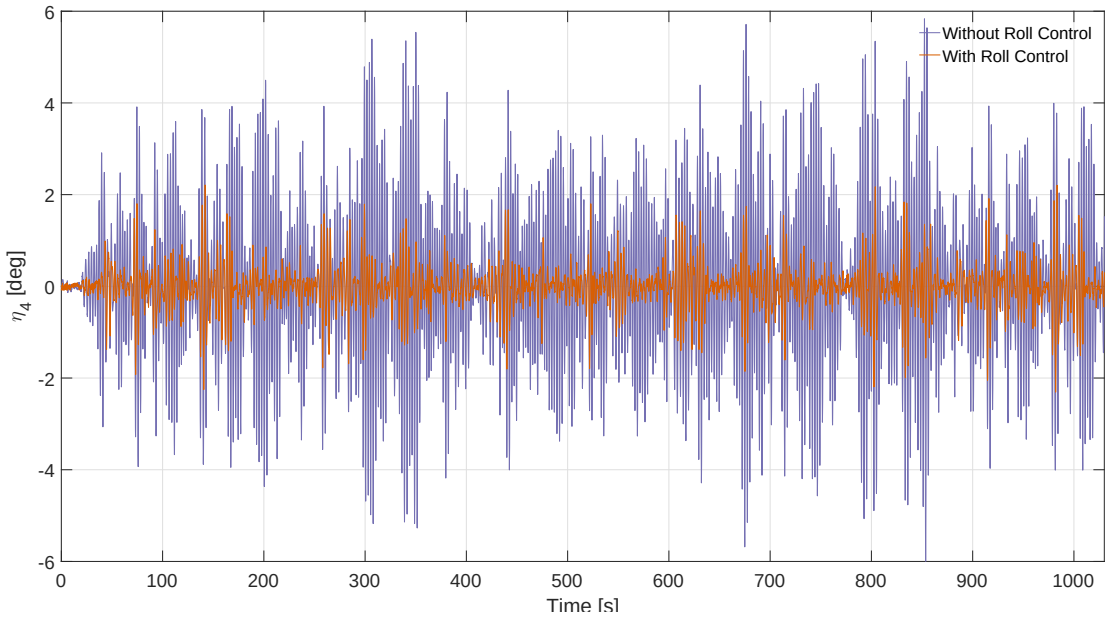

Figure 9.13: Comparison: ARD2 and NRD for irregular waves with peak period 14 s.

Table 9.12: Results from irregular waves with peak period equal to 14 seconds.

Statistical properties		AVG	STD	RMS	η_{4_S}	Max
NRD	[deg]	2.35	1.21	2.63	3.74	5.86
ARD 2	[deg]	0.76	0.49	0.92	1.35	2.60
Improvements		AVG	STD	RMS	η_{4_S}	Max
ARD 2	[%]	67.6	59.0	65.2	63.8	55.6

9.3.1 Discussion of statistical roll properties

From the results depicted in the figures and tables in the previous section, it is obvious that the roll damping system is efficient during moderate sea-states. In general for the three sea states the improvements are in the area 50-70%. In the introduction it was stated that according to Jürgens and Palm (2009) cycloidal propulsion units damped significant roll motions in the order of 64% for sea states with significant wave height equal to 1.5 meters. The improvements in significant roll motion for the three different irregular waves presented, which have the same significant wave heights as Jürgens and Palm (2009), are in the order 56.0-63.8%. Thus, are the roll damping achieved by using conventional thrusters comparable with cycloidal propulsion units for moderate sea states.

9.3.2 Probability of non-exceedance

The statistical roll properties from the irregular waves, can be used to calculate the probability of non-exceedance (PNE), see Section 6.3, using the roll criteria for helicopter landing on ships (Helideck Certification Agency, 2016), i.e. lower than 2°and 3°, and Weibull distributions. The irregular wave with peak 11.9 seconds was used to illustrate the PNE because it had the most repetitions and this sea state experienced the largest roll motions. The results are presented in 9.13 and are shown graphically by PDFs in Figure 9.14.

Table 9.13: Probability of non-exceedance for irregular wave Tp 11.88 s.

	NRD	**CSS**	**ARD1**	**ARD2**
$P(\eta_4 \leq 2^o)$	28.5%	35.8%	87.6%	91.4%
$P(\eta_4 \leq 3^o)$	54.4%	64.0%	97.8%	98.6%

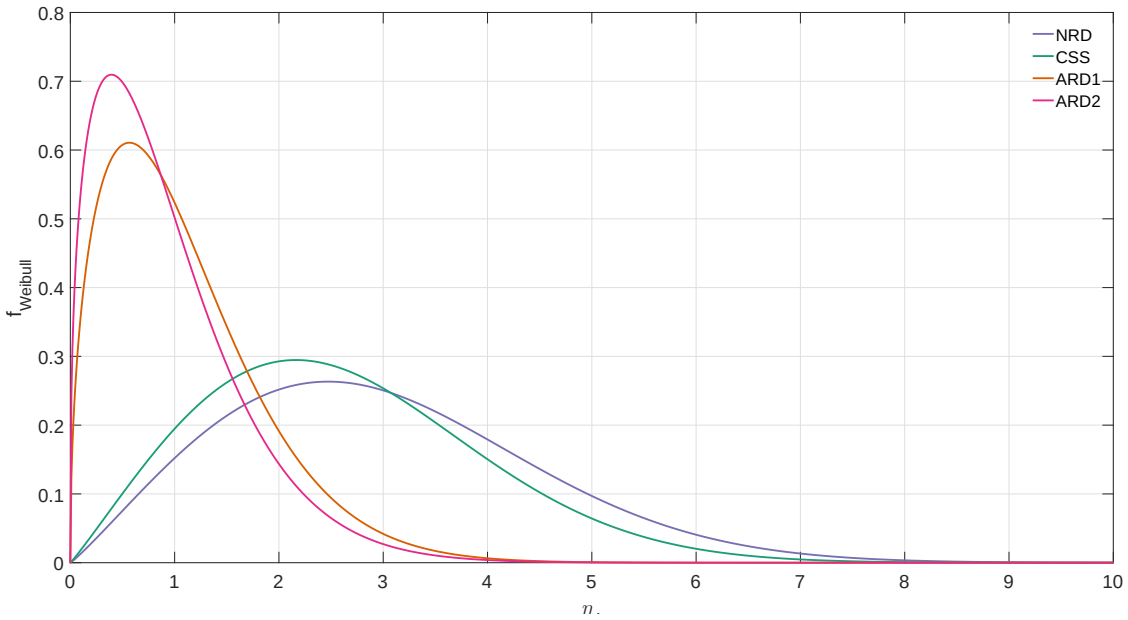

Figure 9.14: Weibull probability density functions for roll peaks with irregular wave Tp 11.9 s and significant wave height 1.5 meter.

Table 9.13 and Figure 9.14 shows that 98% of the roll peaks are below the criteria when active roll reduction is active, this stands in contrast to the case when no roll reduction is used, i.e. 54%.

9.3.3 Prediction of power usage

In order to use such a system, it is necessary to calculate the power used to damp the system. The power is calculated using the relation between torque (Q_a), shaft sped (n), and the mechanical loss η_M this is expressed as

$$P_a = 2\pi n Q_a \eta_M(n, Q_a). \tag{9.1}$$

The mechanical loss in model scale is defined using an empirical formula provided by Luca Savio at MARINTEK:

$$\begin{aligned}\eta_{M_M}(n, Q_a) = &-0.015017 - 0.001264 \cdot n + 0.962580 \cdot Q_a \\ &+ 0.000026 \cdot n^2 + 0.002791 M^2 + 0.000079 \cdot n \cdot M.\end{aligned} \tag{9.2}$$

The mechanical loss estimation with respect to shaft speed and torque is plotted in Figure 9.15. Moreover, the mechanical loss is scaled to full scale with the following relation $\eta_{M_F} = \eta_{M_M}/0.95$. It is scaled by dividing by 0.95 since this is a typical mechanical loss factor in full scale.

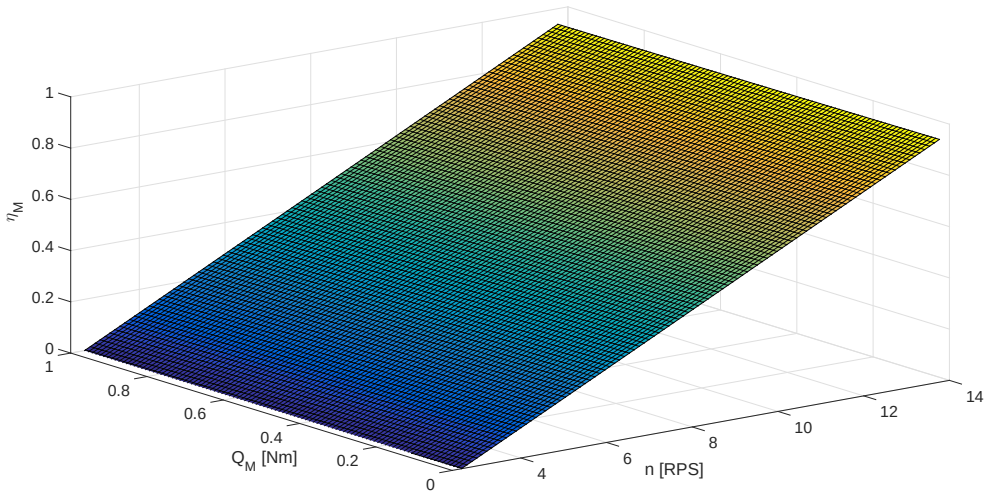

Figure 9.15: Mechanical loss estimation with respect to shaft speed and motor torque.

The fuel consumption is calculated by integrating the effect over time:

$$P[kWh] = \int_0^T P_a dt. \tag{9.3}$$

There are mainly two power estimation parameters that are of the importance: the maximum effect and the mean effect. The maximum effect is needed to establish whether the full-scale thrusters can produce the requested power, and the mean effect is used to calculate the fuel consumption. The results from the model experiments and the scaled to full scale results are presented in Table 9.14.

Table 9.14: Results from power estimation from model scale and scaled to full scale using Froude scaling.

	Model-scale		**Full-scale**	
Max power Azipull thrusters	$P_{M_A}^{max}$ [W]	66.83	$P_{F_A}^{max}$ [kW]	1897
Max power Bow thrusters	$P_{M_B}^{max}$ [W]	14.02	$P_{F_B}^{max}$ [kW]	398
Mean effect Azipull thrusters	$P_{M_A}^{mean}$ [W]	22.20	$P_{F_A}^{mean}$ [kW]	630
Mean power Bow thrusters	$P_{M_B}^{mean}$ [W]	4.11	$P_{F_B}^{mean}$ [kW]	116

The motor power for the Rolls Royce Azipull thrusters has according to the technical specification 2090 kW for each thruster, and the bow thrusters have 970 kW each. By comparing this with the results from Table 9.14 is it apparent that the conclusion must be that all the thrusters have sufficient power.

9.3.4 Fuel consumption

To discuss the fuel consumption, a comparison is drawn between a helicopter and the propulsion system. It might be more economically beneficial to turn the system on during the helicopter landing, than for the helicopter to wait until the waves calm. The case helicopter is of the type Sikorsky S-92 used by Norwegian helicopter operators Norsk Helikopterservice (NHS). The power of the S-92 is 2043 kW, in this case, it is assumed that the aircraft operates at 80% MCR, i.e. 1840 kW. The mean power used for the anti-roll system is 746 kW.

In this scenario, the vessel is equipped Rolls Royce B32:40L6P, which has a specific fuel consumption equal to 184 g/kWh, thus will the fuel conception per hour be 140 kg/h. According to Technical Manager Roger Aure at NHS (personal communication, June 3, 2016) does their S-92 have an average consumption equal to 590 kg/h. Thus, might fuel be saved using the roll damping system if waiting is needed.

9.4 Combination: Active thruster damping working with passive anti roll tanks

Another experimental trial that was carried out were trials using anti-roll tanks. The main purpose of doing this was to change the lower GM, thus increasing the natural roll period. The goal was to see if the thrusters would perform better on vessels with higher natural roll periods, since the thrusters will have more time to produce thrust. The weight of 23 kg was removed from the vessel and replaced with water in an anti-roll tank. This increased the natural roll period to 13.5 seconds, however, this also increased the damping of the model to such a great extent, that the response from regular waves became so small with active thrusters, that if was difficult to study the results. Thus, it was decided to study the effect with both the passive anti-roll tanks and the active roll damping using thrusters. Figure 9.16 presents the decay test, from the illustration the reader can see that it is not possible to calculate the increased damping ratio with the active control system, because the system is fully damped after only one roll peak. Figure 9.17 represents the irregular wave with peak 14 s with anti-roll tank and with anti-roll tank and the active thruster roll damping system. The results and improvements are presented in Table 9.15.

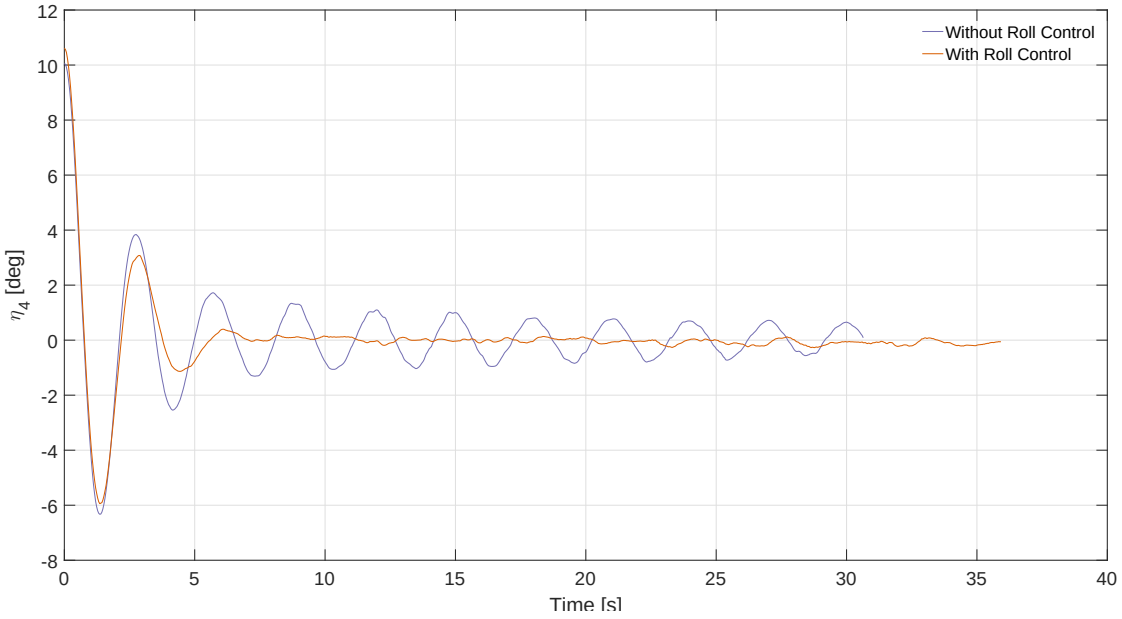

Figure 9.16: Decay with passive anti roll tanks.

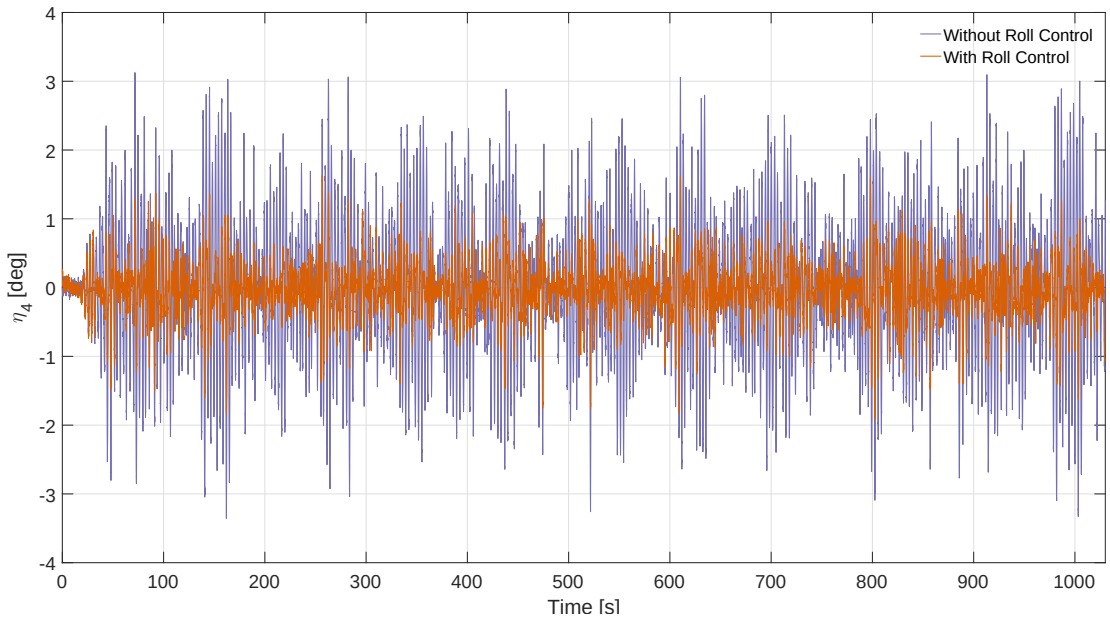

Figure 9.17: Comparison: ARD2 and NRD for irregular waves with peak period 14 s equipped with a anti-roll tank.

Table 9.15: Results from irregular waves with peak period equal to 14 seconds.

Statistical properties		AVG	STD	RMS	η_{4_S}	Max
No roll reduction	deg	2.35	1.21	2.63	3.74	5.86
Anti-roll tank	deg	1.29	0.63	1.43	2.32	2.96
Anti-roll tank & ARD 2	deg	0.56	0.27	0.94	0.62	1.59
Improvements		AVG	STD	RMS	η_{4_S}	Max
Anti-roll tank	%	38.3	37.8	38.2	38.0	41.9
Anti-roll tank & ARD 2	%	76.2	71.6	75.2	74.9	68.2

Table 9.15 shows that the damping is increased from around 38% when only-anti roll tanks are measured to 74% when the thrusters work as well as the passive anti-roll tank.

9.5 Roll center estimation

It is of vital importance to have established the vertical roll of center (COR), due to the fact that it is necessary for the calculation of the incoming water velocity and the thruster's momentum arm. The term is often set to the center of gravity (COG). However, it is possible to estimate the roll center using two velocities on the body, since the roll center lies at the intersection be-

tween those two lines, Fernandes et al. (2015). Unfortunately, the roll rate of the vessel was only measured during the experiments, thus was it difficult to estimate the roll center experimentally. Fernandes et al. (2016) introduces away to estimate the location of the vertical center of roll using heave and roll parameters:

$$\begin{aligned} COR_T &= COG + \frac{V_z(t)}{\omega_4(t)} \\ V_z(t) &= -\eta_3 \omega_3 \sin(\omega_t t + \phi_3) \end{aligned} \tag{9.4}$$

Using this approach, the results were not comparable with the results from Fernandes et al. (2016), and therefore it was decided to continue with a different approach. Since the sway is measured, the sway velocity can be estimated by derivation in MATLAB. Therefore, the two points can be used to find the center of roll even though the estimated sway velocity ($\hat{\dot{\eta}}_2$) might contain some discrepancy. One velocity measurement is taken from the center of gravity(COG), which is where the measurements are taken from, and one point is at the keel, see Figure 9.18 and Equation (9.5).

$$y_1 = \hat{\dot{\eta}}_2, \tag{9.5a}$$

$$y_2 = \hat{\dot{\eta}}_2 - COG \cdot \dot{\eta}_4. \tag{9.5b}$$

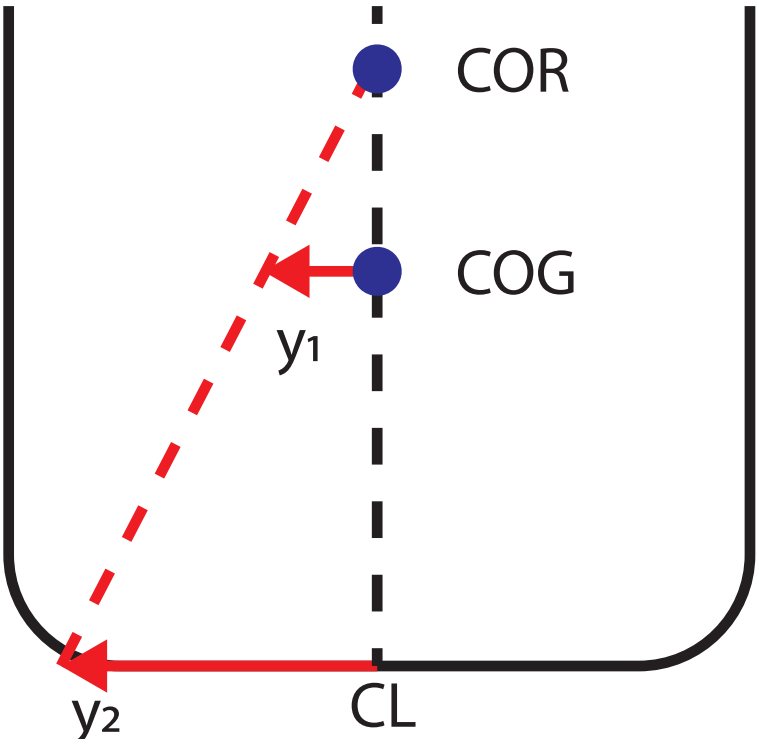

Figure 9.18: Center of roll estimation.

The vertical center of roll can be estimated by finding the intersection between the centerline (CL) and the sway velocities y_1 and y_2:

$$COR = \frac{y_2 \cdot COG}{y_2 - y_1} = \frac{\dot{\eta}_4 \cdot COG - \hat{\dot{\eta}}_2}{\dot{\eta}_4}. \tag{9.6}$$

From Equation (9.6), the center of roll will go towards $\pm\infty$ when the roll rate goes towards zero, which is the same behavior found in (Fernandes et al., 2016, Fig. 9). The roll rate and the estimated sway rate are presented in Figure 9.19, and the center of roll is depicted for the experimental roll decay in Figure 9.20.

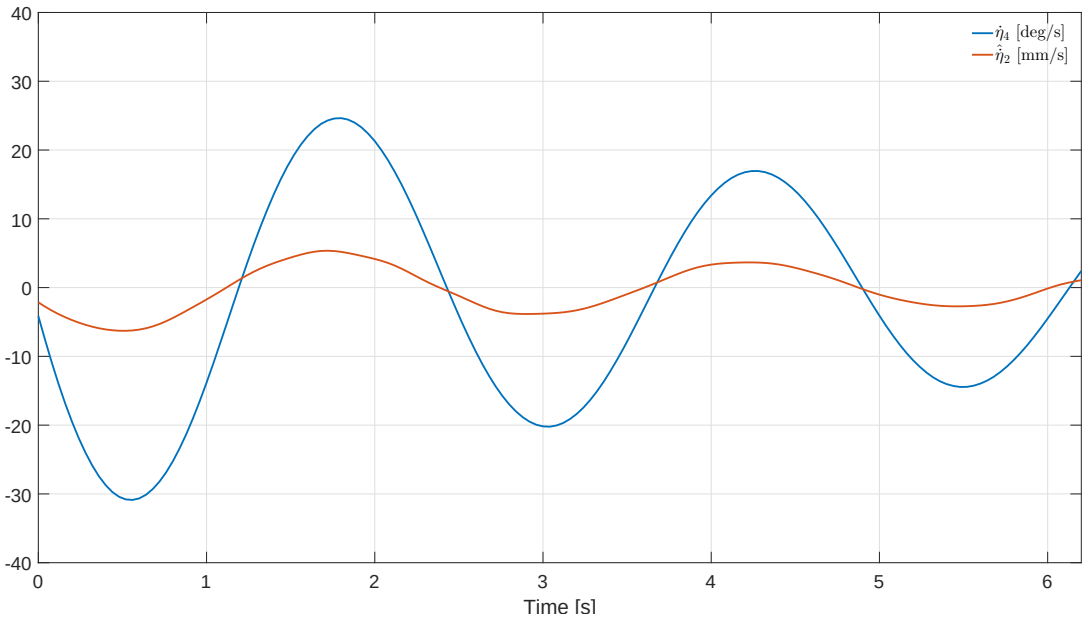

Figure 9.19: Roll rate and estimated sway rate during a decay test.

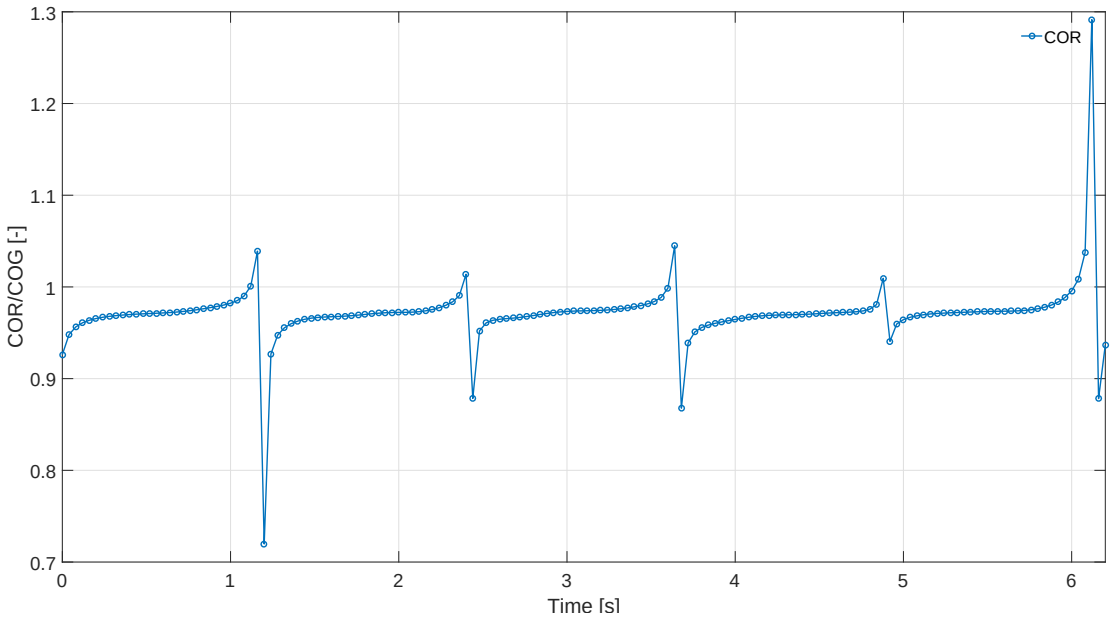

Figure 9.20: Non-dimensional center of roll found experimentally.

Figure 9.20 clearly shows that for the majority of time, the center of roll lies slightly below the center of gravity. This can be illustrated further by studying the regime of importance, i.e. where the majority COR occur. The results are presented in Figure 9.21.

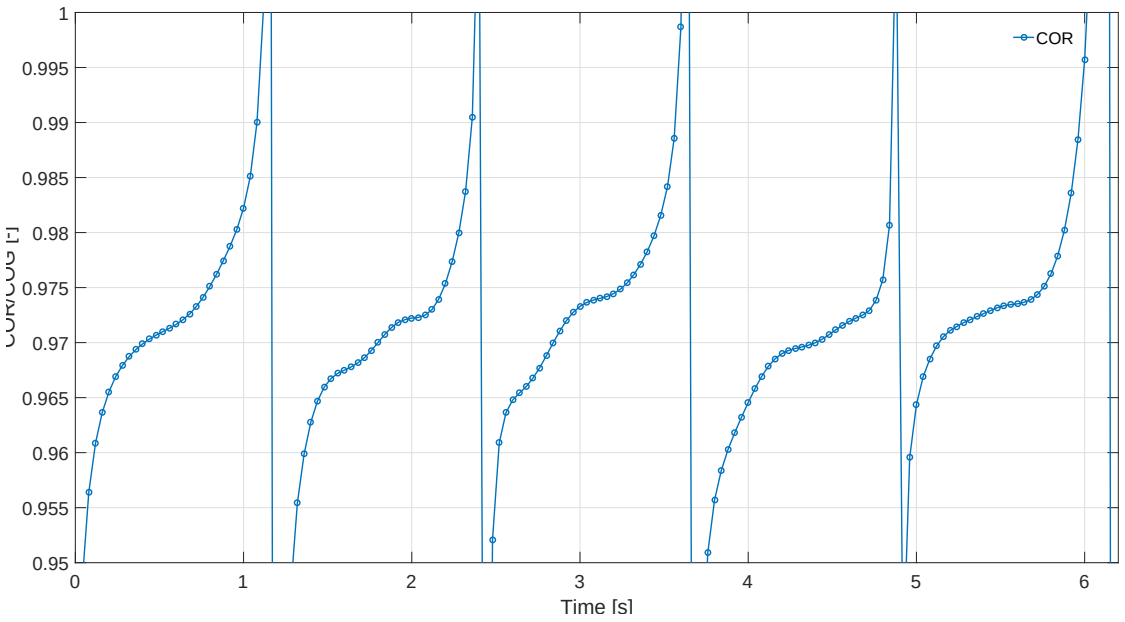

Figure 9.21: Non-dimensional center of roll found experimentally 2.

The average from the relationship COR/COG was found to be 0.97, i.e. the average roll center is placed 3% below the center of gravity.

9.6 Open water comparison

Prior to the experimental trials, open water tests were carried out see Section 7.2. Open water tests are steady state tests in which the velocity and the shaft speed are kept constant. The roll motions are dynamic, thus other effects will take place. The first dynamic effect, which also is difficult to study, is the influence in the wake that the propellers are creating. When the vessel is oscillating, the propellers will operate in their own wake. Secondly, the hull-propeller interaction could also change the thrust. Lastly, ventilation could take place during large roll angles.

Before the roll experiments could be compared with the open water characteristics, it was necessary to adjust the force transducers with respect to the mass and inertia forces from the engines that were mounted on top of the propellers, since they will impact the sampled forces. Figure 9.22 illustrates the force measurements for the regular wave 11 s when thrusters are not working.

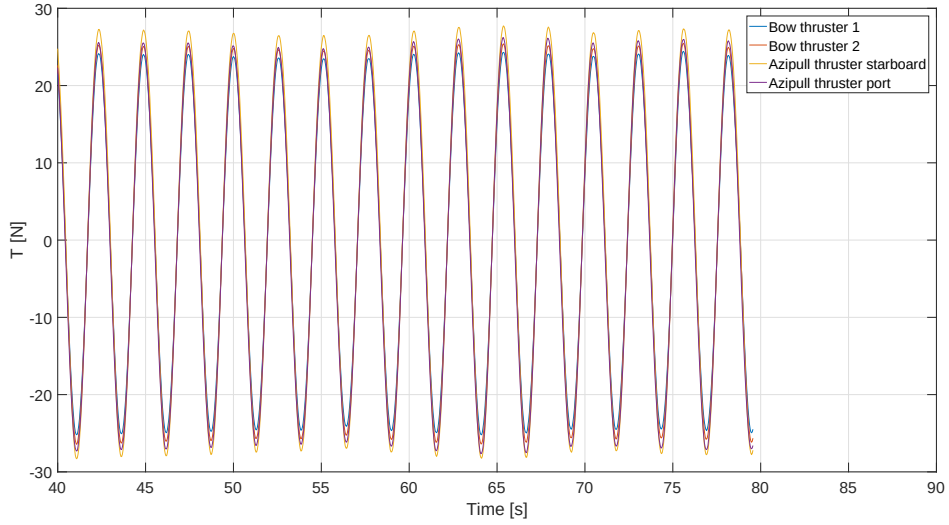

Figure 9.22: Thruster force measurements when thrusters are not active.

This was adjusted for the roll motion and the acceleration measured on top of the thrusters as:

$$T_{correction} = a\ddot{\eta}_4 + b\sin(\eta_4) +, \tag{9.7}$$

where a and b are tuning parameters. The parameters are different for all the four thrusters, and are found using the curve fitting toolbox in MATLAB, the results are found in Table 9.16.

Table 9.16: Thrust correction factors.

Thruster	**a**	**b**
Bow 1	16.6	38
Bow 2	17.2	41
Azipull starboard	20.5	24.9
Azipull port	14.3	74.2

Furthermore, the thrust and acceleration measurements were filtered using a low pass filter, where all frequencies above 2 Hz was filtered out using the Nyquist frequency in order to avoid aliasing:

$$f_N = \frac{f_s}{2}, \tag{9.8}$$

where f_s represents the sampling frequency (200 Hz).

Another problem that arises is that the roll motion was sampled with a different sampling frequency than the roll rate, acceleration, and force transducers. Thus, there are two possible approaches to the problem; extrapolate the roll motion, or down-sample the other parameters with the same sampling frequency as the roll motion. Both of these methods are presented below for one roll cycle and compared to the open water trials found in Section 7.2.

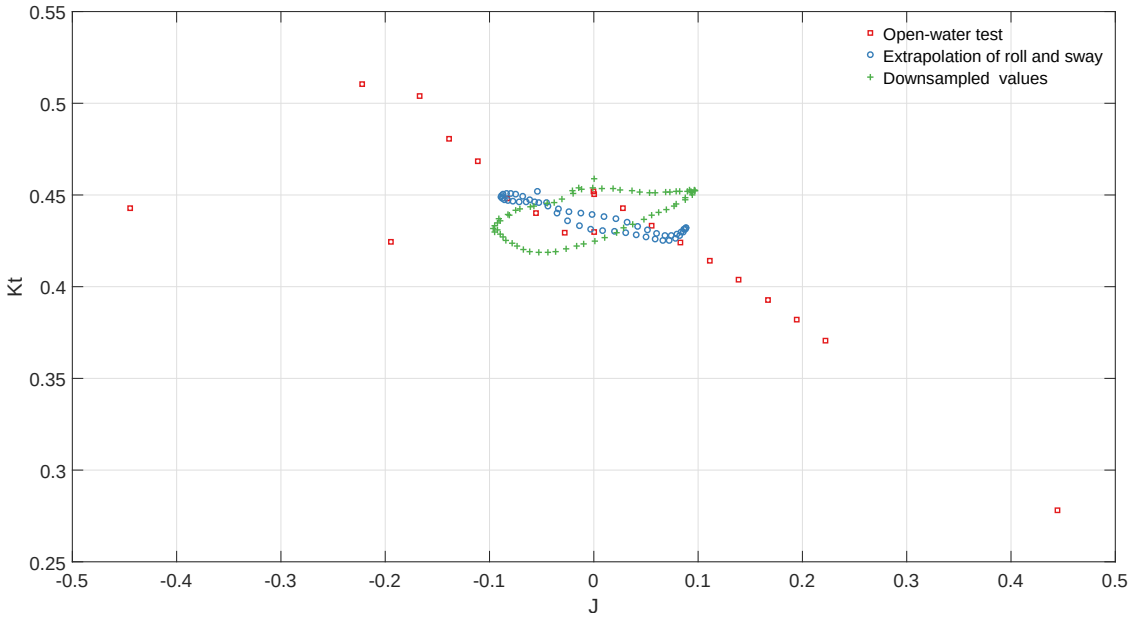

Figure 9.23: Comparison with open water test for Azipull thrusters.

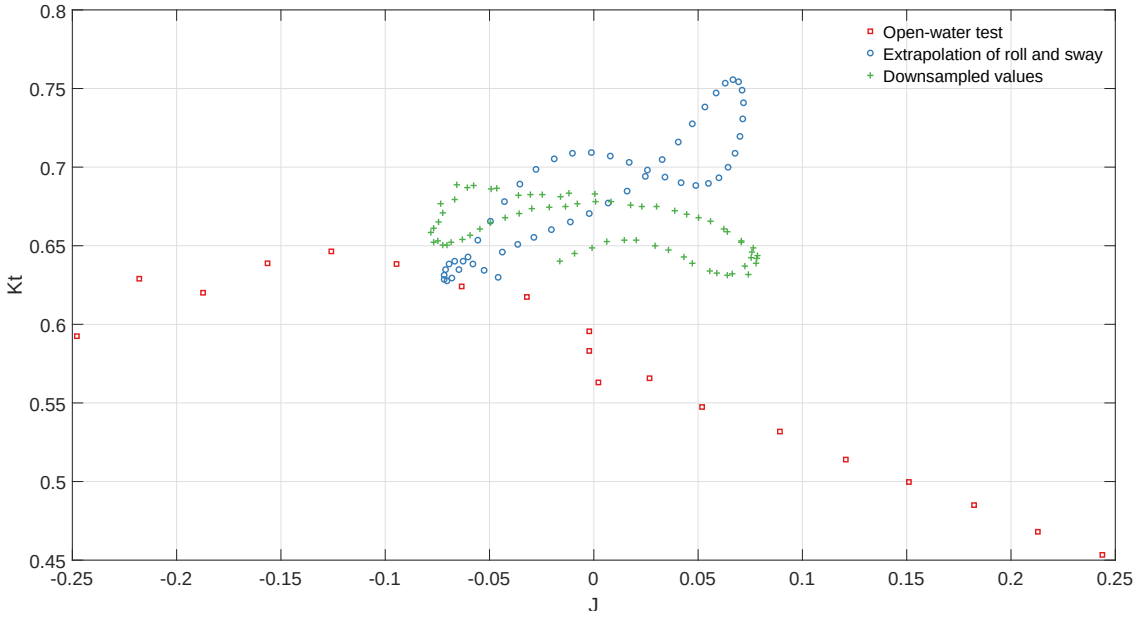

Figure 9.24: Comparison with open water test for bow thrusters.

Both figures 9.23 and 9.24 shows discrepancies compared to the measured steady state open water tests represented in red. This discrepancy yields for both suggested sampling methods. The bow thrusters the difference is of magnitude 10% higher than what was measured during the open water tests. The largest discrepancy is the circular like behavior the thrust coefficients are depicting.This could be due to the dynamic effect mentioned. In order to get a more realistic open water test should the tests have been carried out with oscillations instead of fixed speeds. It is a great deal of uncertainty behind this guess, thus, should new experiments be performed in order to study this phenomenon closer.

Part III

Simulation Results

Chapter 10: Hydrodynamic coefficients

Past simulations were carried out with the hydrodynamic coefficients calculated from VERES. To achieve a correct simulation model, new values should be calculated. From the inclination test GM and the weight of the vessel was found. Thus, the restoring moment can be found using:

$$C_{44} = \rho g \nabla \mathrm{GM}_T. \tag{10.1}$$

Moreover, the radius of gyration (r_{44}) can be estimated using the relationship between the natural roll frequency (ω_{0_4}), the restoring moment and added mass. Using the added mass coefficient indicates that the VERES added mass are correctly calculated at the natural frequency.

$$\omega_{0_4} = \sqrt{\frac{C_{44}}{I_{44} + A_{44}}}, \tag{10.2}$$

where $I_{44} = M\, r_{44}^2$. From the decay tests, Section 9.1, the natural roll frequency was calculated to be 2.57 rad/s. The calculated restoring moment, the radius og gyration and mass moment of inertia are tabulated in Table 10.1.

Table 10.1: Calculated hydrodynamic coefficients from experiments.

	Symbol	**Unit**	**Value**
Mass	M	[kg]	1428.8
Transverse metacentric height	GM_T	[m]	0.134
Restoring moment	C_{44}	[Nm/rad]	1878
Added mass	A_{44}	[Nm(s/rad)^2]	80
Natural roll frequency	ω_{0_4}	[rad/s]	2.57
Radius of gyration	r_{44}	[m]	0.45
Mass moment of inertia	I_{44}	[Nm(s/rad)^2]	206

10.1 Vertical roll center

Section 9.5 described the behavior of the estimated center of roll. The results clearly depicted rapid signal changes around roll rate equal to zero. This is not suited for simulation purposes. This necessitates fixing the vertical center of roll to a constant value, and COR are set to be equal to COG for the simulations.

10.2 Open water representation

As mentioned earlier, the open water tests must be represented with curve fitting due to the non-continuous behavior not suited for simulation purposes. From Section 4.3.1 it found that Häusler et al. (2013, 2015) L-method was a suitable model representation of the Wageningen example propeller. The L-method is depicted for the Azipull and bow thrusters below.

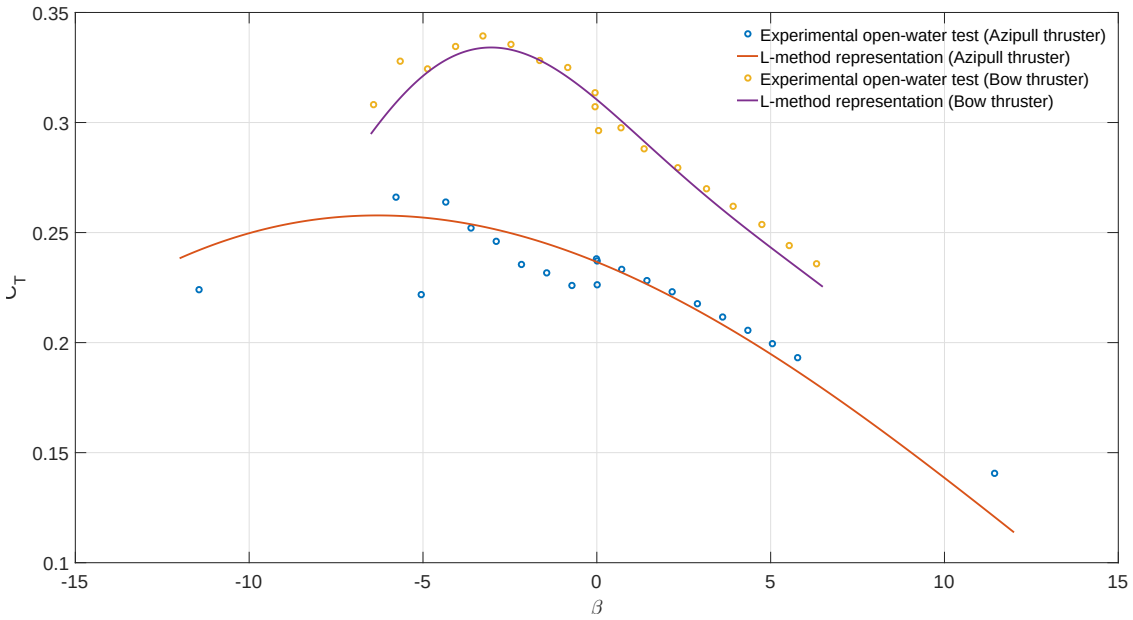

Figure 10.1: L-method representation of the open water test.

Figure 10.1 shows a good fit for the bow thrusters, however, the Azipull show some discrepancy. Since there are considerable uncertainty regarding if standard open water tests can be used, see Section 9.6 for further discussion, are these fitting curves acceptable for the simulations.

10.3 Nonlinear roll damping term

Faltinsen (1990) nonlinear roll damping linearization leads to equal damping ratio for every roll angle, which is not realistic. Since the simulation environment should be as close to reality as possible, it is suggested to introduce other methods. The importance of correct nonlinear damping term estimation is discussed in de Oliveira and Fernandes (2014), where several methods are introduced. Different methods were carried out to represent the damping ratios. The result was the second order damping moment function that was tuned to fit the experimental results. This was tuned by changing the nonlinear damping term (B^4_{NL}) until the linear regression line for the roll damping ratios was similar for both experimental and simulated decay tests. The total damping contribution in roll is illustrated as:

$$\text{Damping} = B_{Lin}(\omega_w) + B^4_{NL}\dot{\eta}_4|\dot{\eta}_4|. \tag{10.3}$$

It was found that $B^4_{NL} = 210 Nms^2/rad^2$ was the optimal nonlinear term. The comparison between experiments and simulations with adjusted nonlinear damping component are depicted with decay tests on the following page.

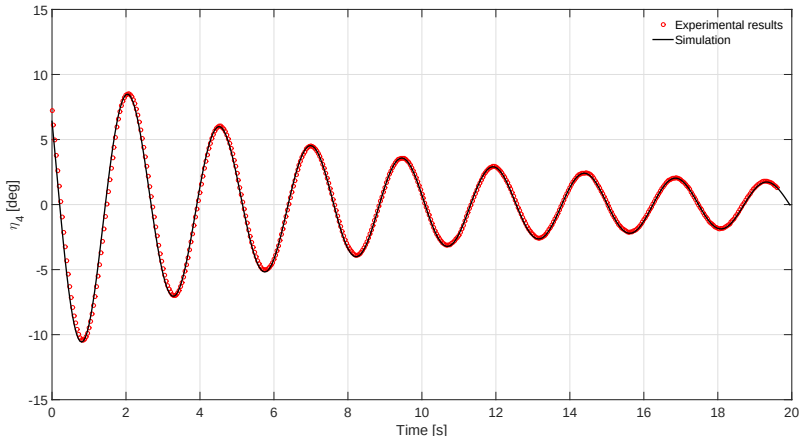

Figure 10.2: Comparison experimental vs simulation roll decay without roll control.

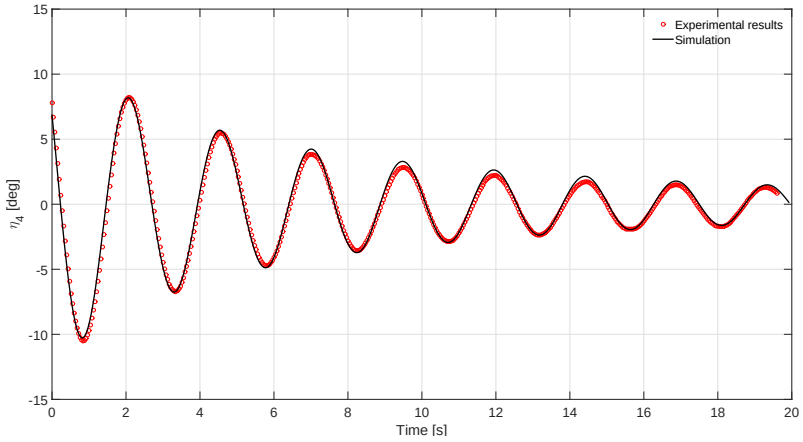

Figure 10.3: Comparison experimental vs simulation roll decay with constant shaft speed.

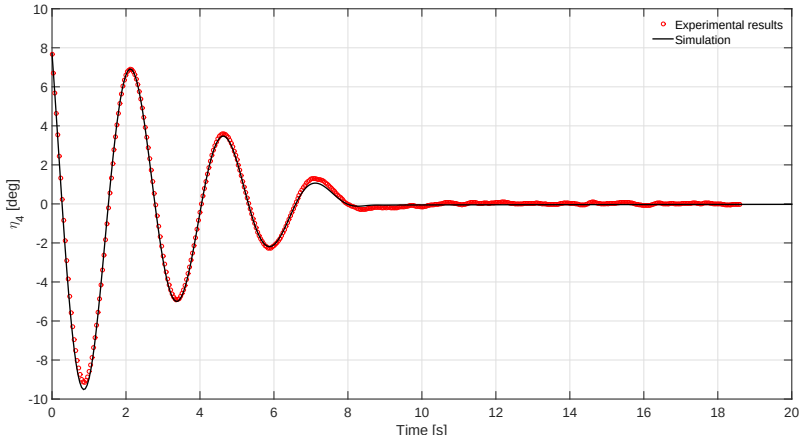

Figure 10.4: Comparison experimental vs simulation roll decay with active roll control.

Both the in case with and the case without roll control, great comparability was shown. However, there is some discrepancy between the numerical and experimental results for constant shaft speed. There are many possible causes for this discrepancy. Most likely it is due to the discrepancy shown in open water tests presented in Section 9.6.

10.3.1 Nonlinear sway damping term

This spring force was implemented in the SIMULINK model. Since the equivalent linear sway damping term is not known, several sway decay tests were simulated for different equivalent sway damping terms (B_2^{EQ}). The nonlinear equivalent damping term equal to 0.015 gave the best fit. The results from this sway decay test are illustrated in Figure 10.5.

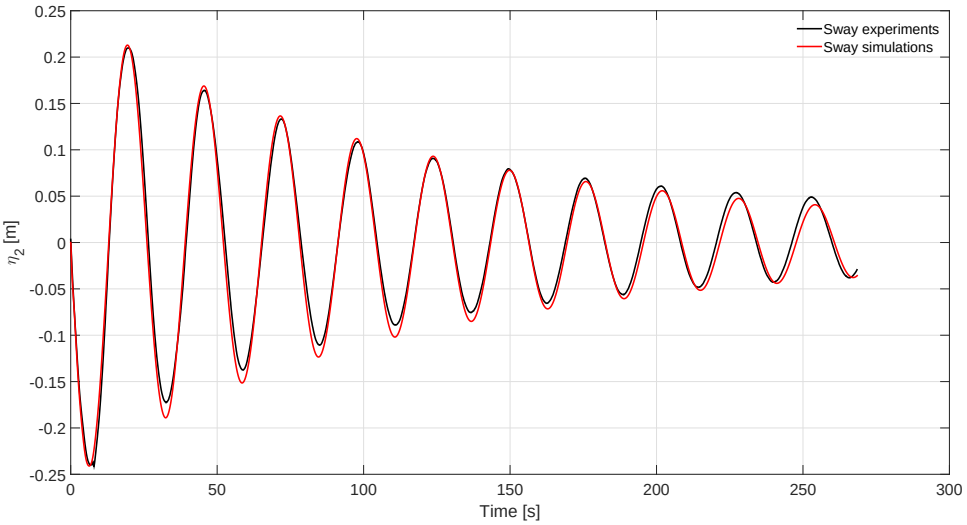

Figure 10.5: Sway decay test comparison between simulations and experiments.

10.4 Force RAO estimation

The most difficult parameters to estimate from the model experiments are force RAO, since the model was free to oscillate during all experiments. Force ROA was estimated by establishing the other hydrodynamic coefficients, such as damping, restoring, inertia and added mass by decay tests. Both the sway and roll forces are necessary to describe roll motion in beam waves. These

force RAOs are tuned to give the same results in simulation and experiments.

First, the sway force RAO was adjusted to provide similar sway behavior as the regular wave experiments. The roll moment RAO was neglected here since the contribution in sway due to roll motion is of minimal nature. Moreover, the roll RAO was adjusted in that matter that the simulation motion RAO was similar to the experiments. Figure 10.6 shows the comparison between simulated and experimental RAO without roll control.

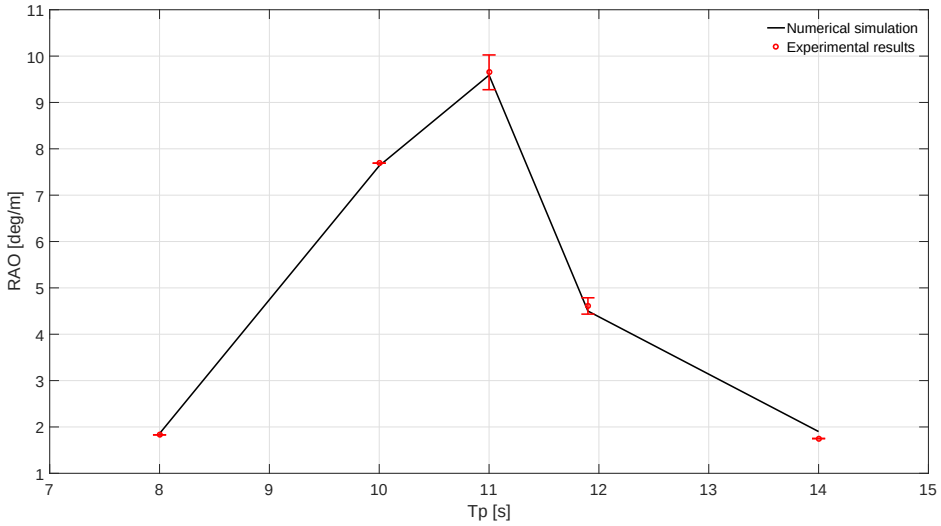

Figure 10.6: Comparison experimental vs simulation roll RAO without roll control.

10.5 Simulated response using active damping

Both decay and regular waves were simulated and compared with the experimental results, in order to determine whether the thrusters were implemented correctly. From Figure 10.4 one can see that the simulated results are close to the experimental results. From Section 10.4 it was explained that the force RAOs were adjusted in such a way that the RAO from the simulations would be comparable with the experiments. The same force RAO was tested with active roll damping, this is depicted in Figure 10.7.

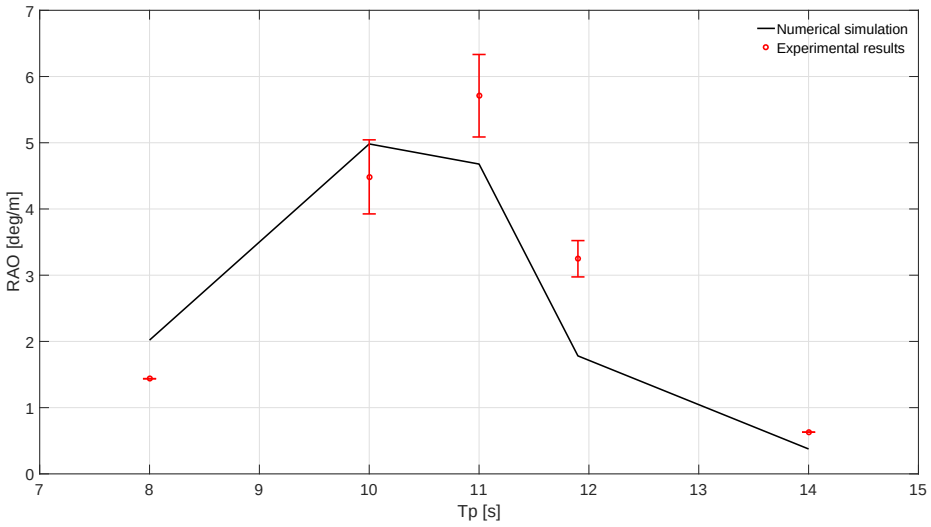

Figure 10.7: RAO comparison between experiments and simulations with active roll damping.

Figure 10.7 clearly shows a discrepancy between the experiments and the simulations. The damping is higher for wave periods larger than the natural roll period, and lower for the smaller wave periods. There are several reasons why this occurs, the most obvious one is that standard 4-quadrant open water diagrams are used, Section 9.6 showed that this was not a perfect representation. Furthermore, the frequency dependent linear damping, added mass, and force RAO could deviate from the reality. Another possible reason could be some dynamic thrust gains or losses from the wake of the propellers.

Chapter 11: Simulations

The simulation model has been described throughout this thesis and the SIMULINK model and the necessary scripts to run the simulations are enclosed in the electronic Appendix. Furthermore, the SIMULINK simulation model is illustrated in Appendix B.1. In what follows different numerical seakeeping trials that were not possible during the experiments are presented.

11.1 Roll reduction at resonance

Roll reduction at resonance was described in Section 6.1. Roll reduction at resonance is carried out in order to measure the effectiveness of the roll reduction system at resonance. The regular wave experiments , unfortunately, did not have the natural roll period calibrated (10.5 s), however the results from period equal to 10 and 11 seconds showed damping equal to 40%, see Section 9.2. The advantage of using simulations is to study the damping effect for other wave heights that were not possible during the experiments. Thus, a study was carried to determine which regular wave heights the vessel can damp efficiently. The roll reduction given wave height is presented in Figure 11.1.

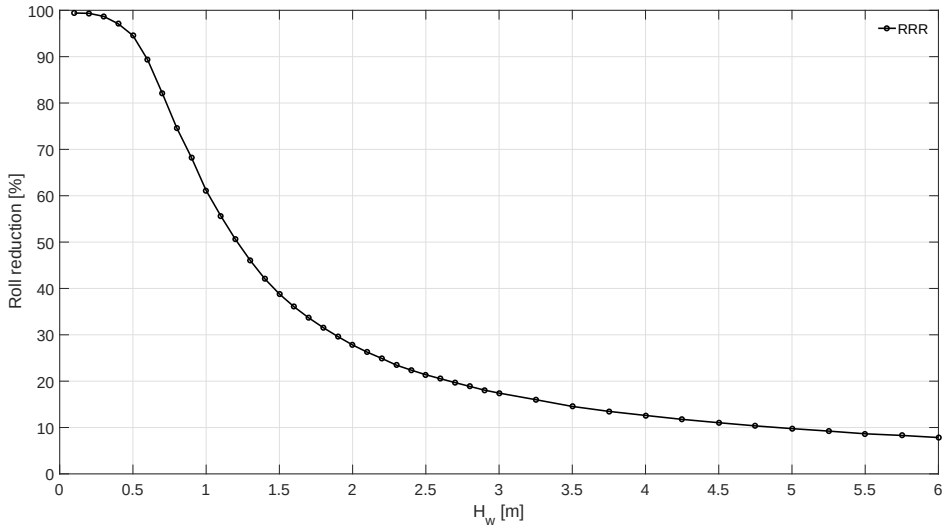

Figure 11.1: Simulated RRR with respect to wave height with wave period equal to the natural roll period.

Figure 11.1 show that the damping is above 50% for wave heights lower than 1.2 meters. The damping system can be considered inefficient for wave heights greater than 3 meters.

11.2 Improved thruster variation

The fine tuning of the control parameters and thrust variation were carried out experimentally with decay tests. To determine if this actually was the optimal parameters was the PSO-algorithm carried out for simulated irregular waves. From this, new optimal thruster limits were found. The new optimal shaft speed limit was found to be 0.4 instead of 0.223 which was used during the experiments. The new shaft speed limit represents a thruster reaction time equal to 4.1 seconds and a variation equal to 84%. From these findings was it of interest to illustrate how the choice of reaction time and thrust variation influence the damping, this is depicted in Figure 11.2

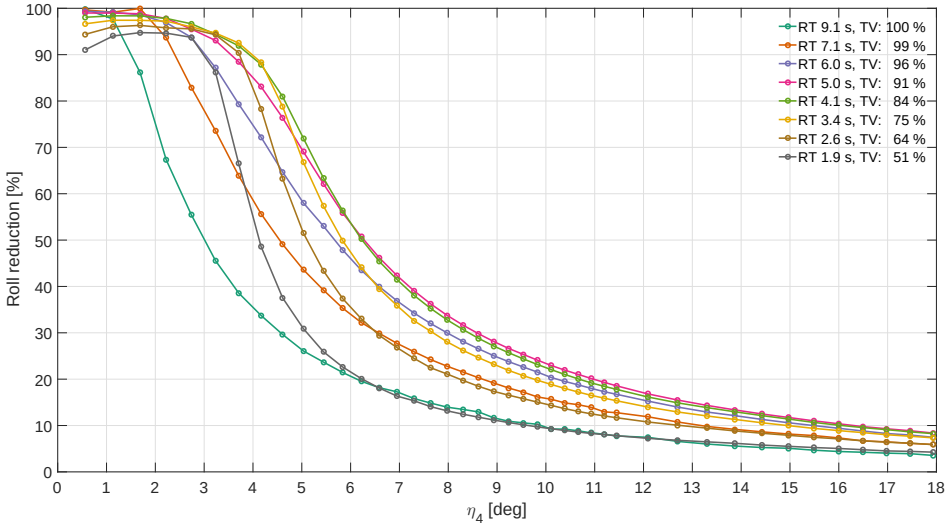

Figure 11.2: Simulated RRR with different trade-offs between reaction time (RT) and thrust variation (VT).

Figure 11.2 portrays the effect of constraining the thruster to a lower thrust limit, and the importance of choosing the correct trade-off between reaction time (RT) and thrust variation (VT). From these results it is apparent that the trade-off RT 4.1 s and TV 84% is the optimal for this study. For the rest of the simulations this thrust variation and reaction time is used.

11.3 Effect of thruster reserve

This section compares the situation where thrust reserve for DP-operations are added or neglected, i.e all available thrust will be used for roll reduction. Since the open water tests are carried out for shaft-speeds with thrust reserve (WTR), is it assumed that the thrust with no thrust reserve (NTR) will follow the same curve, which is not a perfectly valid assumption. The shaft-speeds for the thrust with no thrust reserve is found by using the experimental bollard pull Figures 7.3 and 7.4. From this graphs the following shaft speeds are found in Table 11.1.

Table 11.1: Bollard pull thrust and max shaft speed, with and without thruster reserve.

		NTR	**WTR**
Bollard pull thrust AT	T_{0_A} [N]	52	39
Bollard pull BT	T_{0_B} [N]	29	22
Max shaft speed A	T_{m_A} [RPS]	12.4	11.0
Max shaft speed BT	n_{m_B} [RPS]	15.4	13.6

Using these different shaft speeds the roll RAO can be simulated for the two different cases. It should be noted that for both cases the same control and thruster limits are used, i.e. the results from NTR could have been improved the controller was optimized. The results are depicted in Figure 11.3.

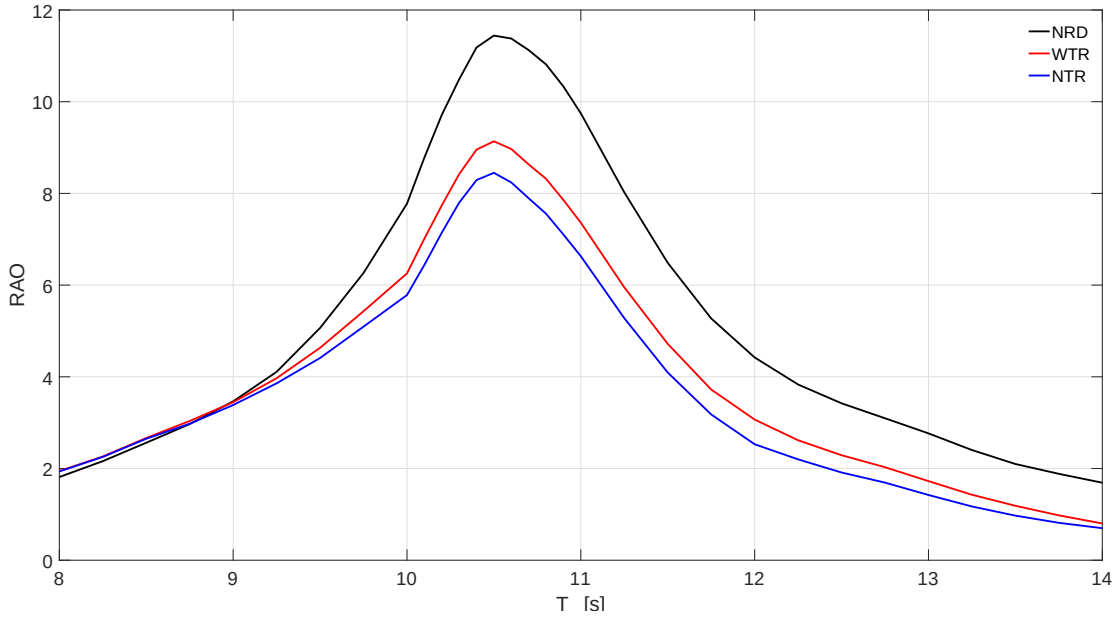

Figure 11.3: Effect of thrust reserve.

The improvement that was a result of using all available thrust to damp roll motions was largest at resonance, and was 6% larger than when thrust reserve is used.

11.4 Improved damping with respect to moment arm

It is of interest to study how the roll damping is affected by the momentum arm, i.e. the distance between the propeller hub and COR. Both the Azipull and bow thrusters have the same momentum arm, and it is assumed in this study that all of the thrusters are placed at the same distance from COR. The reference point of this study is at the bottom of the keel. The tests are carried out in the interval z=[-1.5:0.5:1.5] and are depicted in Figure 11.4.

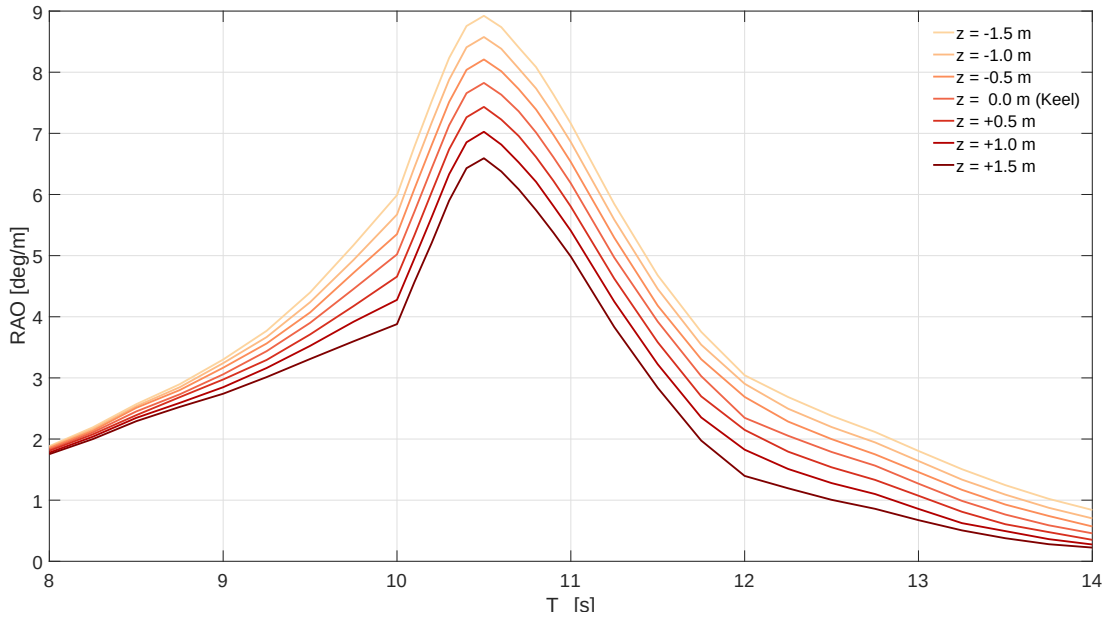

Figure 11.4: Damping with respect to increasing thruster momentum arm. Darker color represents increased arm

Figure 11.4 clearly illustrates how the damping increases with the momentum arm. The improvements are largest at resonance for obvious reasons. Linear regression analysis showed that the damping is increased with 11.2% per meter at resonance, see Figure 11.5.

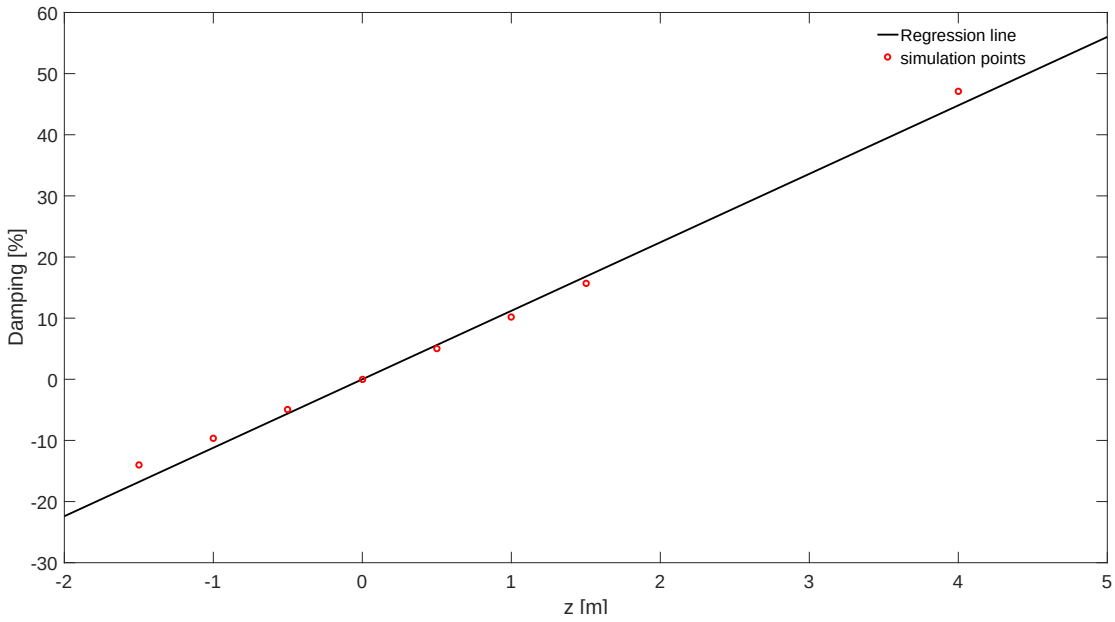

Figure 11.5: Linear least square regression of the damping with respect to the moment arm. The damping is in reference to the damping achieved at z=keel. R=0.993

11.5 Irregular wave simulations

To study the behavior in a realistic scenario, it is necessary to study the damping during irregular waves. The experiments were carried out for three different sea states with the same significant wave height. It is of importance to evaluate during which sea states the roll damping system will contribute to roll damping sufficiently. First two cases are presented where the peak period is equal to the natural roll period and the significant wave height are 1.5 and 3 meters. The case with no roll reduction (NRD) and with active roll damping (ARD) are presented in Figure 11.6 and 11.7.

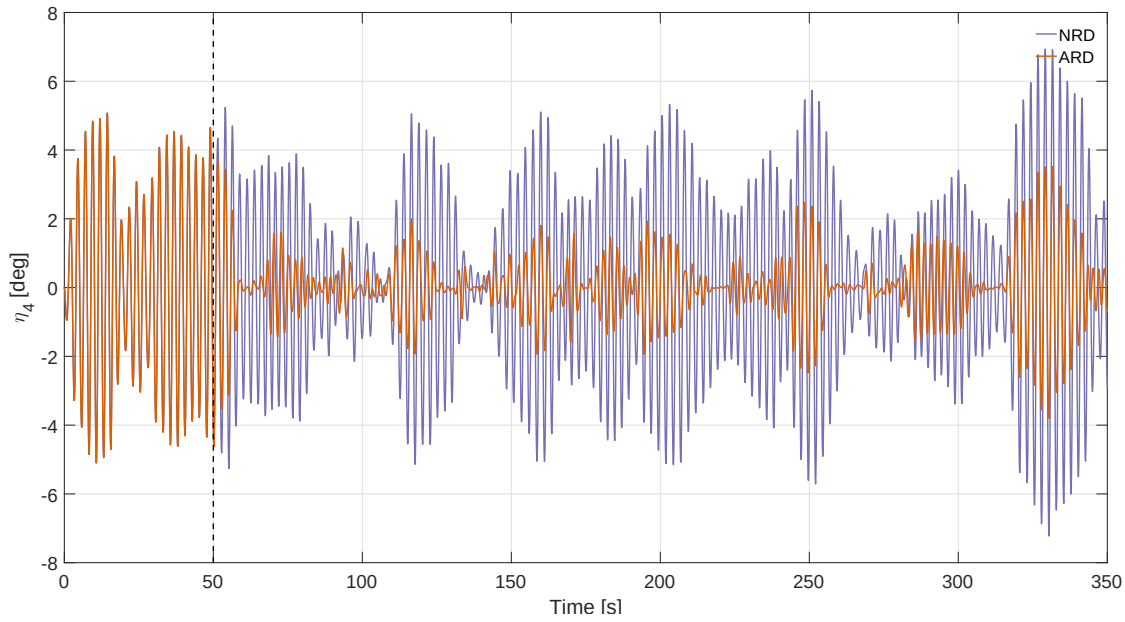

Figure 11.6: Illustration of the roll damping device for irregular waves with significant wave height equal to 1.5 meter and peak period equal to the natural roll period. Stippled line illustrates when the active roll damping system is switched on.

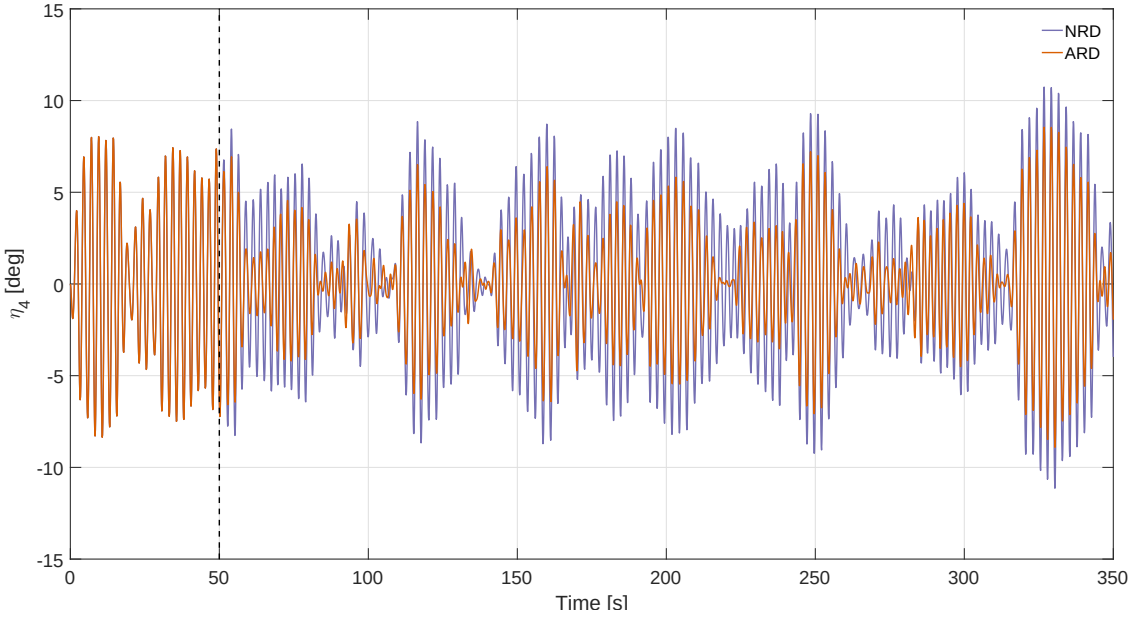

Figure 11.7: Illustration of the roll damping device for irregular waves with significant wave height equal to 3 meter and peak period equal to the natural roll period. Stippled line illustrates when the active roll damping system is switched on.

Figure 11.6 and 11.7 clearly shows that the damping contribution is larger for the sea state with the lowest significant wave height, i.e. 1.5 meter. Therefore, a trial with increasing significant wave height was carried out. Significant wave height between 0.25 and 5 meters was carried out for no roll reduction and active roll reduction. The damping of the statistical properties; mean, standard deviation (STD), root-mean-square (RMS), significant roll (η_{4s}), and maximum roll angle is presented in Figure 11.8.

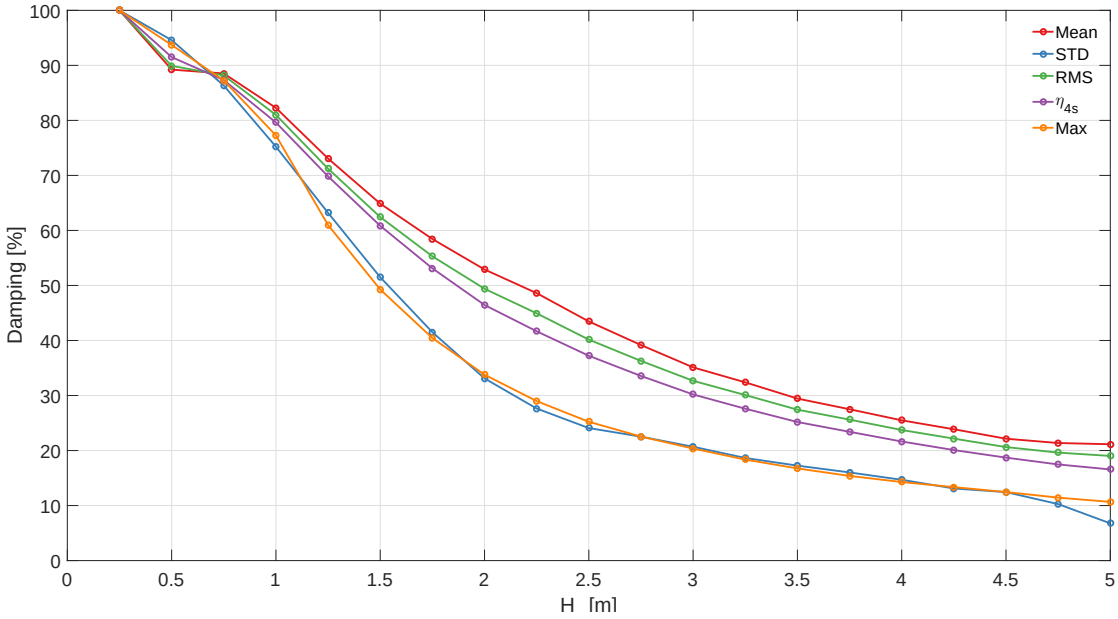

Figure 11.8: Damping with respect to significant wave heights when the peak period is equal to the natural roll period.

The figure illustrates that all statistical properties have a damping effect of more than 50% when the significant wave height is less than 1.5 meters, thus this system is especially useful during moderate sea states.

11.6 Operability analysis

It is of interest to see how much the operability can be improved by using the proposed active roll damping system. To accomplish this, it is suggested to expose the vessel with different sea sates in the waves directions (β_w) 0-180°with 10° increment. Furthermore, each of the sea states will be carried out with 20 different wave seeds. For every seed will the maximum roll and pitch angle be sampled and used to in a Gumbel distribution, see Section 6.4. The 95 percentile is used and compared with the standards of Helideck Certification Agency (2016), if the value is below the criteria, i.e. 3°, it will be defined as valid for the given sea state.

Figure 11.9 represents the flow chart of the operability process for a given peak period. The if statements introduced to the right of the chart act as a break in the loop. This is implemented because it is not necessary for the script to run 20 seeds if there is a high probability that the 95 percentile will be below the criteria. The program will update the wave direction only when the maximum roll or pitch angle are exceeded, the operability vector will then be updated with the last feasible significant wave height. The simulations are quite time-consuming, and it is estimated that for the sea peak periods represented in Figure 11.15 requests in excess of 20.000 simulations, this is the main reason why it does not exist many of these kinds of analysis in the literature according to Perez (2005, p.135).

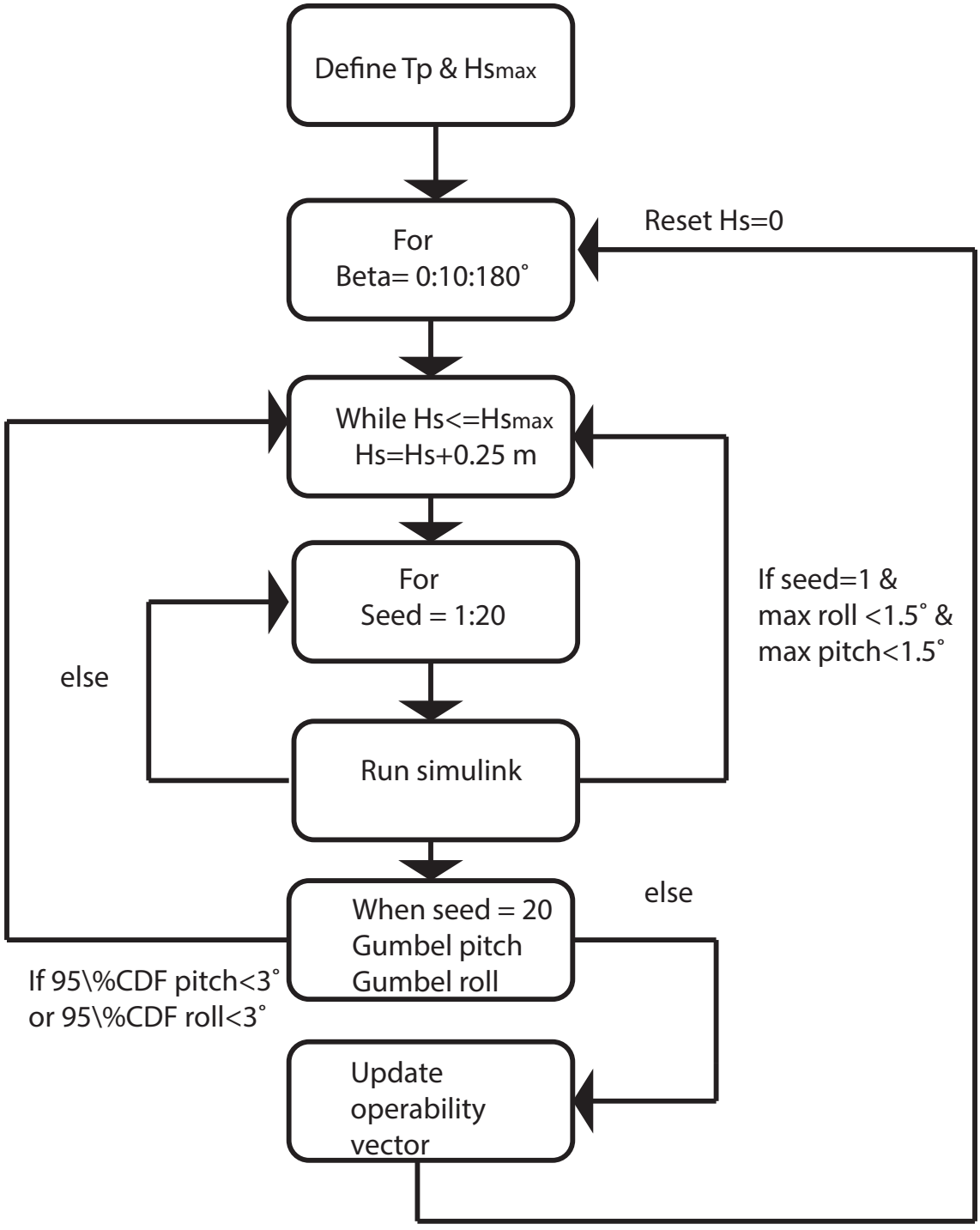

Figure 11.9: Operability flow chart.

On the following page are the operability diagrams for peak periods 8.5-12.5 presented.

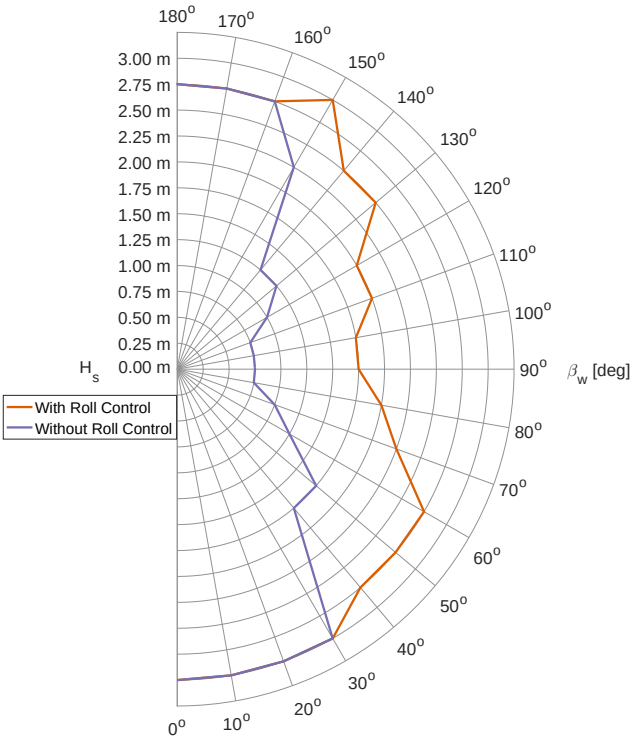

Figure 11.10: Operability diagram Tp = 8.5 s.

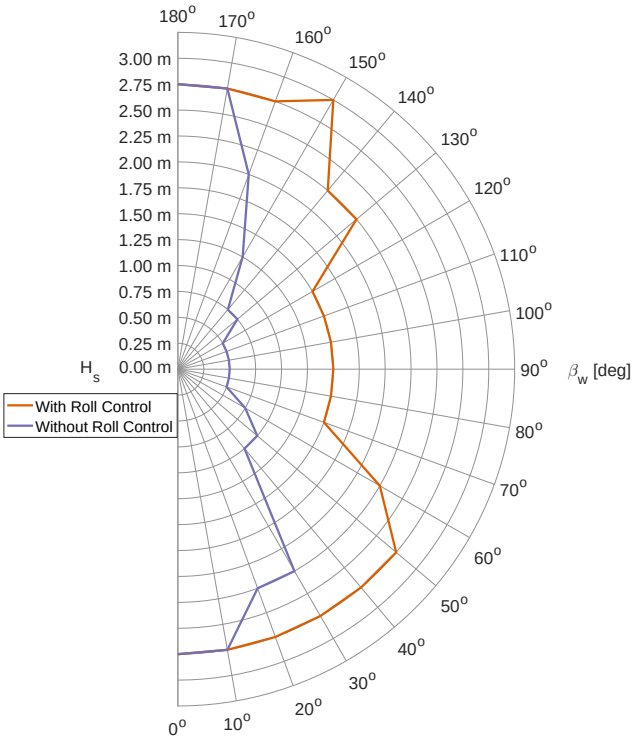

Figure 11.12: Operability diagram Tp = 9.5 s.

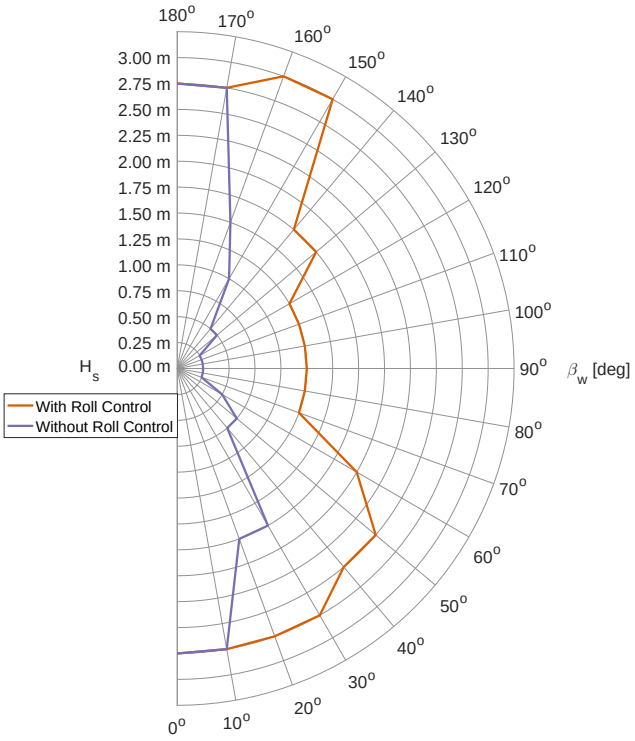

Figure 11.11: Operability diagram Tp = 10.5 s.

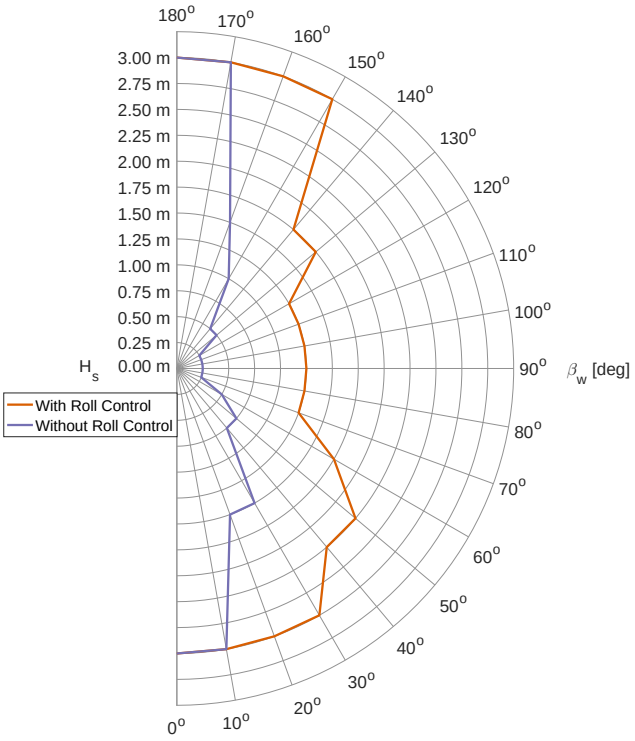

Figure 11.13: Operability diagram Tp = 11.5 s.

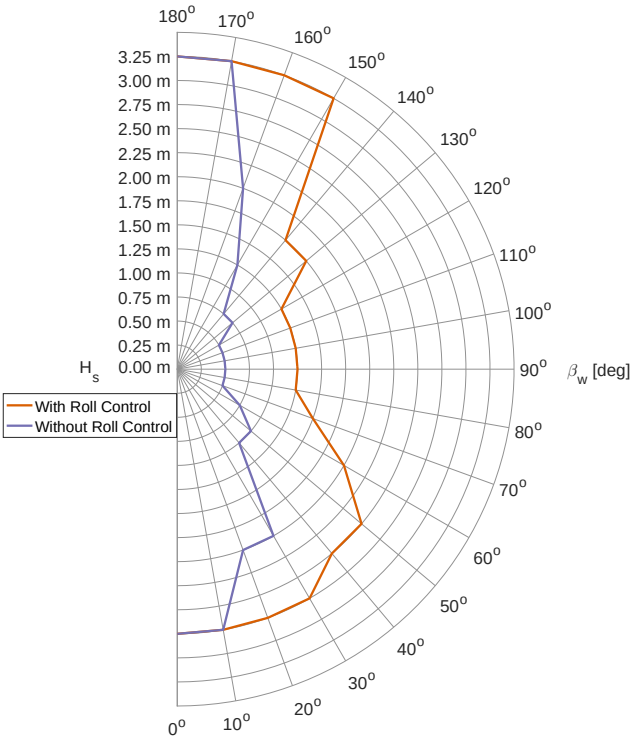

Figure 11.14: Operability diagram Tp = 12.5 s.

In general, the operability diagrams show significant improvement around beam waves, which was expected. Moreover, the effect is even larger at oblique incoming waves. This effect is because pitch motion will be the dominant motion for a larger incoming wave angle regime when active roll motions are used compared to when no roll damping systems are used. When roll control is not active the, pitch motion is the dominant motion for head sea and following sea with ±10°. When roll control is active, pitch is the dominant motion up to at least ±30°. This indicates that it will be less important to keep heading while landing a helicopter, or carrying out roll critical operations.

Furthermore, cost-benefit analyses can be made for each wave direction by using the diagrams and calculating the probability of experiencing waves below the criteria depicted in the diagrams 11.10-11.14. This is carried out using the wave statistics from the Heidrun area during 2013, provided by Haver (1985). From this data is it possible to find the distributions of wave height given peak period using a lognormal distribution:

$$
\begin{aligned}
f(h) &= \frac{1}{h \cdot s_n \sqrt{2\pi}} e^{-\frac{(ln(h)-l_n)^2}{2s_n^2}}, \\
l_n &= e^{\mu+\sigma^2/2}, \\
s_n &= (e^{\sigma^2}-1)e^{2\mu+\sigma^2}.
\end{aligned} \tag{11.1}
$$

Using this probability density function the wave heights can be distributed between peak periods 8-13 s. This is illustrated in Figure 11.15.

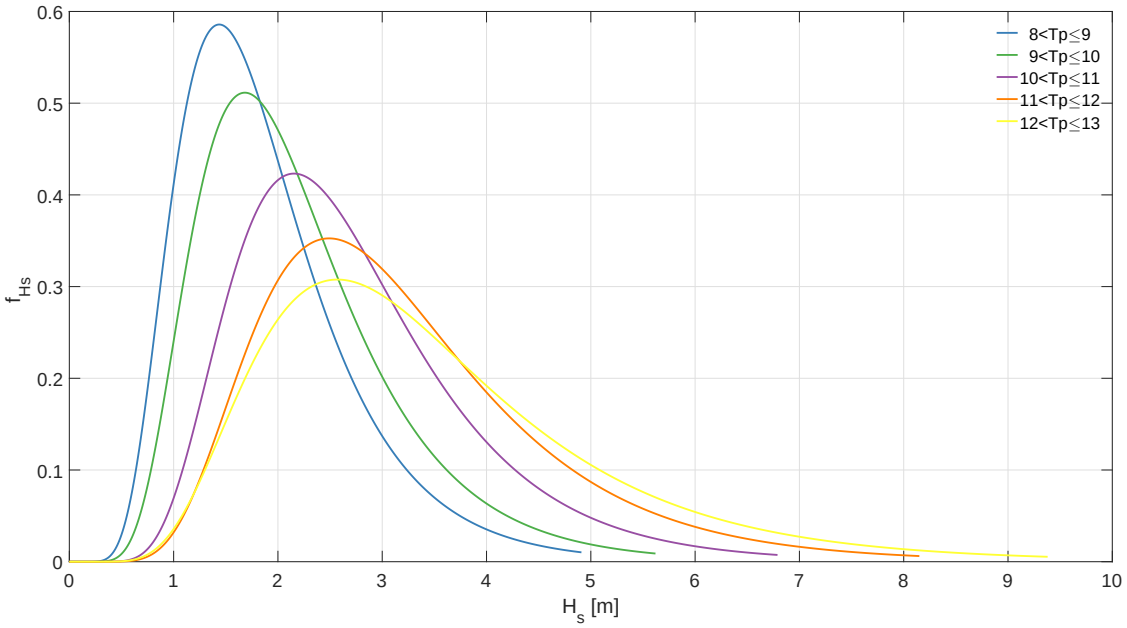

Figure 11.15: Lognormal probability density distribution of the significant wave heights given peak period.

The PTO, see Section 6.5, was calculated using the summed probability that the vessel would experience waves with lower significant wave heights depicted in the operability diagrams figures 11.10-11.14 given the peak period range 8-13 s. Equation (11.2) can be utilized to calculated the PTO with respect to incoming wave direction.

$$
PTO(\beta) = 100 \sum_{j,k} (\mathbf{Pr}(T_{p_j}) \cdot \mathbf{Pr}(H_{s_k} < OL | T_{p_j})). \tag{11.2}
$$

The operability for a unstabilized and stabilized vessel are depicted in Figure 11.16. Furthermore, the Increase in Time Operable (IPTO) due to active damping can be illustrated by using the relation found in Perez (2005):

$$IPTO = (PTO_s - PTO_u), \tag{11.3}$$

where the subscripts represents stabilized and unstabilized. The IPTO is presented in Figure 11.17.

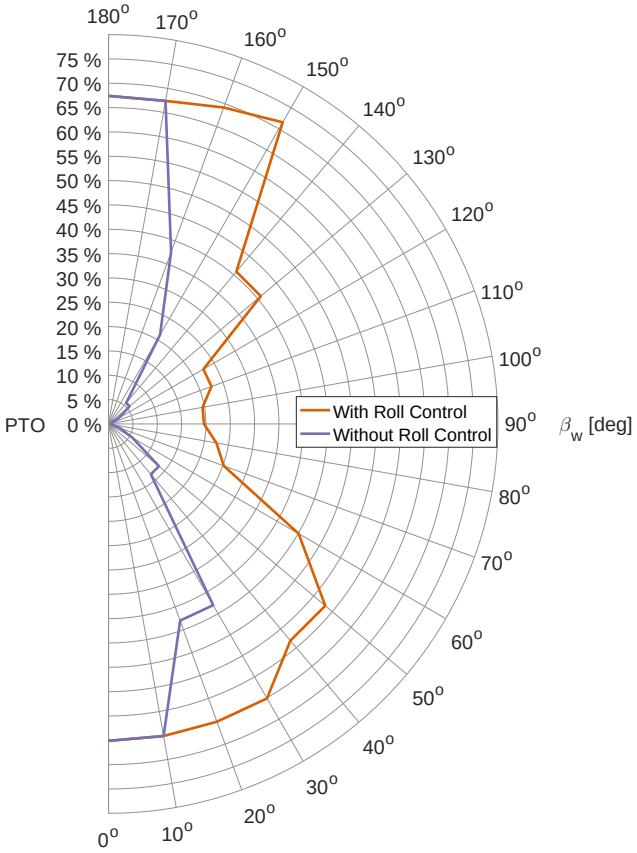

Figure 11.16: Percentage of time operable during the year 2013.

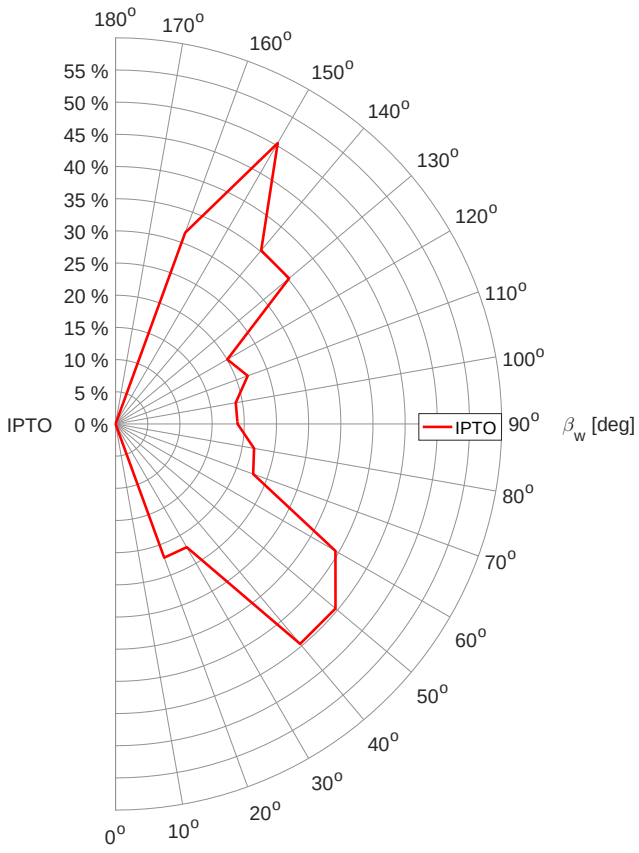

Figure 11.17: Improved percentage of time operable during the year 2013.

Figure 11.16 presents up to 72.5% percentage of time operable and the maximum improvement is 50.4% (Figure 11.17), which is a significant improvement. As mentioned is the effect largest at oblique waves, to illustrate this effect the IPTO is divided in three diagrams areas, e.g 20-60°, 70-110°, and 120-160°.

Table 11.2: Mean IPTO for three incoming wave direction regimes.

Incoming wave direction	**Mean improvement**
20-60°	34.6%
70-110°	20.9%
120-160°	34.5%

The results from Table 11.2 and the depiction from the operability diagrams indicates that a vessel can be more flexible regarding wave direction when helicopter landings take place. It could be especially useful when several incoming directions occur at the same time. Furthermore, the results depict the efficiency of the proposed active roll damping system for moderate sea states which can have several areas of use, such as increase crew efficiency, crane-operation, gangway operations. The latter operation could this system especially be useful since the operation is critical to roll motion and usually there is only a given location where the gangway can be placed, i.e. the vessel can not be flexible regarding the incoming wave direction.

Chapter 12: Conclusion and Recommendations

12.1 Conclusion

This thesis has studied the feasibility of using conventional thrusters to actively damp roll motions of vessels. Since the thrusters build thrust from 0-100% fairly slow, it was determined that more efficient roll reduction is obtained by varying the thrust between a non-zero lower limit and maximum, e.g. 20%, and 100%. The trade-off between a lower limit and the reaction time was found by optimizing the thruster reaction time with the control gains, using a PSO algorithm. Several typical trials related to roll motions were conducted experimentally in order to examine to what degree the roll motions would be damped for different conditions using the proposed anti-roll system. With the help of decay tests, it was established that the proposed active roll reduction more than doubles the damping ratio. Furthermore, a series of regular wave experiments was used to find the RAO and study the damping effect at certain wave period. It was found that 40% damping was introduced around resonance frequency. Moreover, three different irregular wave spectra were used to excite the vessel. These were long-crested beam waves with significant wave heights of 1.5 meters. The statistical roll properties, except maximum roll, was reduced somewhere between 50-70% when the proposed active roll damping system was used. This stands in contrast to today's used method of constant shaft speed, where the improvement was measured to be between 10-15% damping. Moreover, the probability of non-exceedance was calculated for peak period 11.9 seconds. The results showed that 98% of the roll peaks were below the helicopter landing criteria, i.e. 3°. Without roll control this was

calculated to be 54%. Additionally, the predicted power consumption was calculated in order to study whether the thrusters have sufficient power, and also in order to study fuel consumption. Finally, the open water characteristics were compared with the thrust and roll rate during constant shaft speed during the experiments. Two sampling methods were utilized. However, the results showed some circular behavior. This phenomenon was discussed, but no certain conclusions could be drawn from the results. Even though this effect occurs, the active roll damping system has been validated to be efficient, and it can be concluded that the system is comparable with cycloidal propulsion damping.

Additionally, a numerical simulations model was created and finely tuned regarding the findings from the experimental campaign. The main advantages of using a numerical model are that it makes it possible to study other effects that were impossible to carry out during the experiments, and also that using a numerical model utilizes the simulation model to get initial control parameters that were used during the experiments. The numerical regular waves were used to tune the trade-off between thrust variation and reaction time, and also to study the effect of the proposed active roll damping systems for larger wave heights. It was determined that the damping at resonance was above 50% if the wave heights were smaller than 1.2 meters. A study of the effect of the thruster momentum arm showed that the damping increased by 11% per meter extension. The vessel was also exposed to different numerical long-crested irregular waves, in order to examine the effect for different sea states. For the higher sea state, the effect of damping was significantly lower, due to the fact that the wave-exciting forces was so big that the thruster could not provide a sufficient counteracting moment. Lastly, operability diagrams were made for different incoming wave directions to study the increased operational time for helicopter landing on ships. This study showed that the operation time would increase with 34% for oblique waves and 20% for beam waves.

The main purpose of this thesis has been to study the feasibility and performance of a proposed active anti-roll system using conventional thrusters. Based on the results, it can be concluded that the system works very well for moderate sea states, and that the damping contributions, that is to say in moderate sea state conditions, is comparable to that of currently available anti-roll systems.

12.2 Recommendations for further work

- An investigation of the open water characteristics in oscillatory flow should be carried out experimentally, seeing as the simulation model cannot be fully utilized until all the dynamics are correctly represented.
- Review the wear and tear that will be inflicted upon the propulsion system.
- The proposed anti-roll control system should be merged with a standard DP-control system, because one would not usually sacrifice losing course and position to damp roll motions.
- Due to the fact that the model experiments validated the damping contribution, the next natural step is to carry out full-scale preliminary trials.

List of References

Bury, K. V. (1975). *Statistical Models in applied Science*. John Wiley & Sons.

Carlton, J. (1994). *Marine Propellers and Propulsion*. Butterworth-Heinemann Ltd.

Crossland, P. (2003). The effect of roll-stabilisation controllers on warship operational performance. *Control Engineering Practice*, 11(4):423–431.

Cummins, W. E. (1962). The impulse response function and ship motion. Technical report, David Taylor Model Basin.

de Oliveira, A. and Fernandes, A. (2014). The nonlinear roll damping of a FPSO hull. *Journal of Offshore Mechanics and Arctic Engineering*, 136(1).

Ehlers, S. (2012). Particle swarm algorithm-based optimization for high-strength steel structures. *Journal of Ship Production and Design*, 28(1).

Faltinsen, O. (1990). *Sea Loads on Ships and Offshore Structures*. Cambridge University Press.

Fathi, D. (2004). Shipx vessel responses (veres). Technical report, Marintek AS.

Fernandes, A., Asgari, P., and Seddigh, M. (2015). Roll center of a FPSO in regular beam seas for all frequencies. volume 7.

Fernandes, A., Asgari, P., and Soares, A. (2016). Asymmetric roll center of symmetric body in beam waves. *Ocean Engineering*, 112:66–75. cited By 0.

Fossen, T. (2011). *Handbook of Marine Craft Hydrodynamics and Motion Control*. Wiley.

Fossen, T. and Smogeli, N. (2004). Nonlinear time-domain strip theory formulation for low-speed manoeuvring and station-keeping. *Modeling, Identification and Control*, 25(4):201–221.

Haver, S. (1985). Wave climate off northern norway. *Applied Ocean Research*, 7(2):85–92.

Healey, A., Rock, S., Cody, S., Miles, D., and Brown, J. (1995). Toward an improved understanding of thruster dynamics for underwater vehicles. *IEEE Journal of Oceanic Engineering*, 20(4):354–361.

Helideck Certification Agency (2016). Helideck Limitations List Part C. Retrived 31st of March 2016, from http://www.helidecks.org/download

Huse, E. and Børresen, R. (1983). Heave, pitch, and roll damping of platforms and ships due to positioning thrusters. volume 3, pages 209–219.

Häusler, A., Saccon, A., Hauser, J., Pascoal, A., and Aguiar, A. (2013). Four-quadrant propeller modeling: A low-order harmonic approximation. volume 9, pages 161–166.

Häusler, A., Saccon, A., Hauser, J., Pascoal, A., and Aguiar, A. (2015). A novel four-quadrant propeller model.

Jalkanen, J. (2006). Particle swarm optimization of load carrying structures. *J, Structural Mechanics*, 2:23–35.

Jürgens, D. and Palm, M. (2009). Voith schneider propeller - an efficient propulsion system for dp controlled vessels.

Kennedy, J. and Eberhart, R. (1995). Particle swarm optimization, *Proceedings*. In *IEEE Institute of Electrical and Electronics Engineers, International Conference on Neural Networks, Piscataway*, volume 4, pages 1942–1948. IEEE Service Center, Piscataway, NJ.

Miniovich, I. Y. (1960). Investigation of hydrodynamic characteristics of screw propellers under conditions of reversing and calculation methods for backing of ships. *Buships Translation 697*.

Monk, K. (1987). A warship roll criteria. *Transactions of RINA*.

Newman, J. N. (1977). *Marine Hydrodynamics*. The MIT Press.

Ogilvie, T. F. (1964). Recent progress toward the understanding and prediction of sship motions. *The Fifth Symposium on Naval Hydrodynamics pp. 3 - 128*.

Perez, T. (2005). *Ship Motion Control: Course Keeping and Roll Reduction using Rudder and Fins*. Springer-Verlag,London, UK.

Perez, T. and Fossen, T. I. (2009). A matlab tool for parametric identification of radiation-force models of ships and offshore structures. modelling, identification and control, mic-30(1):1-15. http://www.marinecontrol.org/.

Pérez, T.erez, T. and Fossen, T. (2008). Time-vs. frequency-domain identification of parametric radiation force models for marine structures at zero speed. *Modeling, Identification and Control*, 29(1):1–19.

Price, W. C. and Bishop, R. E. D. (1974). *Probabilistic theory of ship dynamics*. Chapman and Hall, London.

Rudaa, S. (2015). Use of coventional thrusters for roll damping for ships. Unpublished project thesis, Department of Marine Technology, NTNU Trondheim.

Salvesen, N., Tuck, E. O., and Faltinsen, O. (1970). Ship motions and sea loads. *The Society of Naval Architects and Marine Engineers - SNAME*, 78:250–87.

Sellars, F. H. and Martin, J. P. (1992). Selection and evaluation of ship roll stabilization systems. *SNAME: pp. 84-101*.

Smogeli, Ø. N. (2006). *Control of Marine Propellers: From Normal to Extreme Conditions*. PhD thesis, Norwegian University of Science and Technology (NTNU).

Söding, H. (2004). Rolldampfung mittels voith schneider-technologie (german).

Steen, S. (2014a). Experimental methods in marine hydrodynamics. TMR 7 Lecture Notes.

Steen, S. (2014b). Foil and propeller theory. Lecture Notes.

van den Boom, H., editor (2010). *Helicopter Operations for Offshore Ships*, 6.0. MARIN.

van Lammeren, W. P. A., van Manen, J. D., and Oosterveld, M. W. C. (1969). Wageningen b-screw series. *Transactions of SNAME*.

Voth Scheider (2006). Offshore Supply Vessels equipped with Voith Schneider Propellers. Retrived 20th of March 2016 from: http://www.dieselduck.info/machine/02

Weinblum, G. and St.Denis, M. (1950). On the motion of ships at sea. *Trans. SNAME*.

White, A. (2013). Limits to control of ship capsize using cycloidal propellers compared to active fins. *World Journal of Modelling and Simulation*, 9(2):130–138.

Appendix A: Propeller model

A.1 Wageningen Fourier series

Table A.1: Wageningen B4-70 propeller 4-quadrant model Fourier coefficients.

k	A_T	B_T	A_Q	B_Q
0	2.5350E-02	0.0000E-00	2.4645E-03	0.0000E-00
1	1.7820E-01	-7.4777E-01	2.6718E-02	-1.1081E-01
2	1.4674E-02	-1.3822E-02	1.6056E-03	1.5909E-04
3	2.8054E-02	1.0077E-01	6.5822E-03	1.6455E-02
4	-1.6328E-02	-1.1318E-02	-2.2497E-03	-2.0601E-03
5	-5.3041E-02	4.7186E-02	-7.8062E-03	8.5343E-03
6	6.0605E-04	1.0666E-02	2.4126E-04	8.7856E-04
7	3.6823E-02	-9.0239E-03	6.1475E-03	-3.1327E-03
8	-2.5429E-03	-7.8452E-03	-1.6065E-03	-9.6650E-04
9	-1.7680E-02	2.3941E-02	-3.3291E-03	4.3190E-03
10	2.7331E-03	8.0787E-03	1.2311E-03	1.2453E-03
11	2.1436E-02	-1.4942E-04	3.1123E-03	9.5986E-05
12	-2.4782E-03	-3.1925E-03	-1.2559E-03	-7.9986E-04
13	1.2317E-03	9.2620E-03	1.3948E-03	1.5073E-03
14	5.0980E-03	1.5527E-03	8.8397E-04	2.4595E-04
15	7.8076E-03	-6.5683E-03	5.0358E-05	-1.6918E-03
16	-3.7816E-03	-6.1655E-04	-7.9990E-04	5.1603E-04
17	3.5353E-03	5.1033E-03	1.3345E-03	1.1504E-03
18	5.3014E-03	-6.0263E-04	1.1928E-03	-4.7976E-04
19	2.1940E-03	-8.2244E-03	-1.3556E-04	-1.4566E-03
20	-2.8306E-03	-6.3789E-04	-7.0825E-04	2.3280E-04

A.2 Values from the experiments conduced by Huse and Børresen (1983)

Table A.2: Values from the experiments conduced by Huse and Børresen (1983)

No force on thrusters		2/3 of full power on thrusters	
Time [s]	Roll [deg]	Time [s]	Roll [deg]
0.4792	6.3770	0.3895	13.1356
2.4391	5.9481	2.3004	7.2034
4.4754	4.7632	4.2435	3.6441
6.4478	3.7201	6.1576	2.4576
8.5307	3.2437	8.2492	1.7797
10.4287	2.8622	10.0334	1.1864
12.4496	2.4332	11.8197	0.4237
14.4086	2.0515	13.9041	0.3390
16.3647	1.8116	15.6208	0.2542
18.3865	1.3353	17.6429	0.2542
20.2788	1.2373	19.8509	0.0847

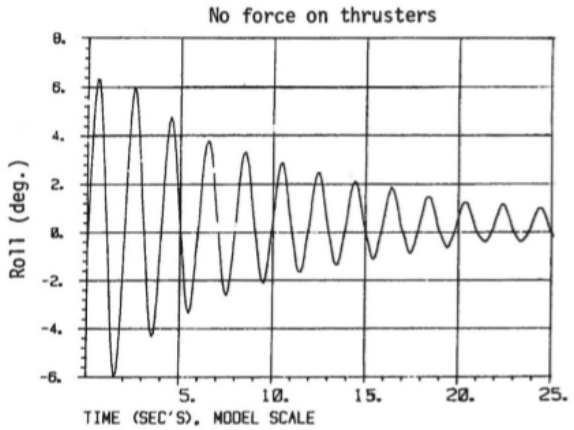

Figure A.1: Experiments from Huse and Børresen (1983), no force on thrusters

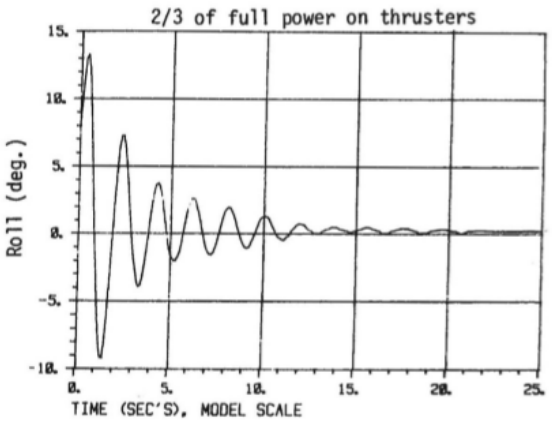

Figure A.2: Experiments from Huse and Børresen (1983), 2/3 of full power on thrusters

Appendix B: Simulink Blocks

Color coding of Simulink blocks:

- **GREEN**: Sources (inputs ports, constants, etc.)
- **RED**: Sinks (output ports, terminators, to workspace blocks, etc.)
- **CYAN**: Memory blocks: Integrators, unit delays, memory, transfer functions, state space blocks, etc.
- **ORANGE**: GOTO blocks.
- **MAGENTA**: FROM blocks.
- **YELLOW**: All remaining blocks.

B.1 Simulation model

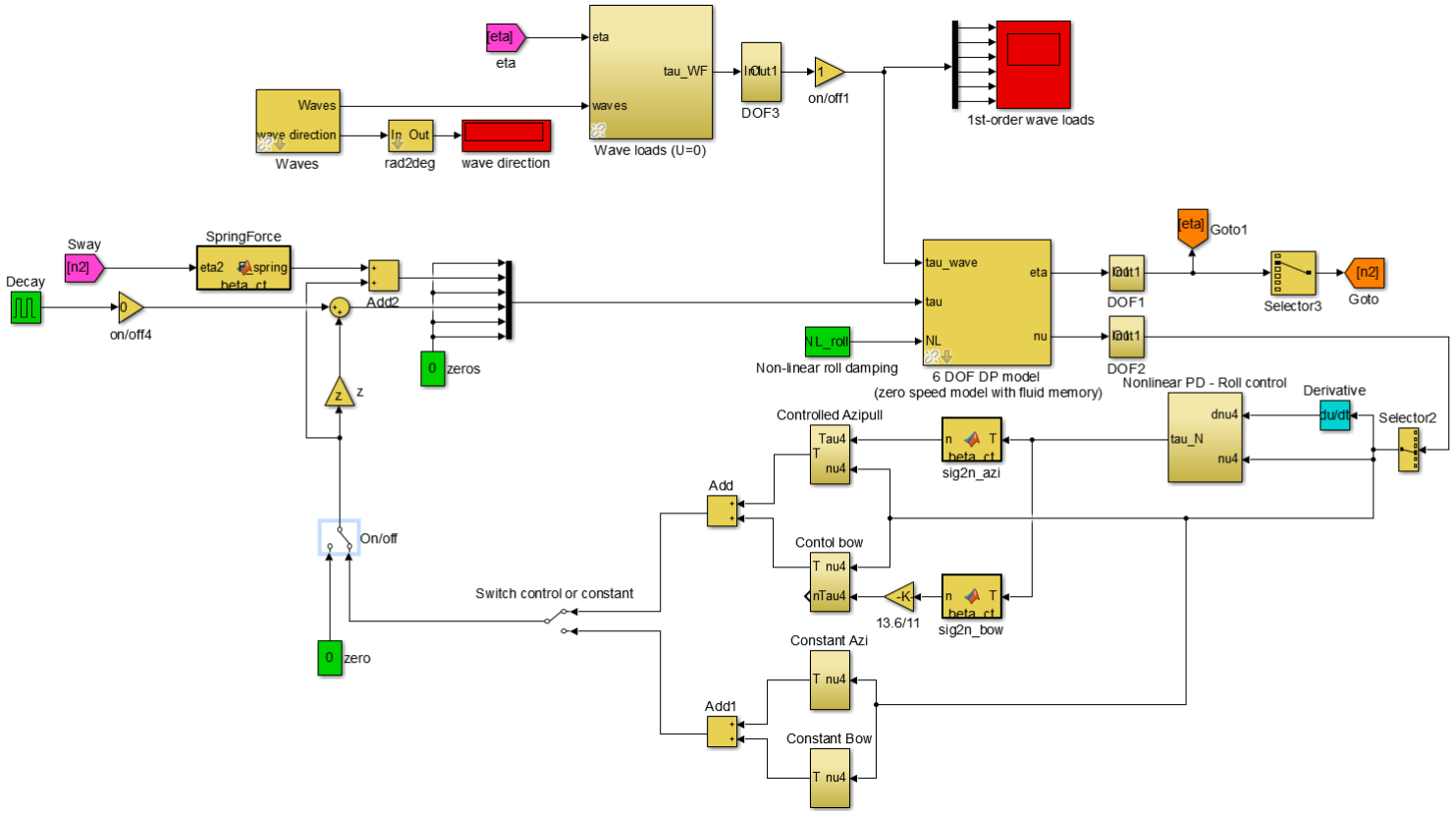

Figure B.1: Simulation model. Consisting of wave and decay load generators, ship model, nonlinear PD roll control, and thruster allocation.

B.2 Thruster allocation

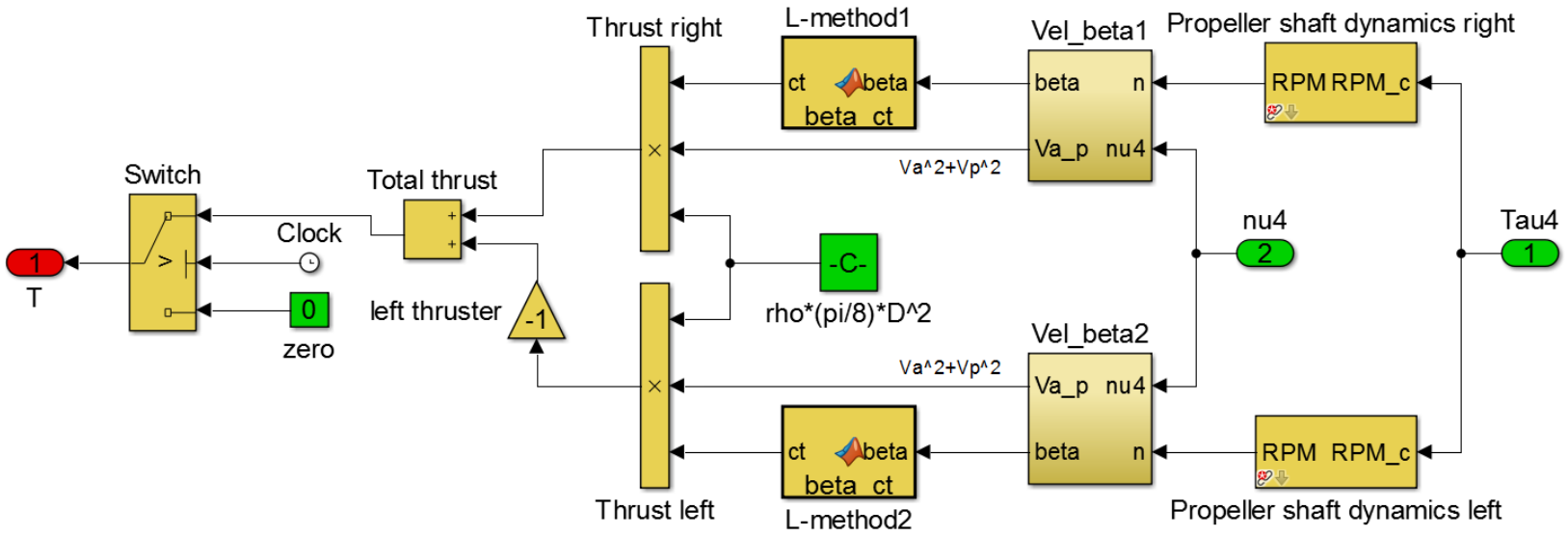

Figure B.2: Thruster allocation: Containing shaft speed dynamics and thrust calculation using L-method. The switch is added because the first time-step will give NaN.

Appendix C: Additional Information

C.1 Pump efficiency

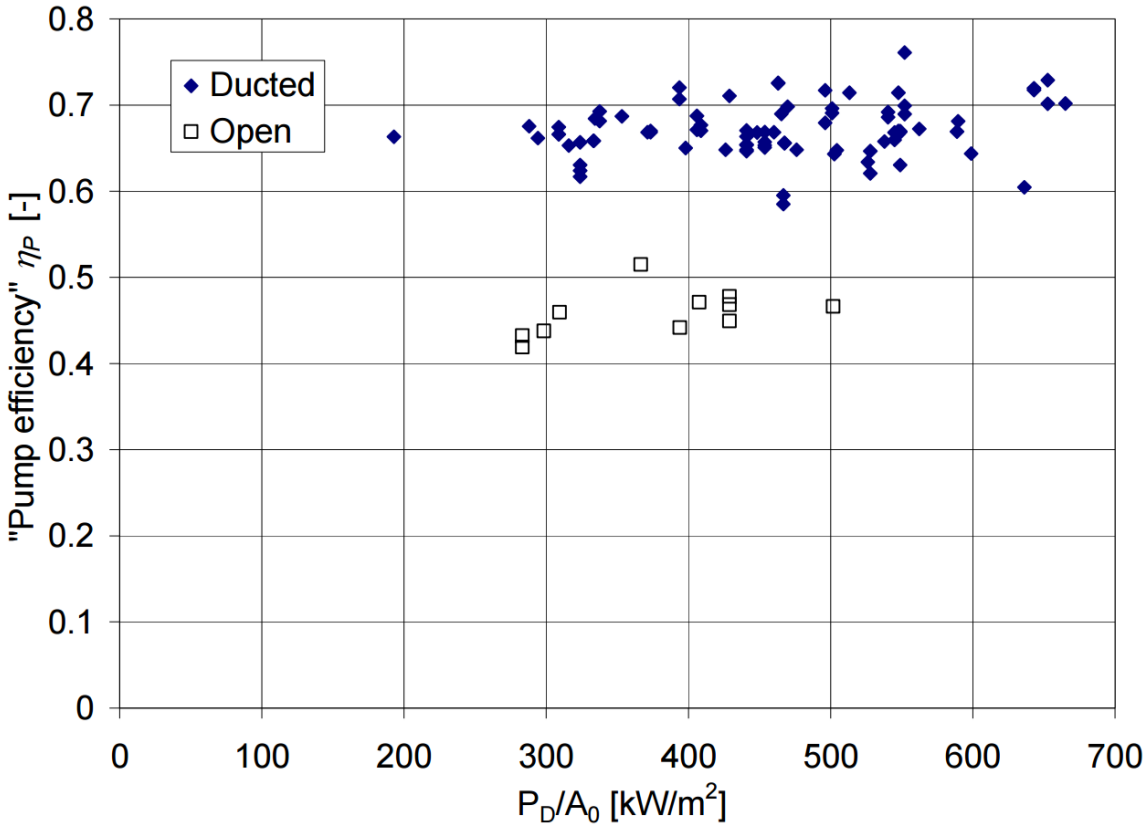

Figure C.1: Pump efficiency as function of the propeller power density, based on a regression on bollard pull model test at MARINTEK. Found from the lecture notes of Sverre Steen referanse.

Appendix D: Wave Calibration

This appendix contains the waves that were used for the experimental trials. Section D.1 illustrates the how the wave amplitudes behaves over time, and Section D.2 shows the irregular wave amplitudes. The amplitudes ζ are scaled to full scale and the time is model scale.

D.1 Regular Waves

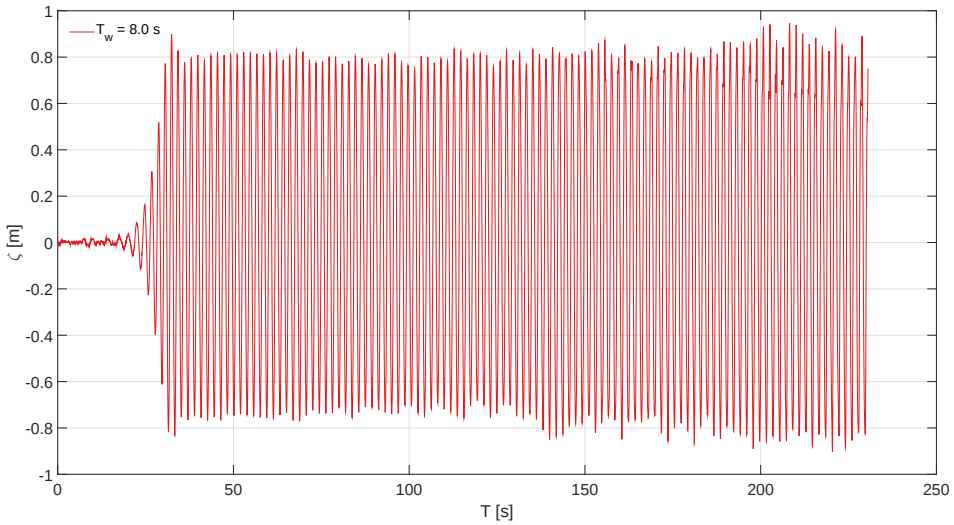

Wave elevation over time for period full scale equal to 8 seconds.

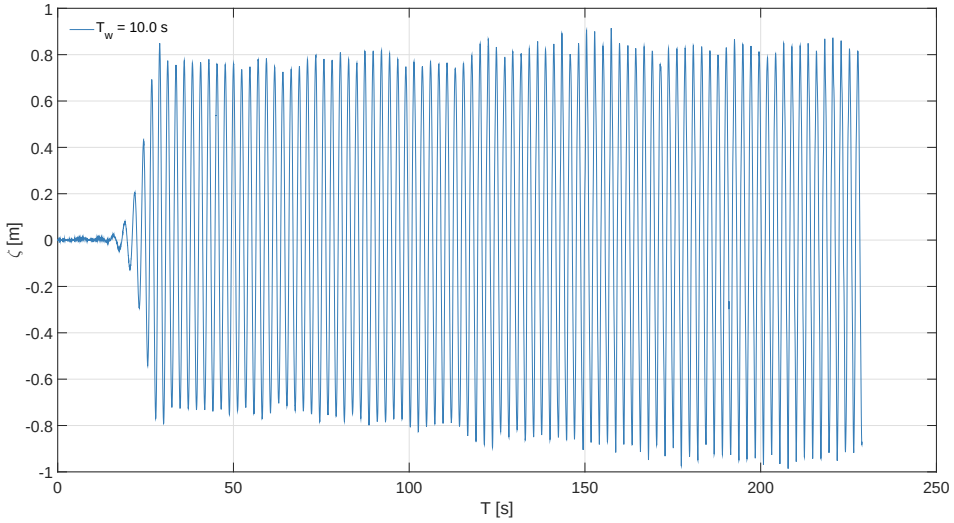

Wave elevation over time for period full scale equal to 10 seconds.

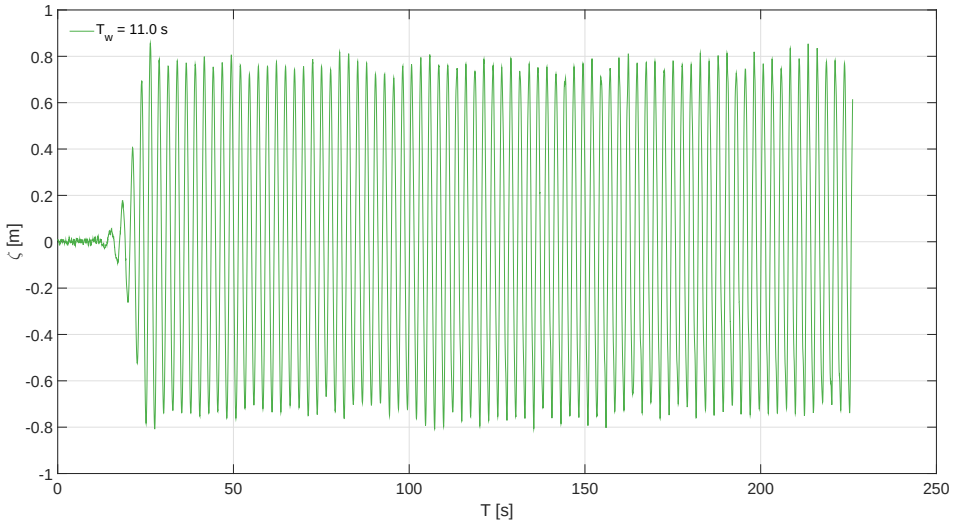

Wave elevation over time for period full scale equal to 11 seconds.

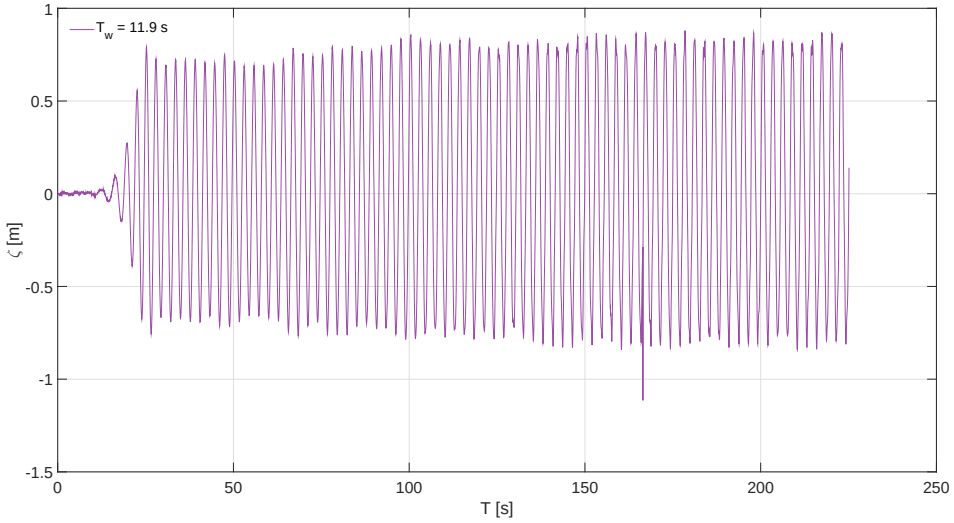

Figure D.1: Wave elevation over time for period full scale equal to 11.9 seconds.

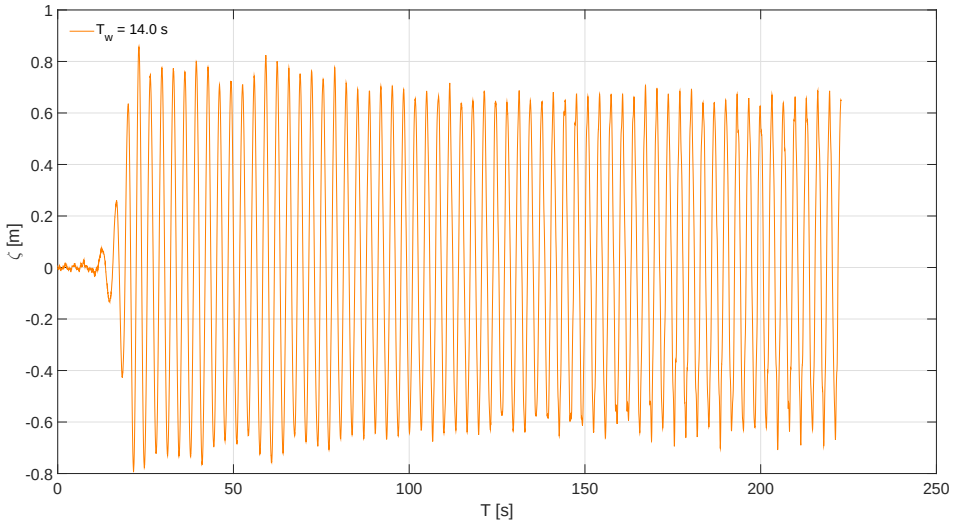

Figure D.2: Wave elevation over time for period full scale equal to 14 seconds.

D.2 Irregular Waves

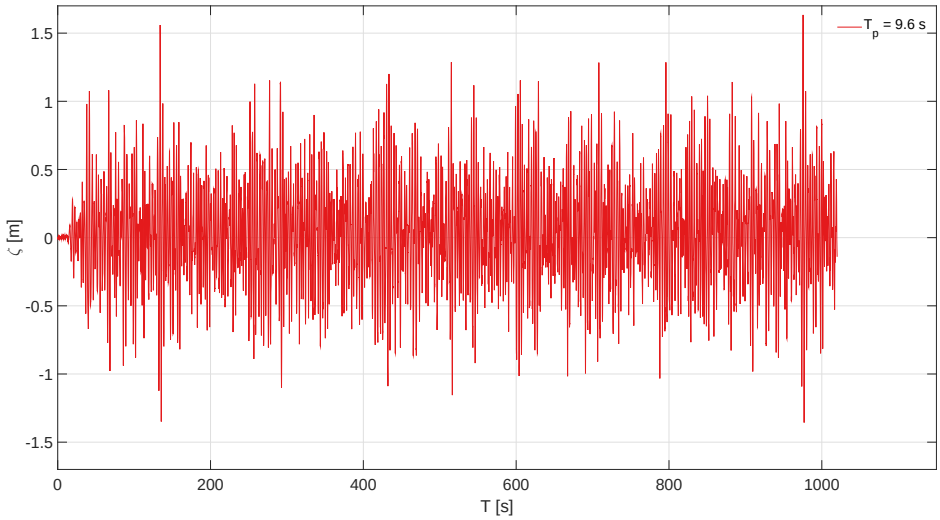

Figure D.3: Wave elevation over time for peak period full scale equal to 9.6 seconds.

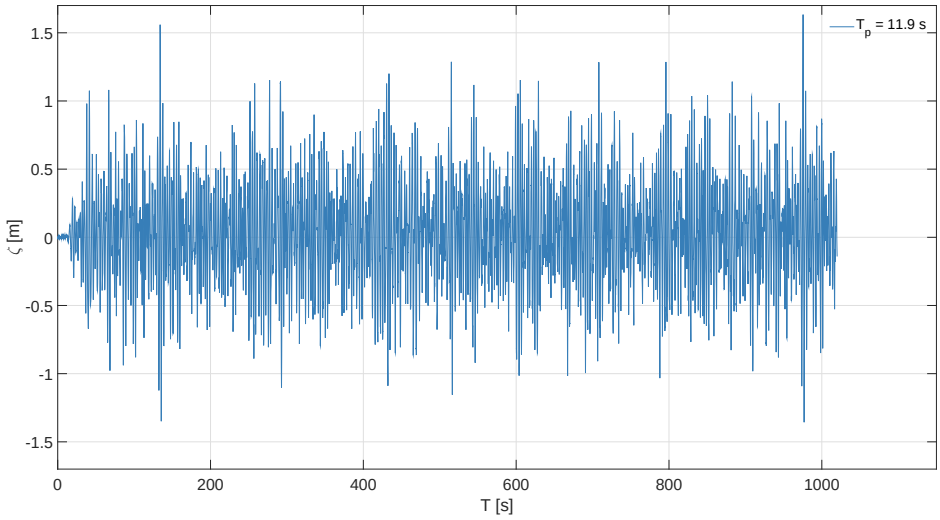

Figure D.4: Wave elevation over time for peak period full scale equal to 11.9 seconds.

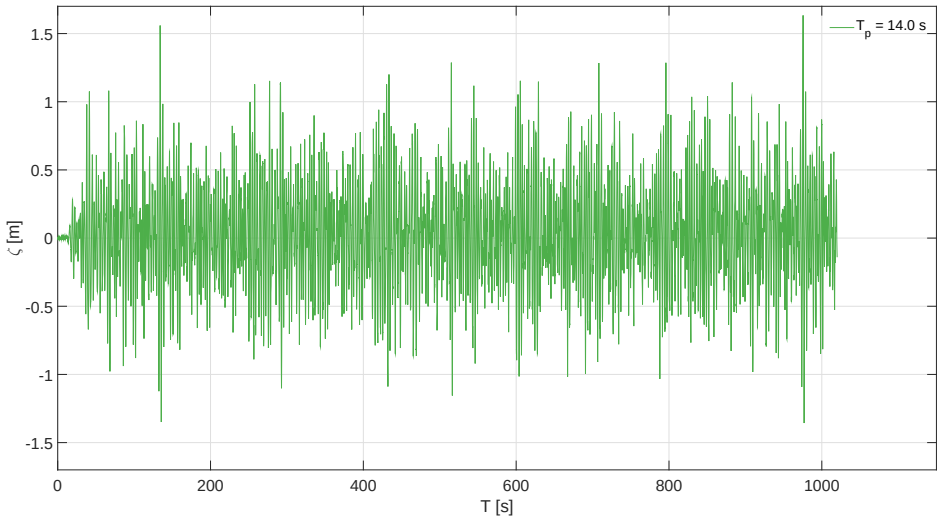

Figure D.5: Wave elevation over time for peak period full scale equal to 14 seconds.

Appendix E: Electronic appendix

This appendix contains the description of the enclosed electronic appendix. The folders are structured as follows:

Folder: Simulation model

- **main.m:** Script used for running simulations.
- **M_visc.mat:** Structs containing the values from VERES and retardation functions.
- **t_r.m:** Estimates the reaction time.
- **modHydro.m:** Modifies the hydrodynamic coefficients from VERES.
- **RollDampingSim.slx:** SIMULINK simulation model.

Folder: Movie

- **Decay.mp4:** Movie of the decay test with and without roll control.
- **Irregular_wave_11_9.mp4:** Movie of the experiments with and without roll control during irregular waves.

Folder: Poster

- **Poster.pdf:** Poster presentation of thesis for the Master Poster Exhibition 2016.

Folder: Experimental results

- **Folder runs:** Contains all the experimental runs that were stored, represented in binary form.
- **catman_read_5r8.m:** Post-processing script 1.
- **num2catman:** Post-processing script 2.
- **Open_water_azipull.xlsx:** Results form open water tests for Azipull thrusters.
- **Open_water_bow.xlsx:** Results form open water tests for bow thrusters.
- **UDP.slx:** SIMULINK model used for experimental trials.

The experimental trials relevant to this master thesis are represented Section E.2. Furthermore, the description of the channels used during the experiments is explained in section E.1.

E.1 Experimental measurements

The measurements contains 66 different channels, however, not all of them are used. The signals not used are defined as Not Used (NU). The channels also distinguishes between Measured Signal (MS) and Control Signal (CS). The former represents what actually is measured. The latter, represents the signals the vessel were receiving from the computer. The control signals was only used to study if there occurred any discrepancy during measurements. The abbreviations used in the descriptions are presented in Table E.1 and the channel list is presented in Table E.2.

Table E.1: Abbreviation list.

Abbreviation	
NU	Not used
MS	Measured signal
CS	Control signal
SF	Sampling frequency
BT	Bow thruster
SP	Starboard pointing
PP	Port pointing

Table E.2: Channel list.

Channel	Channel Name	Unit	SF [Hz]	Description
1	DAQ time stamps	[s]	25	Time series for SF 25
2	DAQ time stamps SR2	[s]	200	Time series for SF 25
3	DAQ time stamps absolute	[h:m:s]	25	Time series for SF 25 (NU)
4	DAQ time stamps absolute SR2	[h:m:s]	200	Time series for SF 200 (NU)
5	n72_vel_ctrl	[rps]	200	CS: shaft speed BT 2
6	n70_vel_ctrl	[rps]	200	CS: shaft speed BT 1
7	n69_vel_ctrl	[rps]	200	CS: shaft speed AT 1
8	n71_vel_ctrl	[rps]	200	CS: shaft speed AT 2
9	n09_pos_ctrl	[deg]	200	CS: AT rudder 2
10	n11_pos_ctrl	[deg]	200	CS: AT rudder 1
11	n72_vel_meas	[rps]	200	MS: shaft speed BT 2
12	n70_vel_meas	[rps]	200	MS: shaft speed BT 1
13	n69_vel_meas	[rps]	200	MS: shaft speed AT 1
14	n71_vel_meas	[rps]	200	MS: shaft speed AT 2
15	n09_pos_meas	[deg]	200	MS: AT rudder 2 (NU)
16	n11_pos_meas	[deg]	200	MS: AT rudder 1 (NU)
17	NTP time stamps QX SR2	[s]	200	NU
18	framenumber	[-]	25	NU
19	errorcode	[-]	25	NU
20	xpos1	[m]	25	Surge
21	ypos1	[m]	25	Sway
22	zpos1	[m]	25	Heave
23	roll1	[deg]	25	Roll
24	pitch1	[deg]	25	Pitch
25	yaw1	[deg]	25	Yaw
26	residual1	[-]	25	NU

Continued on next page

Table E.2 – *Continued from previous page*

Channel	**Channel Name**	**Unit**	**SF [Hz]**	**Description**
27	utralab_status	[-]	25	NU
28	wave_1	[m]	25	Wave amplitudes
29	wave_ref	[m]	25	NU
30	NTP time stamps QX	[s]	25	NU
31	fx-for-8701	[N]	200	X-Spring forces in front of model
32	fy-for-8692	[N]	200	Y-Spring forces in front of model
33	fx-aft-8704	[N]	200	X-Spring forces in stern of model
34	fy-aft-8644	[N]	200	Y-Spring forces in stern of model
35	Fx-SB-Thr-20514	[mV]	200	(NU)
36	Fy-SB-Thr-20522	[mV]	200	(NU)
37	Fx-BB-Thr-20513	[mV]	200	(NU)
38	Fy-BB-Thr-20516	[mV]	200	(NU)
39	Carriage_speed	[m/s]	200	Carriage speed, zero-speed (NU)
40	Fy-Thr-1-20258	[N]	200	Y-force for bow thruster 1
41	Fy-Thr-2-20263	[N]	200	Y-force for bow thruster 2
42	Acc1-x	[m/s²]	200	Acceleration in X for BT
43	Acc1-y	[m/s²]	200	Acceleration in Y for BT
44	Acc1-z	[m/s²]	200	Acceleration in Z for BT
45	Acc2-x	[m/s²]	200	Acceleration in X for AT
46	Acc2-y	[m/s²]	200	Acceleration in Y for AT
47	Acc2-z	[m/s²]	200	Acceleration in Z for AT
48	Mom-Thr1	[Nm]	200	Torque for BT 1
49	Mom-Thr2	[Nm]	200	Torque for BT 2
50	Mom-SB	[Nm]	200	Torque for SP AT
51	Mom-BB	[Nm]	200	Torque for PP AT
52	Roll-Rate	[deg/s]	200	Roll rate
53	Pitch-Rate	[deg/s]	200	Pitch rate (NU)

Continued on next page

Table E.2 – *Continued from previous page*

Channel	Channel Name	Unit	SF [Hz]	Description
54	Yaw-Rate	[deg/s]	200	Yaw rate (NU)
55	rps-Thr1	[Hz]	200	NU
56	WAVE1	[m]	25	Wave amplitude
57	RPS-SB-THR	[rps]	200	Shaft speed for SP AT
58	RPS-BB-THR	[rps]	200	Shaft speed for PP AT
59	RPS-THR01	[RPS]	200	Shaft speed for BT 1
60	RPS-THR02	[RPS]	200	Shaft speed for BT 2
61	SB-THR	[deg]	200	Rudder SP AT
62	BB-THR	[deg]	200	Rudder pointing pointing AT
63	FX-SB-THR	[N]	200	X thruster force for SP AT
64	FY-SB-THR	[N]	200	Y thruster force for SP AT
65	FX-BB-THR	[N]	200	X thruster force for PP AT
66	FY-BB-THR	[N]	200	Y thruster force for PP AT

E.2 Experimental trials

The following table contains the different experimental trials used to find the results presented in this thesis. The runs are sorted with respect to the different seakeeping trials and waves. The necessary experimental runs are presented in Table E.3 and E.4.

Table E.3: Run list.

Test	**Run number**
Decay	10**
Regular wave (model)	20**
Irregular wave (model)	30**
Regular wave (calibration)	80**
Irregular wave (calibration)	81**

The results from the different runs can be found by using the enclosed function *num2catman*. This function takes the run number as input and utilizes the *catman_read_5r8* function, written by Dr. Andreas Geissler, and returns the struct c. To find the data stored in the struct, simply write c(run_number).data.

Table E.4: Experimental runs.

Run number	**Name**	**Comment**
1003	Roll decay	No active damping
1007	Roll decay	No active damping
1025	Roll decay	No active damping
1047	Roll decay	No active damping
1015	Roll decay	Constant shaft speed 150%
1018	Roll decay	Constant shaft speed 150%
1028	Roll decay	Constant shaft speed 150%
1016	Roll decay	Constant shaft speed 150%
1048	Roll decay	Active roll damping 2
1049	Roll decay	Active roll damping 2

Continued on next page

Table E.4 – *Continued from previous page*

Run number	Name	Comment
1050	Roll decay	Active roll damping 2
1051	Roll decay	Active roll damping 2
1052	Roll decay	Active roll damping 2
1053	Roll decay	Active roll damping 2
8010	WAVE 8010: Regular H=1.5 T = 8	Wave calibration
8060	WAVE 8060: Regular H=1.5 T = 10	Wave calibration
8030	WAVE 8030: Regular H=1.5 T = 11	Wave calibration
8071	WAVE 8071: Regular H=1.5 T = 11.9	Wave calibration
8050	WAVE 8071: Regular H=1.5 T = 14	Wave calibration
2044	WAVE 8010: Regular H=1.5 T=8	No active damping
2060	WAVE 8010: Regular H=1.5 T=8	Active roll damping 2
2001	WAVE 8060: Regular H=1.5 T=10	No active damping
2045	WAVE 8060: Regular H=1.5 T=10	No active damping
2018	WAVE 8060: Regular H=1.5 T=10	Constant shaft speed 100%
2047	WAVE 8060: Regular H=1.5 T=10	Constant shaft speed 100%
2017	WAVE 8060: Regular H=1.5 T=10	Constant shaft speed 150%
2057	WAVE 8060: Regular H=1.5 T=10	Active roll damping 2
2061	WAVE 8060: Regular H=1.5 T=10	Active roll damping 2
2062	WAVE 8060: Regular H=1.5 T=10	Active roll damping 2
2007	WAVE 8030: Regular H=1.5 T=11	No active damping
2008	WAVE 8030: Regular H=1.5 T=11	No active damping
2012	WAVE 8030: Regular H=1.5 T=11	No active damping
2014	WAVE 8030: Regular H=1.5 T=11	No active damping
2016	WAVE 8030: Regular H=1.5 T=11	No active damping
2048	WAVE 8030: Regular H=1.5 T=11	No active damping
2006	WAVE 8030: Regular H=1.5 T=11	Constant shaft speed 100%
2050	WAVE 8030: Regular H=1.5 T=11	Constant shaft speed 100%

Continued on next page

Table E.4 – *Continued from previous page*

Run number	**Name**	**Comment**
2006	WAVE 8030: Regular H=1.5 T=11	Constant shaft speed 150%
2050	WAVE 8030: Regular H=1.5 T=11	Constant shaft speed 150%
2056	WAVE 8030: Regular H=1.5 T=11	Active roll damping 2
2063	WAVE 8030: Regular H=1.5 T=11	Active roll damping 2
2064	WAVE 8030: Regular H=1.5 T=11	Active roll damping 2
2065	WAVE 8030: Regular H=1.5 T=11	Active roll damping 2
2066	WAVE 8030: Regular H=1.5 T=11	Active roll damping 2
2009	WAVE 8071: Regular H=1.5 T=11.9	No active damping
2010	WAVE 8071: Regular H=1.5 T=11.9	No active damping
2011	WAVE 8071: Regular H=1.5 T=11.9	No active damping
2052	WAVE 8071: Regular H=1.5 T=11.9	No active damping
2019	WAVE 8071: Regular H=1.5 T=11.9	Constant shaft speed 100%
2053	WAVE 8071: Regular H=1.5 T=11.9	Constant shaft speed 100%
2021	WAVE 8071: Regular H=1.5 T=11.9	Constant shaft speed 150%
2058	WAVE 8071: Regular H=1.5 T=11.9	Active roll damping 2
2067	WAVE 8071: Regular H=1.5 T=11.9	Active roll damping 2
2068	WAVE 8071: Regular H=1.5 T=11.9	Active roll damping 2
2069	WAVE 8071: Regular H=1.5 T=11.9	Active roll damping 2
2004	WAVE 8071: Regular H=1.5 T=11.9	No active damping
2054	WAVE 8071: Regular H=1.5 T=11.9	No active damping
2059	WAVE 8071: Regular H=1.5 T=11.9	Active roll damping 2
2004	WAVE 8050: Regular H=1.5 T=14	No active damping
2054	WAVE 8050: Regular H=1.5 T=14	No active damping
3035	WAVE 8050: Regular H=1.5 T=14	Active roll damping 2
8100	WAVE 8100: IRR J H1.50 T9.60 G3.30 C0 RN155	Wave calibration
8120	WAVE 8120: IRR J H1.50 T11.88 G3.30 C0 RN74	Wave calibration
8111	WAVE 8111: IRR J H1.50 T14.01 G3.30 C0 RN161	Wave calibration

Continued on next page

Table E.4 – *Continued from previous page*

Run number	Name	Comment
3000	IRR J H1.50 T9.60 G3.30 C0 RN155	No active damping
3007	IRR J H1.50 T9.60 G3.30 C0 RN155	No active damping
3027	IRR J H1.50 T9.60 G3.30 C0 RN155	No active damping
3017	IRR J H1.50 T9.60 G3.30 C0 RN155	Constant shaft speed
3028	IRR J H1.50 T9.60 G3.30 C0 RN155	Constant shaft speed
3033	IRR J H1.50 T9.60 G3.30 C0 RN155	Active roll damping 2
3036	IRR J H1.50 T9.60 G3.30 C0 RN155	Active roll damping 2
3010	IRR J H1.50 T11.88 G3.30 C0 RN74	No active damping
3011	IRR J H1.50 T11.88 G3.30 C0 RN74	No active damping
3023	IRR J H1.50 T11.88 G3.30 C0 RN74	No active damping
3046	IRR J H1.50 T11.88 G3.30 C0 RN74	No active damping
3047	IRR J H1.50 T11.88 G3.30 C0 RN74	No active damping
3049	IRR J H1.50 T11.88 G3.30 C0 RN74	No active damping
3051	IRR J H1.50 T11.88 G3.30 C0 RN74	No active damping
3052	IRR J H1.50 T11.88 G3.30 C0 RN74	No active damping
3053	IRR J H1.50 T11.88 G3.30 C0 RN74	No active damping
3012	IRR J H1.50 T11.88 G3.30 C0 RN74	Constant shaft speed
3024	IRR J H1.50 T11.88 G3.30 C0 RN74	Constant shaft speed
3034	IRR J H1.50 T11.88 G3.30 C0 RN74	Active roll damping 2
3037	IRR J H1.50 T11.88 G3.30 C0 RN74	Active roll damping 2
3040	IRR J H1.50 T11.88 G3.30 C0 RN74	Active roll damping 2
3041	IRR J H1.50 T11.88 G3.30 C0 RN74	Active roll damping 2
3048	IRR J H1.50 T11.88 G3.30 C0 RN74	Active roll damping 2
3050	IRR J H1.50 T11.88 G3.30 C0 RN74	Active roll damping 2
3054	IRR J H1.50 T11.88 G3.30 C0 RN74	Active roll damping 2
3029	IRR J H1.50 T14.01 G3.30 C0 RN161	No active damping
3035	IRR J H1.50 T14.01 G3.30 C0 RN161	Active roll damping 2

Continued on next page

Table E.4 – *Continued from previous page*

Run number	**Name**	**Comment**
3042	IRR J H1.50 T14.01 G3.30 C0 RN161	New GM, no active roll damping
3043	IRR J H1.50 T14.01 G3.30 C0 RN161	New GM, active roll damping 2
3044	IRR J H1.50 T14.01 G3.30 C0 RN161	New GM, active roll damping